© 2021. Published by The Company of Biologists Ltd | Journal of Cell Science (2021) 134, jcs255752. doi:10.1242/jcs.255752

RESEARCH ARTICLE

Upregulation of APP endocytosis by neuronal aging drives amyloid-dependent synapse loss

Tatiana Burrinha[1], Isak Martinsson[2], Ricardo Gomes[1,3], Ana Paula Terrasso[1,3,4], Gunnar K. Gouras[2] and Cláudia Guimas Almeida[1,*]

ABSTRACT

Neuronal aging increases the risk of late-onset Alzheimer's disease. During normal aging, synapses decline, and β-amyloid (Aβ) accumulates intraneuronally. However, little is known about the underlying cell biological mechanisms. We studied neuronal aging using normal-aged brain and aged mouse primary neurons that accumulate lysosomal lipofuscin and show synapse loss. We identified the upregulation of amyloid precursor protein (APP) endocytosis as a neuronal aging mechanism that potentiates APP processing and Aβ production *in vitro* and *in vivo*. The increased APP endocytosis may contribute to the early endosome enlargement observed in the aged brain. Mechanistically, we showed that clathrin-dependent APP endocytosis requires F-actin and that clathrin and endocytic F-actin increase with neuronal aging. Finally, Aβ production inhibition reverts synaptic decline in aged neurons, whereas Aβ accumulation, promoted by endocytosis upregulation in younger neurons, recapitulates aging-related synapse decline. Overall, we identify APP endocytosis upregulation as a potential mechanism of neuronal aging and, thus, a novel target to prevent late-onset Alzheimer's disease.

This article has an associated First Person interview with the first author of the paper.

KEY WORDS: APP endocytosis, Clathrin-mediated endocytosis, Actin-dependent endocytosis, Neuronal aging, β-amyloid; Alzheimer's disease

INTRODUCTION

Late-onset Alzheimer's disease (AD), the most prevalent neurodegenerative disorder in the aging population, is increasing due to higher life expectancy, and an adequate treatment remains elusive. Aging is the biggest risk factor for late-onset AD. Identifying the causal mechanisms of late-onset AD is necessary for devising novel therapies to prevent or delay AD.

Cognitive decline develops with aging and often precedes AD (Yankner et al., 2008). The multifactorial mechanisms underlying this aging-associated cognitive decline are likely silent pathological mechanisms that will eventually trigger the onset of AD (Gauthier et al., 2006; Veitch et al., 2018). One of these mechanisms is the cellular aging of neurons, the AD primary cellular target (Mattson and Magnus, 2006). Unlike other brain cells, most neurons are embryonically born, do not undergo cell division and thus have a chronological age the same as that of the organism. Neurons are the major β-amyloid (Aβ) producers, the synaptotoxic agent that accumulates in amyloid plaques and triggers neurofibrillary tau tangle formation, the AD pathological hallmarks (Cole and Vassar, 2007; Palop and Mucke, 2010; Selkoe and Hardy, 2016). Thus, neurons contribute to the initiation of the disease. Synaptic loss, rather than neuronal death, likely triggers the initial cognitive decline (Morrison and Baxter, 2012). The aging-dependent synaptic decline has been characterized morphologically by synapse loss and disrupted remodeling of spines, the postsynaptic compartments, and physiologically by impaired synaptic plasticity, such as defects in synapse potentiation and weakening in the hippocampus and prefrontal cortex, likely undermining new memory establishment (Dickstein et al., 2013; Morrison and Baxter, 2012; Samson and Barnes, 2013; Yankner et al., 2008). How the aging of neurons drives synapse loss associated with aging is unclear.

Neurons without the cell division-diluting effect accumulate damage, such as lipofuscin, an autofluorescent undegradable long-lived complex consisting of oxidatively damaged proteins and lipids, a cellular aging hallmark (Mattson and Magnus, 2006). The lipofuscin accumulates in lysosomes, the endosomal trafficking pathway endpoint (Brunk and Terman, 2002; Mattson and Magnus, 2006).

In familial AD (fAD), the Aβ progressive accumulation initiates the cascade that leads to AD (Gordon et al., 2018; McDade et al., 2018; Selkoe and Hardy, 2016). Aβ accumulation results from the imbalance between production and clearance. Aβ accumulation in fAD is primarily due to increased Aβ42 production by neurons, caused by mutations that potentiate amyloid precursor protein (APP) cleavage by β-secretase (BACE1) or alter the cleavage by γ-secretase to produce Aβ42. However, in the absence of mutations, Aβ42 is normally produced (Haass et al., 1992), and it can accumulate in the brain with aging in mice, monkeys and humans (Baker-Nigh et al., 2015; Blair et al., 2014; Kikuchi et al., 2011; Lesné et al., 2013; Marks et al., 2017; Petersen et al., 2016). The progressive intracellular Aβ accumulation associated with synapse dysfunction precedes extracellular amyloid plaque formation (Baker-Nigh et al., 2015; Blair et al., 2014; Eimer and Vassar, 2013; Gouras et al., 2005; LaFerla et al., 2007; Pensalfini et al., 2014; Takahashi et al., 2002, 2004; Welikovitch et al., 2018).

The Aβ clearance likely diminishes with aging. Neprilysin, the most critical neuronal Aβ-degrading enzyme, loses activity with aging (Iwata et al., 2002), and APOEe4, an Aβ-binding lipoprotein isoform associated with aging and AD prevents Aβ transport out of the brain through the blood-brain barrier (Castellano et al., 2011; Shibata et al., 2000). In contrast, the contribution of increased production to Aβ accumulation with aging is less clear. Evidence

[1]iNOVA4Health, Chronic Diseases Research Center (CEDOC), NOVA Medical School (NMS), Universidade Nova de Lisboa, 1169-056 Lisboa, Portugal. [2]Experimental Dementia Research Unit, Lund University, 22184 Lund, Sweden. [3]iBET - Instituto de Biologia Experimental e Tecnológica, Apartado 12, 2780-901 Oeiras, Portugal. [4]Instituto de Tecnologia Química e Biológica, Universidade Nova de Lisboa, Av. da República, 2780-157 Oeiras, Portugal.

*Author for correspondence (claudia.almeida@nms.unl.pt)

T.B., 0000-0003-0166-6552; A.P.T., 0000-0002-4369-6277; G.K.G., 0000-0002-5500-6325; C.G.A., 0000-0001-9384-2896

Handling Editor: Giampietro Schiavo
Received 13 October 2020; Accepted 3 April 2021

Journal of Cell Science (2021) 134, jcs255752. doi:10.1242/jcs.255752

points to aging-dependent BACE1 and γ-secretase activities alteration (Fukumoto et al., 2004; Guix et al., 2012; Vassar et al., 2009; Placanica et al., 2009), but not in APP expression (Flood et al., 1997; Gegelashvili et al., 1994). From AD genetic risk factors studies, we and others have shown that alterations in the APP traffic into endosomes enhances APP processing and Aβ generation (Andersen et al., 2006; Herskowitz et al., 2012; Rajendran and Annaert, 2012; Ubelmann et al., 2017a; Xiao et al., 2012). It is unknown whether, during aging, alterations in the APP endocytic trafficking increase Aβ production. Whether aging-dependent Aβ accumulation, independent of Alzheimer's mutations, impacts the maintenance of synapses is unknown. In this study, we have investigated whether changes in APP endosomal trafficking with neuronal aging contribute to increased Aβ production and whether the increased Aβ generation is responsible for the age-dependent synaptic decline.

We chose primary mouse postmitotic cortical neurons aged in culture as a neuronal aging model as these cultures undergo an accelerated stereotyped differentiation process and recapitulate, in 4 weeks, important *in vivo* brain-aging aspects, such as lipofuscin accumulation, increased reactive oxygen species, protein oxidation and lipid alterations (Aksenova et al., 1999; Goslin and Banker, 1989; Martin et al., 2011; Papa et al., 1995; Trovò et al., 2013; Youmans et al., 2012). We found that aged primary neurons accumulate intracellular Aβ42, which correlates with the increase in APP processing observed *in vivo*. Such a phenomenon could be due to our discovery that APP endocytosis is upregulated in aged neurons, especially in neurites. We validated endocytosis upregulation in the aged brain. Mechanistically, we discovered that APP endocytic machinery is altered quantitatively but not qualitatively with aging *in vitro* and *in vivo*. Finally, we established causality between aging-dependent endocytic Aβ production and synapse decline. Overall, we identified a mechanism whereby neuronal aging may be contributing to the development of AD.

RESULTS

Intracellular Aβ42 increases with neuronal aging

Primary embryonic cortical neurons in culture undergo a stereotyped differentiation process. Briefly, during the first 7 days *in vitro* (7 DIV), axons and dendrites are formed; in the second week (14 DIV), dendrites develop, completing maturation after 3 weeks (21 DIV) (Boyer et al., 1998; Goslin and Banker, 1989). In accordance, we observed the highest microtubule-associated protein (MAP2) expression, a neuronal differentiation marker, at 21 DIV (Fig. 1A,B). Several groups have reported that neurons start aging or cellular senescence after 28 DIV (Aksenova et al., 1999; Goslin and Banker, 1989; Martin et al., 2011; Papa et al., 1995; Trovò et al., 2013; Youmans et al., 2012). We observed that primary neurons cultured for 21 and 28 DIV had similar MAP2 levels (Fig. 1A,B), and did not present gross morphological changes, such as axonal bead-like degeneration or dendritic shrinkage (Fig. 1C). Moreover, we observed a drastic reduction in doublecortin expression, a neuronal precursor marker, from 14 to 28 DIV, as described previously (Fig. S1A,B) (Francis et al., 1999). Notably, 28 DIV neurons showed cellular aging canonical signs, such as the accumulation of senescence-associated β-galactosidase^{+} cells (SA-β-Gal) (Fig. 1D,E) and the formation of the autofluorescent granules (Fig. S1C,D) (Bigagli et al., 2016; Dong et al., 2014; Gray and Woulfe, 2005; Jurk et al., 2012). The autofluorescent granules were considered lipofuscin when localized within the lysosome-associated membrane protein 1 (LAMP1)$^{+}$ late endosomes/lysosomes (Fig. 1F). The amount of lysosomal lipofuscin was significantly higher (6-fold) in cell bodies of aged neurons (28 DIV), in which most neuronal lysosomes localize (Ferguson, 2018) compared with mature neurons (21 DIV), consistent with the aging-dependent accumulation of lysosomal lipofuscin (Fig. 1G). We found a non-significant tendency for glial fibrillary acidic protein (GFAP), a glial cell marker, to increase with time in culture, indicating glial cells limited proliferation in our experimental conditions (Fig. S1E,F). Overall, we established a cellular aging model of postmitotic neurons without neurodegeneration.

Previously, we demonstrated that intracellular Aβ42 progressively accumulates with time in primary transgenic neurons due to mutant hAPP (Swe) overexpression (Takahashi et al., 2004). To investigate whether endogenous Aβ42 accumulates intracellularly in aged wild-type neurons, we used a sensitive semi-quantitative immunofluorescence assay with an Aβ42 C-terminal specific antibody (12F4) (Ubelmann et al., 2017a) not recognizing APP (Fig. S2A) and not labeling APP knockout neurons (Fig. S2B). By analyzing the Aβ42 accumulation in neurites and cell bodies separately, we discovered a significant increase in Aβ42 accumulation (56%) in aged neurites compared to mature neurites (Fig. 1H,I). In the aging cell body, Aβ42 increased (16%) less than in aged neurites, being significantly different only when compared with immature neurites (14 DIV) (Fig. 1H,I). Moreover, we analyzed endogenous Aβ40, which increased (59%) in aged neurites (Fig. S2C,D). In contrast, Aβ42 or Aβ40 (and ratio) levels were unchanged in the aged neurons-conditioned medium using a specific anti-Aβ40 and Aβ42 enzyme-linked immunosorbent assay (ELISA) assay (Fig. S2E-G). The endogenous Aβ secretion may be reduced or more likely undetectable in our experimental conditions as aged neurons overexpressing C99 showed an increase in extracellular Aβ (Guix et al., 2012).

Aβ accumulation and APP processing occur mainly in endosomes in neurites, close to distal synapses (Das et al., 2016; Takahashi et al., 2004). We analyzed the impact of neuronal aging on APP distribution between the cell body and neurites using a specific anti-APP antibody (Y188) (Ubelmann et al., 2017a), which showed no labeling in APP knockout neurites (Fig. S2B). We applied our semi-quantitative immunofluorescence assay to measure APP enrichment in neurites versus cell bodies of aged and mature neurons. We found a significant increase in APP intensity in aged neurites (52%) compared to mature neurites (Fig. 1J,K). In contrast, the APP intensity did not change with neuronal aging in the cell body (Fig. 1J,K). The APP increase in neurites correlated with the increased Aβ42 level detected in neurites (Fig. 1H,I).

Next, we explored whether this increase was occurring in axons or dendrites. We analyzed APP in axons identified by Ankyrin G (AnkG^{+}) and in dendrites (AnkG^{-}) (Fig. S1G). APP was enriched in axons over dendrites in both mature and aged neurons, but the axon/dendrite ratio decreased slightly in aged neurons (Fig. S1H). Indeed, APP increased in aged dendrites (42%) more than in aged axons (28%) (Fig. S1I). The APP increase in neurites may be linked to changes in APP trafficking. These results indicate that neuronal aging drives intracellular Aβ42 accumulation by altering APP processing and trafficking, specifically in neurites.

APP processing and early endosome EEA1 increase with aging

To assess whether APP processing potentiates Aβ42 accumulation in aged neurons, we analyzed the APP C-terminal fragment (APP CTFs) levels by western blotting using an anti-APP CTF (APPY188) antibody in cultured neurons (14, 21 and 28 DIV) and in wild-type C57BL/6 mice (adult, 6 months; aged, 18 months) brain cortex (Fig. 2A,H).

Journal of Cell Science (2021) 134, jcs255752. doi:10.1242/jcs.255752

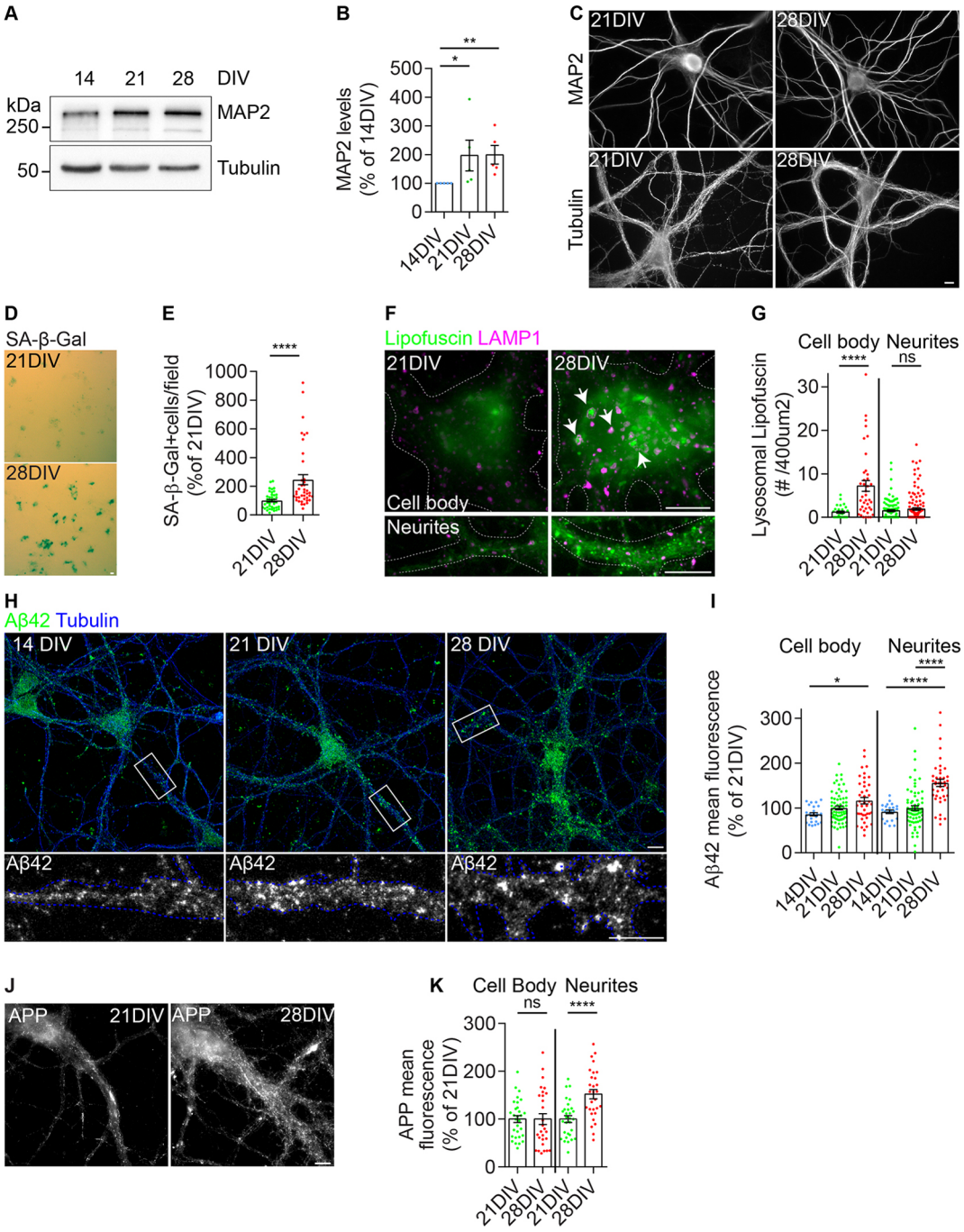

Fig. 1. Primary neurons aged in culture accumulate intracellular Aβ42. (A) Western blot showing MAP2 and tubulin expression in primary neurons (14, 21 and 28 DIV). (B) Quantification of normalized MAP2 levels (n=5). (C) Representative images of MAP2 and tubulin-immunolabeled neurons (21 and 28 DIV). (D) SA-β-galactosidase$^+$ (blue) neurons (21 and 28 DIV). (E) Quantification of the number of SA-β-galactosidase$^+$ (blue) cells per field (N=4). (F) Lipofuscin (arrowheads; green) and LAMP1 (magenta) localization in the cell body and neurites of neurons (21 and 28 DIV). (G) Quantification of lysosomal lipofuscin, defined by the number of colocalizations of autofluorescent granules with LAMP1$^+$ lysosomes per area (400 µm^2) (n=4, $N_{cellbody}$=28-39, $N_{neurites}$=104-129). (H) Intracellular endogenous Aβ42 (green) and tubulin (blue) in neurons (14, 21 and 28 DIV). The white rectangles indicate magnified neurites outlined based on tubulin (blue). (I) Quantification of mean Aβ42 intensity in cell body and neurites (n=3-6, $N_{cellbody}$=25-70, $N_{neurites}$=22-73). (J) APP in the cell body and neurites of neurons (21 and 28 DIV). (K) Quantification of APP mean intensity in the cell body and neurites of neurons (21 and 28 DIV) (n=3, $N_{cellbody}$=28-30; $N_{neurites}$=29-30). Data are mean±s.e.m. Statistical significance was determined by Mann–Whitney test (E,G,K) or one-way ANOVA on ranks with post-hoc Dunn's testing (B,I). *P<0.05; **P<0.01; ****P<0.0001; ns, not significant. Scale bars: 10 µm.

We could observe different bands corresponding to APP CTFs (Fig. 2A,H), with the lower molecular weight bands likely corresponding to both the non-amyloidogenic α-CTF (C83; 10 kDa), the product of α-secretase, and the amyloidogenic β-CTF (C89; 12 kDa), a product of β-secretase cleavage. The band above, more visible after adjusting contrast, likely corresponds to the longer amyloidogenic β-CTF (C99; 14 kDa). A higher molecular weight band (>25 kDa) likely corresponds to η-CTF (C191) (Fig. 2A,H) (Willem et al., 2015). We found that the APP CTFs/APP ratio increased in aged neurons (82%) and brain (118%)

Journal of Cell Science (2021) 134, jcs255752. doi:10.1242/jcs.255752

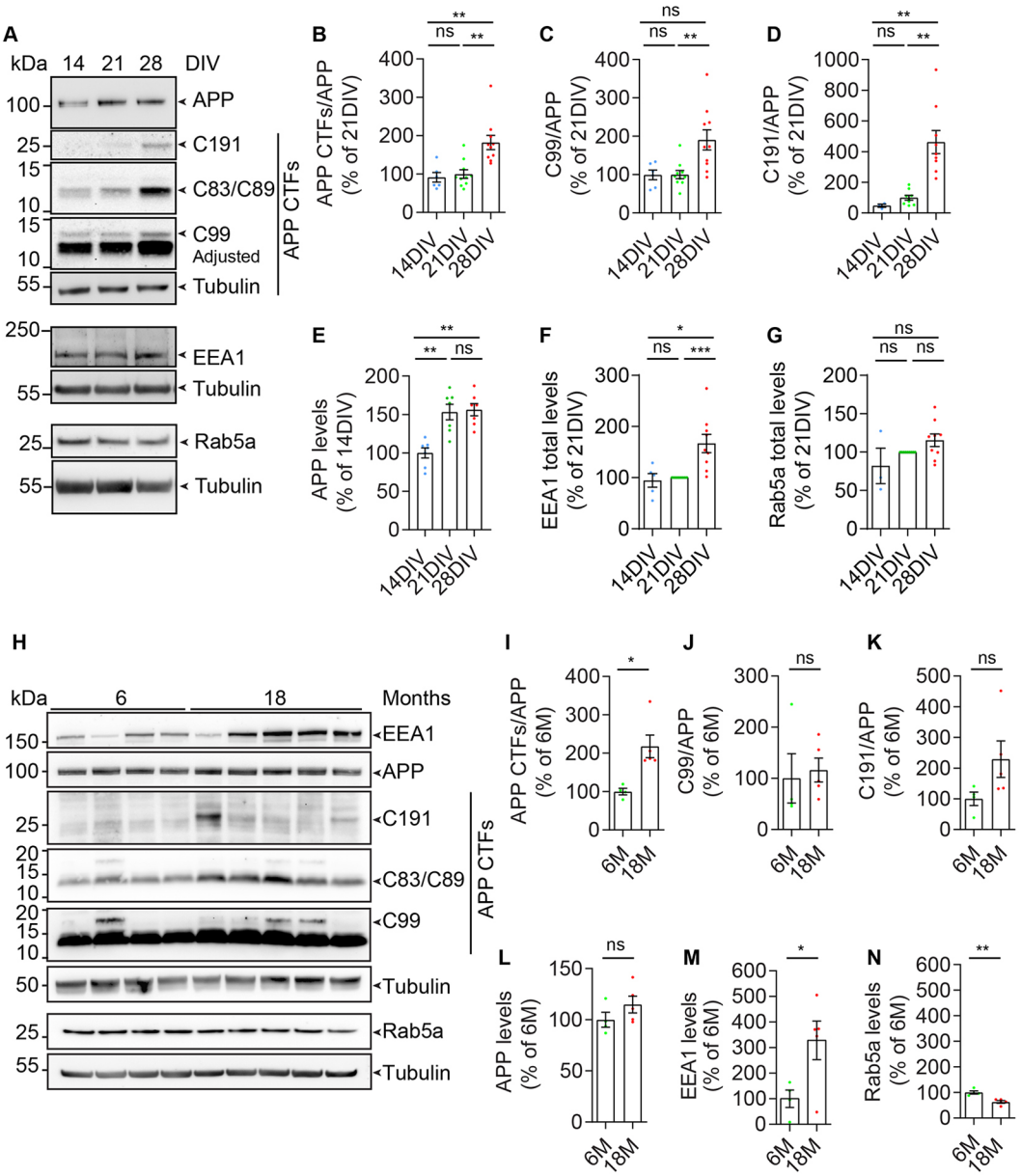

Fig. 2. Neuronal aging potentiates APP processing and early endosome EEA1 accumulation *in vitro* and *in vivo*. (A) Western blot showing endogenous APP, APP-CTFs (C191, C83/89 and C99), EEA1, Rab5a and tubulin levels in neurons (14, 21, and 28 DIV). (B) Quantification of APP-CTFs normalized to APP in neurons (n=6-10). (C) Quantification of C99 normalized to APP in neurons (n=6-10). (D) Quantification of C191 normalized to APP in neurons (n=6-9). (E) Quantification of APP normalized to tubulin in neurons (n=7). (F) Quantification of EEA1 normalized to tubulin in neurons (n=5-9). (G) Quantification of Rab5a normalized to tubulin in neurons (n=3-9). (H) Western blot showing endogenous EEA1, APP, APP-CTFs, Rab5a and tubulin in brain (6 and 18 months). (I) Quantification of APP-CTFs normalized to APP in brain (n=4-5; *P=0.0110). (J) Quantification of C99 normalized to APP in brain (n=4-5). (K) Quantification of C191 normalized to APP in brain (n=4-5). (L) Quantification of APP normalized to tubulin in brain (n=4-5). (M) Quantification of EEA1 normalized to tubulin in brain (n=4-5). (N) Quantification of Rab5a normalized to tubulin in brain (n=4-5). Data are mean±s.e.m. Statistical significance was determined by one-way ANOVA on ranks with post-hoc Dunn's testing (B-G) or unpaired two-tailed Wilcoxon t-test (I-N). *P<0.05; **P<0.01; ***P<0.001; ns, not significant.

(Fig. 2B,I). Interestingly, the higher molecular weight APP CTFs (C99 and C191) were more evident in aged neurons and the brain. However, despite being significantly different in aged neurons, it did not reach significance in the aged brain (Fig. 2C,D,J,K), suggesting increased β and η processing of APP with aging. This increase in APP CTFs supports higher APP processing with aging. Of note, we found that mature neurons (21 DIV) compared with immature neurons (14 DIV) showed increased APP levels but not an increased APP CTFs/APP ratio (Fig. 2B,E), likely due to increased APP expression with neuronal maturation and synaptogenesis (Hung et al., 1992; Nicolas and Hassan, 2014). We did not detect alterations in full-length APP levels with aging *in vitro* and *in vivo* (Fig. 2E,L), discarding a significant impact of neuronal aging on APP expression or degradation. Moreover, BACE1 and nicastrin levels, a γ-secretase subunit, were not significantly altered in aged neurons compared with mature neurons (Fig. S3A,B), recapitulating *in vivo* data (Fukumoto et al., 2004; Guix et al., 2012). The increase in APP processing without changes in full-length APP, nicastrin and BACE1 may indicate an alteration in their activity (Fukumoto et al., 2004; Guix et al., 2012) or an increased encounter due to altered trafficking with neuronal aging. APP processing can occur during its secretory and endocytic trafficking (Toh et al., 2017; Ubelmann

Journal of Cell Science (2021) 134, jcs255752. doi:10.1242/jcs.255752

et al., 2017a). We started by investigating endocytic trafficking alterations with aging by analyzing EEA1 and Rab5a levels, early endosome (EE) markers, by western blotting. We found EEA1 but not Rab5a increased in aged neurons (67%) (Fig. 2A,F,G) and aged brain (228%) (Fig. 2H,M,N). The difference in EEA1 and Rab5a may be due to EEA1 being an EE-associated protein with little expression in the cytosol, whereas Rab5 cycles between a GTP form (EE bound) and GDP form (cytosolic), and its total levels may not reflect a change in EE or endocytosis (Ullrich et al., 1994). These data suggest a new correlation between increased APP processing and upregulated endocytosis in aged neurons and aged brain.

APP endosomal localization and early endosomes increase with aging

As we found that EEA1 expression increased with aging (Fig. 2), we investigated whether EEs increased and whether APP would be more present in EEs in aged neurons and aged brain. *In vitro*, we quantified EE density, size and intensity by analyzing $EEA1^+$ and $Rab5a^+$ puncta in mature and aged neurites. $EEA1^+$ and $Rab5a^+$ EE densities were unaltered, but their size and intensity increased in aged neurites (Fig. 3A-H). Because the anti-EEA1 antibody labels EEs better than the anti-Rab5a antibody, we analyzed APP colocalization only with EEA1 in neurites (Fig. 3I) of aged and

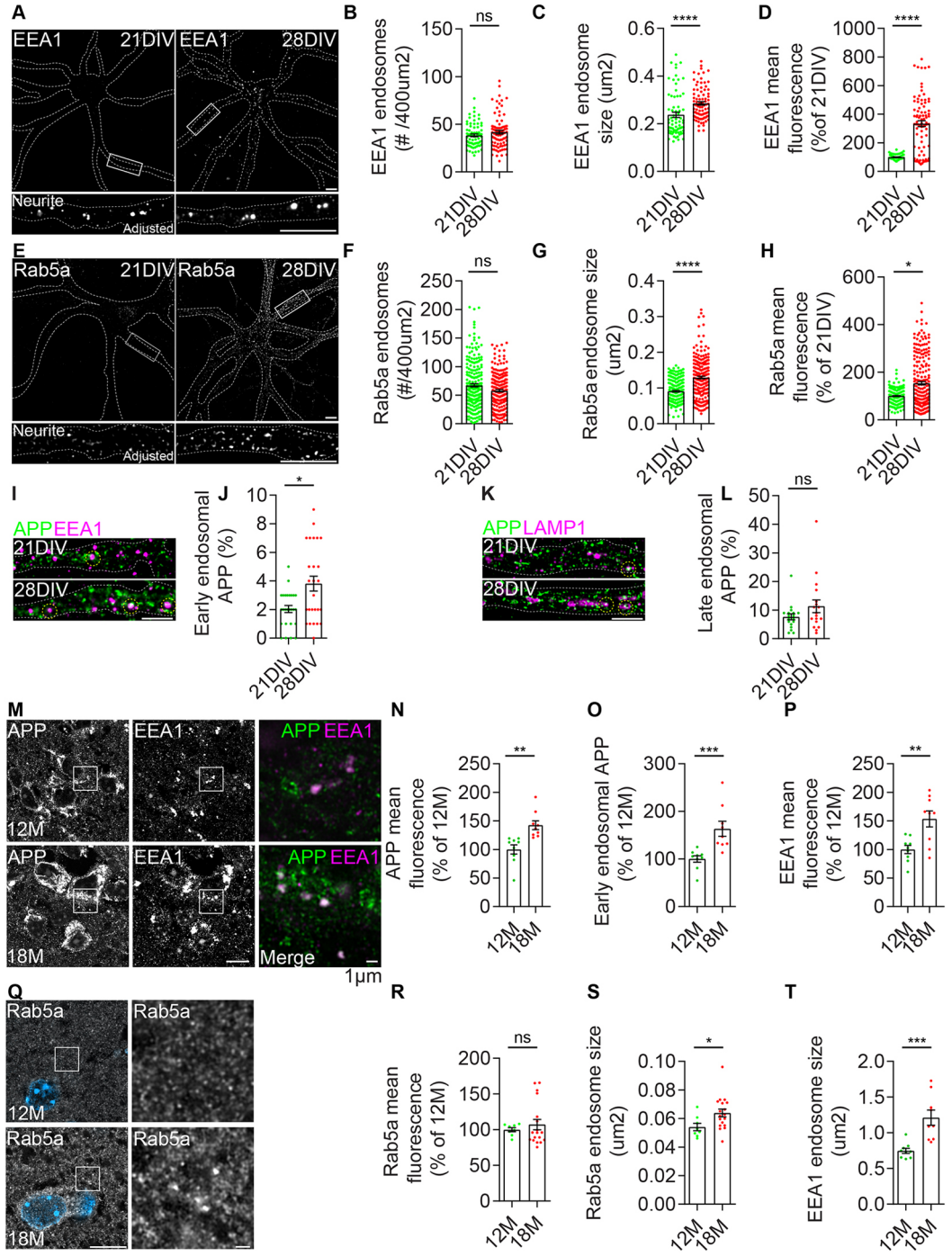

Fig. 3. See next page for legend.

Journal of Cell Science

Fig. 3. Neuronal aging increases APP localization to enlarged early endosomes *in vitro* and *in vivo*. (A) EEA1$^+$ EEs in primary neurons (21 and 28 DIV), displayed after background subtraction, with neurons outlined in white and white rectangles indicating magnified neurites. EEA1 levels were adjusted at 21 DIV. (B) Quantification of EEA1$^+$ EE number per area (400 µm^2) in neurites (*n*=3, *N*=72-85). (C) Quantification of EEA1$^+$ EE mean size (µm^2) in neurites (*n*=3, *N*=72-85). (D) Quantification of EEA1$^+$ EE mean intensity in neurites (*n*=3, *N*=72-85). (E) Rab5a$^+$ EEs in neurons (21 and 28 DIV), displayed after deconvolution, with neurons outlined in white and white rectangles indicate magnified neurites. Rab5a levels were adjusted at 21DIV. (F) Quantification of the Rab5a$^+$ EE number per area (400 µm^2) in neurites (21 and 28 DIV) (*n*=5, *N*=221-223). (G) Quantification of the mean size of each Rab5a$^+$ EEs (µm^2) in neurites (21 and 28 DIV) (*n*=5, *N*=221-223). (H) Quantification of Rab5a$^+$ EE mean intensity in neurites (21 and 28 DIV) (*n*=5, *N*=221-223). (I) APP (green) localization in EEA1$^+$ EEs (magenta) in neurites (21 and 28 DIV) displayed after background subtraction. (J) Quantification of the number of APP$^+$ EEs per area (400 µm^2) in neurites (21 and 28 DIV) (*n*=3; *N*=131-144). (K) APP (green) localization in LAMP1$^+$ late endosomes (magenta) in neurites (21 and 28 DIV). Images are displayed after background subtraction. (L) Quantification of APP$^+$ late endosome number per area (400 µm^2) in neurites (21 and 28 DIV) (*n*=3; *N*=18). (M) APP (green) localization in EEA1$^+$ endosomes (magenta) in brain (12 and 18 months). The white rectangles indicate magnified regions. (N) Quantification of APP puncta mean intensity in brain (12 and 18 months) (*n*=3, N_{images}=9). (O) Quantification of early endosomal APP intensity in brain (12 and 18 months) (*n*=3, N_{images}=9). (P) Quantification of EEA1 mean intensity in brain (12 and 18 months) (*n*=3, N_{images}=9). (Q) Rab5a$^+$ endosomes in brain (12 months and 18 months). The white rectangles indicate magnified regions. (R) Quantification of Rab5a mean intensity in brain (12 and 18 months) (*n*=3, N_{images}=8-18). (S) Quantification of Rab5a size in brain (12 and 18 months) (*n*=3, N_{images}=8-18). (T) Quantification of EEA1 size in brain (12 and 18 months) (*n*=3, N_{images}=9). Data are mean±s.e.m. **P*<0.05; ***P*<0.01; ****P*<0.001; *****P*<0.0001; ns, not significant (Mann–Whitney test). Scale bars: 10 µm (A,E,I,K,M,Q); 1 µm (insets in M,Q).

mature neurons by automatically measuring the percentage of EEA1$^+$ endosomes containing APP. We found 87% more APP in EEs in aged neurites (Fig. 3J). We analyzed APP colocalization with LAMP1, a late endosome/lysosome marker (Fig. 3K). We did not find a significant increase in late endosomal APP in aged neurites (Fig. 3L). Together, these results indicate that APP may redistribute to EEs with neuronal aging. We confirmed this *in vivo* as we found 63% more APP in EE in the aged brain (Fig. 3M,O). We noticed that, like in aged neurons, APP (42%) and EEA1 (53%) intensity increased in the aged brain but not Rab5a intensity, potentially due to cytosolic Rab5a and/or the lower affinity of anti-Rab5a (Fig. 3N,P,Q,R). Interestingly, Rab5a$^+$ endosome size increased (18%), and more pronounced was the 62% enlargement in EEA1$^+$ endosome size in the aged brain (Fig. 3S,T). Overall, these data indicate that APP localizes more to enlarged EEs with aging.

APP endocytosis increases with aging

To further explore the age-dependent APP increase in EEs, we directly assessed APP endocytosis in aged neurons. To study APP endocytosis, we used two endocytosis assays. We performed a biotinylated APP endocytosis assay (Fig. 4A) in which we biotinylated live neurons with cleavable NHS-SS biotin. Biotinylated APP was detected using a specific anti-APP antibody (Y188) (Ubelmann et al., 2017a). The surface biotin cleavage with non-permeable reducing agent glutathione (GSH) allowed for the detection of endocytosed biotinylated APP (Snyder et al., 2005). After 10 min chase, most biotinylated APP remained at the cell surface (10 min minus GSH), and only a small surface APP fraction was endocytosed (10 min plus GSH). After 30 min chase, the endocytosed APP level (30 min plus GSH) increased, being more endocytosed by aged neurons than by mature neurons (Fig. 4B). Quantification revealed that biotin-APP endocytosis at 10 min was 7-fold higher in aged neurons than in mature neurons. After 30 min, APP endocytosis in aged neurons was higher (10-fold) (Fig. 4C). We noticed a 49% increase in biotin-APP after 10 min (without GSH), suggestive of an increase in surface APP (Fig. 4D) as APP total levels were unaltered in aged neurons (Fig. 4E).

We performed an anti-APP antibody internalization assay by pulsing live neurons with a mouse monoclonal antibody against the APP extracellular N-terminal domain (22C11) (Acevedo et al., 2011; Chaufty et al., 2012; Jung et al., 1996; Sullivan et al., 2014; Sun et al., 2019; Ubelmann et al., 2017a,b). We controlled for 22C11 specificity using APP knockout neurons and found a significant reduction in 22C11 intensity in the absence of APP in neurites (Fig. S3C,D). After 10 min, we detected the APP$^+$ endosomes with a fluorescently labeled secondary anti-mouse IgG antibody to detect the endocytosed 22C11 bound to APP (Ubelmann et al., 2017b) (Fig. 4G). Of note, the prompt detection of 22C11 endocytosis in mature and aged neurons was unexpected as, in previous work using immature neurons (9 DIV), APP overexpression was required to consistently detect APP endocytosis (Ubelmann et al., 2017a). The endogenous APP endocytosis detection indicates an increase in the APP undergoing endocytosis with neuronal maturation and aging. In agreement, we observed that, in mature neurons, APP$^+$ endosomes were easily detected in the cell body, and in aged neurons, APP$^+$ endosomes were also detected in neurites (Fig. 4F). Endocytosed APP was 71% more enriched in Rab5a$^+$ EEs in aged neurons than in mature neurons (Fig. S3E,F). We analyzed the endocytosed APP colocalization with Rab5a and detected Rab5a in 26% of APP$^+$ endosomes (Fig. S3E,G). We checked whether Rab11a, a Rab GTPase enriched in recycling endosomes, colocalized with APP$^+$ endosomes. Only 12% of APP$^+$ endosomes were positive for Rab11a, which was not due to reduced Rab11a expression (Fig. S3E,G,H,I). Together, these data show that after 10 min internalized APP is mostly in EEs. To quantify, we segmented each APP$^+$ endosome and analyzed its density, intensity and size in neurites. APP$^+$ endosome density (34%) and intensity (10%), but not size, increased in aged neurites compared to mature neurites (Fig. 4F,H-J). We found that the increase in APP endocytosis did not translate into higher APP degradation as neither the biotin-APP degradation in aged neurons was significantly different from those in mature neurons (Fig. 4K-M) nor APP total levels in aged neurons and aged brain (Fig. 4E; Fig. 2E,L). With regards to surface APP, we observed that it was organized in patches in neurites (Storey et al., 1996; Yamazaki et al., 1995), and its mean intensity increased with age by 68%, which is supported by the APP increase in neurites and suggestive of alterations in trafficking and the secretory pathway (Fig. 4N,O). We observed that recycled APP spread through neurites, with its mean intensity increasing by 25% in aged neurites (Fig. S3J,K), suggesting that the increase in endocytosed APP is not explained by decreased APP recycling. Instead, the increase in recycling may contribute to the higher APP levels at the surface (Fig. 4N,O).

Together these results indicate that APP endocytosis increases with aging, mainly in neurites, explaining the substantial rise observed in Aβ42 neuritic accumulation (Fig. 1H,I). Additionally, we provide hints that other trafficking pathways may change with aging, such as the secretory pathway and endocytic recycling.

Upregulation of endocytosis with aging: a generalized mechanism?

Given the increase in APP endocytosis and EE, we next assessed whether there was a general increase in endocytosis. To assess bulk

Journal of Cell Science (2021) 134, jcs255752. doi:10.1242/jcs.255752

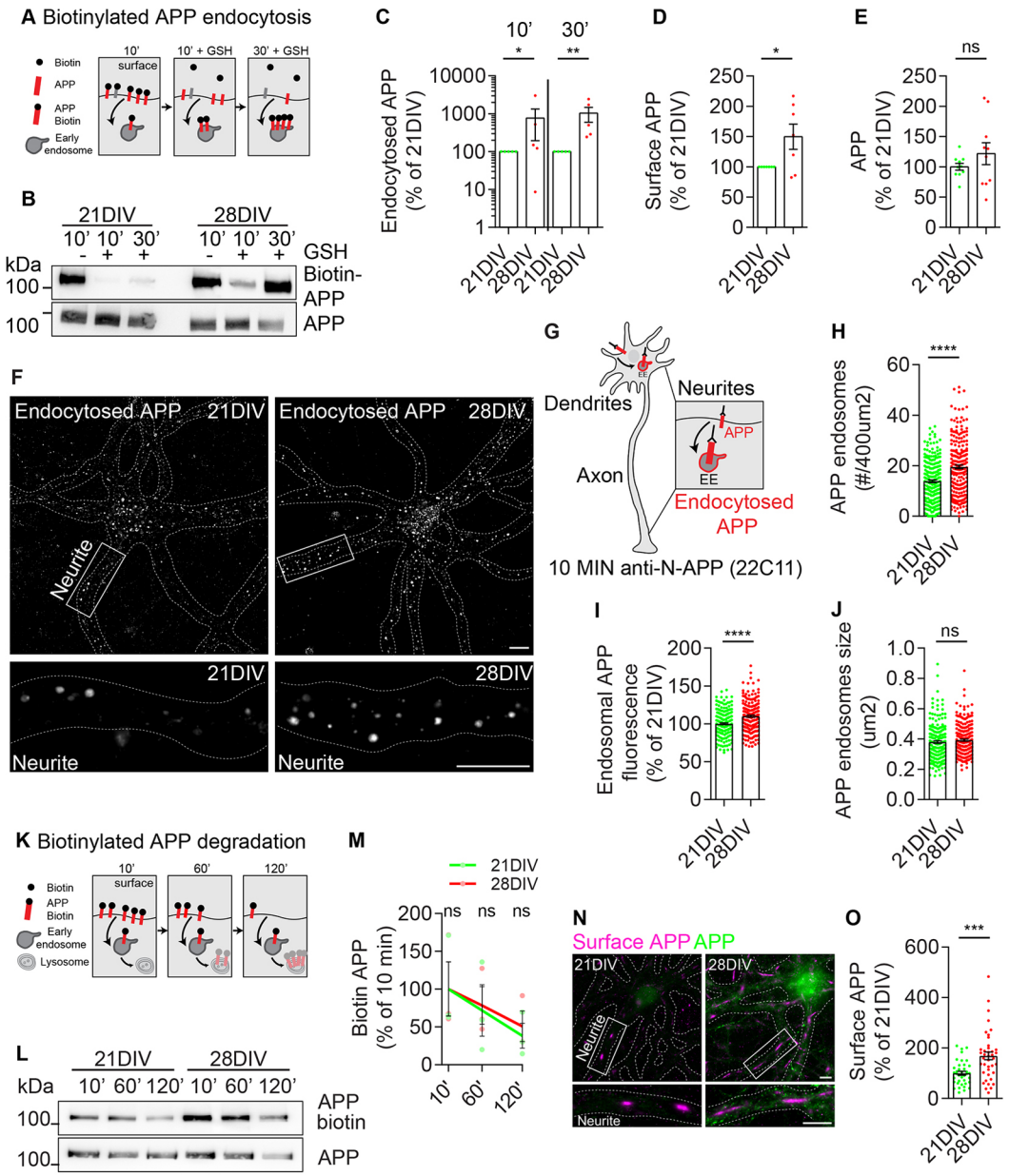

Fig. 4. APP endocytosis upregulation in aged neurons. (A) Schematic illustrating the APP endocytosis assay using surface protein biotinylation. Biotinylated proteins after 10 min chase (10′); endocytosed biotinylated proteins after 10 min chase and removal of surface biotin with non-cell permeable GSH (10′+GSH); endocytosed biotinylated proteins after 30 min chase and removal of surface biotin with non-cell permeable glutathione (GSH) (30′+GSH). (B) Western blot showing surface and endocytosed biotinylated APP (biotin-APP) detected with anti-APP (Y188) in neurons (21 and 28 DIV). (C) Quantification of endocytosed biotin-APP in neurons (logarithmic scale; *n*=5). (D) Quantification of surface biotin-APP normalized to tubulin in neurons (*n*=7). (E) Quantification of total APP normalized to tubulin in neurons (*n*=5). (F) Endocytosed APP (10 min) in neurons (21 and 28 DIV). The white rectangles indicate magnified neurites. (G) Schematic illustrating APP endocytosis after 10 min using a specific antibody against the APP N-terminus (22C11). (H) Quantification of APP$^+$ endosome number (10 min) per area (400 µm^2) in neurites (*n*=5, *N*=220-230). (I) Quantification of the mean intensity of APP$^+$ endosomes in neurites (*n*=5, *N*=221-223). (J) Quantification of APP$^+$ endosome mean size (µm^2) in neurites (*n*=5, *N*=221-223). (K) Schematic illustrating the degradation assay using APP biotinylation after a chase for 10 min (10′); 60 min (60′); and 120 min (120′). (L) Western blot showing biotin-APP and total APP in neurons (21 and 28 DIV). (M) Quantification of the rate of biotin-APP degradation in neurons (*n*=3). (N) Surface APP (magenta) and total APP (green) in neurons (21 and 28 DIV). The white rectangles indicate magnified neurites. (O) Quantification of surface APP mean intensity in neurites (*n*=2, *N*=38-40). Data are mean±s.e.m. Statistical significance was determined by a Kolmogorov–Smirnov test (C-E,M) or a Mann–Whitney test (G-J,O). *P<0.05; **P<0.001; ***P<0.001; ****P<0.0001; ns, not significant. Scale bars: 10 µm.

endocytosis, we used the styryl dye FM1-43 that incorporates the external leaflet of the plasma membrane and concentrates in endosomes upon bulk endocytosis (Fomina et al., 2003). Indeed, after a 10-min pulse with FM1-43 in live neurons, we observed the formation of bright FM1-43 endocytic puncta in aged and mature neurons (Fig. 5A-D). Quantification of FM1-43 puncta density, intensity and size revealed no difference in puncta density but a 32% increase in intensity and an 8% increase in size in aged neurites (Fig. 5B-D).

Next, as APP endocytosis is clathrin dependent (Cirrito et al., 2008; Cossec et al., 2010; Marquez-Sterling et al., 1997), we analyzed transferrin endocytosis, the canonical clathrin-mediated

Journal of Cell Science (2021) 134, jcs255752. doi:10.1242/jcs.255752

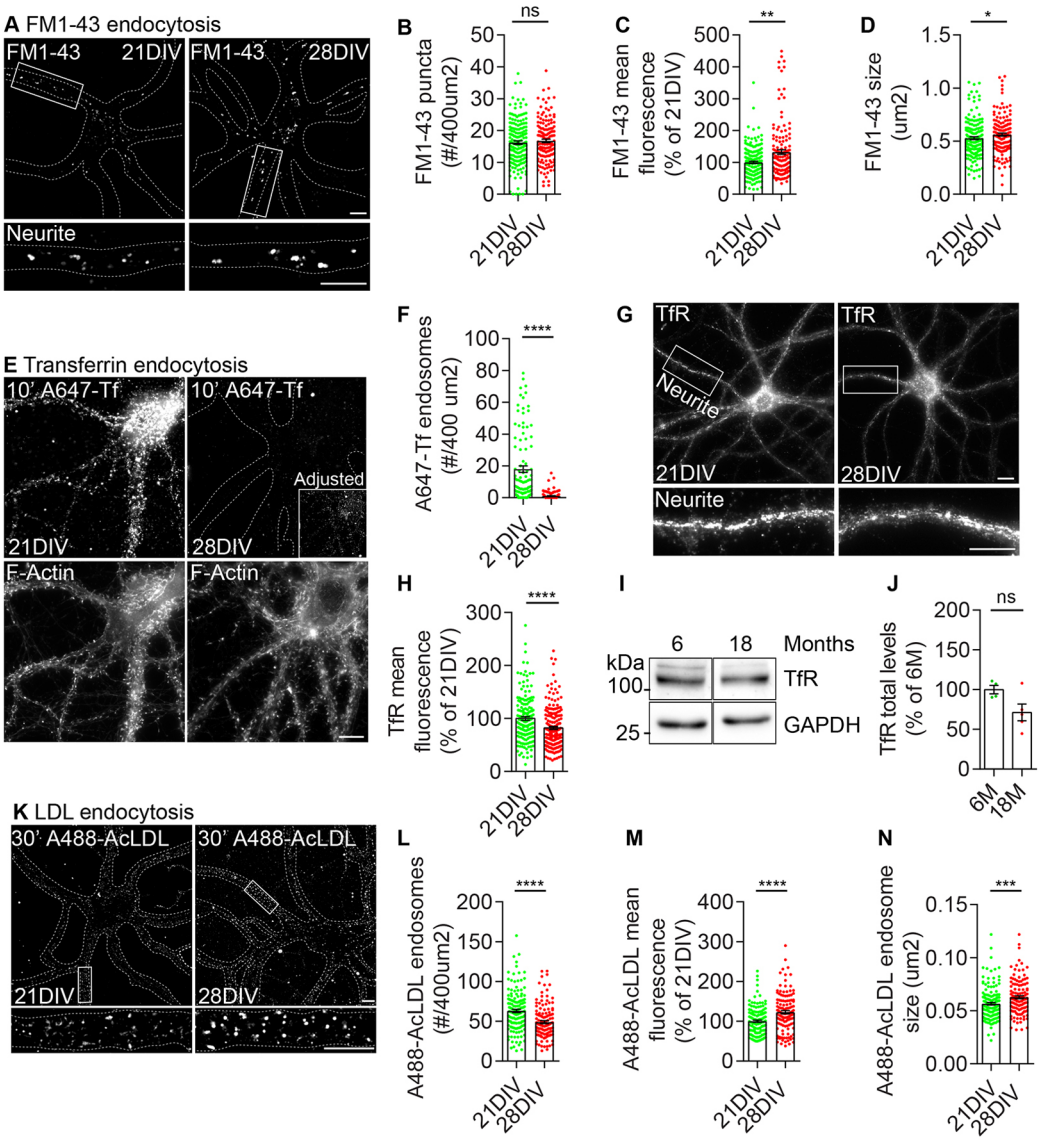

Fig. 5. Neuronal aging increases bulk and LDL endocytosis but not transferrin endocytosis or transferrin receptor. (A) FM1-43 bulk endocytosis for 10 min in neurons (21 and 28 DIV). White rectangles indicate magnified neurites. (B) Quantification of FM1-43 puncta number per area (400 µm^2) in neurites (n=4, N=148-178). (C) Quantification of the FM1-43 puncta mean intensity in neurites (n=4, N=147-178). (D) Quantification of FM1-43 puncta mean size (µm^2) in neurites (n=4, N=149-171). (E) Transferrin endocytosis (Alexa647-Tf; 10′) and F-actin (phalloidin) in neurons (21 and 28 DIV). (F) Quantification of the transferrin endosome number per area (400 µm^2) in neurites (n=3, N=105-156). (G) TfR in neurites (21 and 28 DIV). White rectangles indicate magnified neurites. (H) Quantification of the TfR mean intensity in neurites (n=2, N=165-183). (I) Western blot showing TfR and GAPDH expression in brain (6 and 18 months). (J) Quantification of TfR levels normalized to GAPDH in the brain (n=4-5). (K) Endocytosed LDL (30 min) in neurons (21 and 28 DIV). The white rectangles indicate magnified neurites. (L) Quantification of the number of LDL$^+$ endosomes, defined by the 30 min uptake of A488-AcLDL per area (400 µm^2) in neurites (n=3, N=127-153). (M) Quantification of LDL$^+$ endosome mean intensity in neurites (n=3, N=127-153). (N) Quantification of LDL$^+$ endosome mean size (µm^2) in neurites (n =3, N=127-153). Data are mean±s.e.m. *P<0.05; ** P<0.01; ***P<0.001; ****P<0.0001; ns, not significant (Mann–Whitney test). Scale bars: 10 µm.

endocytosis (CME) cargo. We pulsed live neurons for 10 min with fluorescently labeled transferrin (A647-Tf) that, upon binding to surface transferrin receptor (TfR), is internalized and delivered to EEs (Maxfield and McGraw, 2004). Unexpectedly, we observed a drastic reduction (88%) of transferrin endocytosis in aged neurons (Fig. 5E,F). To understand whether this was due to a reduction in TfR, we analyzed TfR levels in aged neurons (Fig. 5G,H) and aged brain (Fig. 5I,J). In aged neurites, the TfR was significantly reduced by 18% (Fig. 5H), although in the aged brain, the TfR total levels showed only a tendency to decrease (Fig. 5J). We decided to analyze a third CME cargo, acetyl-low-density lipoprotein (LDL) endocytosis (Davis et al., 1987; Ehrlich et al., 2004). We found the LDL endocytosis kinetics slower than APP as we could only detect the LDL$^+$ endosome formation after 30 min. Nevertheless, LDL endocytosis was readily detected in mature neurons and was more prominent in aged neurons (Fig. 5K). Indeed, quantification revealed that, although the LDL$^+$-endosome density decreased, their intensity and size increased by 23% and 14% in aged neurites (Fig. 5L-N).

Together these results indicate a potentially aging-specific decrease in transferrin endocytosis that could be linked to changes in iron metabolism with aging (Lu et al., 2017). In contrast, the increase in FM1-43, LDL and APP endocytosis in aged neurons supports general endocytosis upregulation with aging.

Journal of Cell Science (2021) 134, jcs255752. doi:10.1242/jcs.255752

Aging upregulation of APP endocytosis is dependent on clathrin and actin

We decided to investigate how aged neurons endocytose APP. In young neurons, APP undergoes CME (Cirrito et al., 2008; Marquez-Sterling et al., 1997). Clathrin assembles into lattices to facilitate plasma membrane invagination and endocytic vesicle formation, but endocytosis can occur independently of clathrin (Kaksonen and Roux, 2018; Mayor and Pagano, 2007). We treated mature neurons with clathrin assembly inhibitors Pitstop2 (30 µM) (Dutta et al., 2012) and chlorpromazine (CPZ; 0.14 µM) (Ivanov, 2008), and controlled their impact on transferrin endocytosis before the APP endocytosis assay. Control experiments showed that in neurons at 21 DIV, Pitstop2 and CPZ blocked transferrin endocytosis as expected (Fig. S4A,B). Similar experiments were not performed at 28 DIV because transferrin endocytosis was almost undetectable. Moreover, CPZ reduced APP endocytosis in neurons at 21 DIV, whereas Pitstop2 did not, indicating APP endocytosis in mature neurons is more sensitive to CPZ than to Pitstop2-dependent clathrin inhibition, potentially due to their different mechanisms of action (Daniel et al., 2015; Willox et al., 2014) (Fig. S4C). In aged neurons, both Pitstop2 and CPZ reduced APP endocytosis in aged neurites (Fig. 6A,B), supporting the endocytosis of aged neurons being more sensitive to clathrin inhibition than mature neurons.

Clathrin-mediated endocytosis depends on dynamin GTPase activity for clathrin-coated vesicle scission. Dynamin polymerizes around the vesicle neck, cutting it upon GTP hydrolysis (Roux et al., 2006; Shpetner and Vallee, 1992; Tuma and Collins, 1994). Dynasore, a dynamin GTPase inhibitor, blocks CME (Macia et al., 2006). As dynamin was implicated in APP endocytosis in young neurons using a dynamin mutant and dynamin dominant-negative inhibitory peptide (Carey et al., 2005; Cirrito et al., 2008), we confirmed that dynasore (100 µM) treatment reduced APP and transferrin endocytosis in mature neurons (21 DIV) (Fig. S4A-C). Next, we tested whether APP endocytosis in aged neurons requires dynamin. We observed that dynasore reduced APP endocytosis in aged neurites (Fig. 6A,B).

Formins and the Arp2/3 complex promote local F-actin polymerization during endocytic vesicle formation (Hinze and Boucrot, 2018; Soykan et al., 2017). F-actin polymerization contributes to membrane invagination, budding and scission (Picco et al., 2018). Although clathrin-independent endocytosis requires local F-actin polymerization to potentiate membrane deformation, CME is less dependent on local F-actin polymerization (Guimas Almeida et al., 2018; Picco et al., 2018). To determine whether F-actin polymerization is involved in APP endocytosis, we treated aged neurons with an Arp2/3 complex inhibitor (CK-666; 50 µM) (Hetrick et al., 2013) and a formin inhibitor (SMIFH2; 30 µM) (Isogai et al., 2015) before the APP endocytosis assay. We found that both CK-666 and SMIFH2 abrogated APP endocytosis in aged neurites (Fig. 6A,B) and in mature neurites (Fig. S4C), suggesting that APP endocytosis is dependent on actin dynamics.

Overall, these data indicate that APP endocytosis is clathrin-, dynamin- and actin-dependent in both mature and aged neurons, suggesting that the molecular endocytic machinery of APP is qualitatively unaltered by aging. Importantly, we implicate for the first time, actin polymerization in APP endocytosis. Moreover, we investigated whether Pitstop2, dynasore, CPZ, CK-666 and SMIFH2 impacted the endocytic events non-specifically identified by FM1-43 uptake (Fig. S4D,E). We found FM1-43 bulk endocytosis reduced in aged neurites but to a lesser extent than APP endocytosis, indicating that clathrin-independent endocytosis mechanisms exist in aged neurons (Fig. S4D,E).

Next, we investigated whether neuronal aging altered the levels of proteins involved in endocytosis. We measured clathrin, actin and ARPC2 (an Arp2/3 complex subunit) levels in aged neurons and aged brain. Interestingly, clathrin levels increased (50%) with aging *in vitro* and *in vivo* (Fig. 6C-F). In contrast, actin or ARPC2 levels were unaltered with aging (Fig. S5G,H,K,L).

As clathrin increased, we analyzed clathrin cellular distribution in aged neurons. Clathrin puncta density increased but not its intensity (Fig. 6G-J). Importantly, APP accumulated at clathrin puncta in aged neurons (Fig. 6K,L). Together, these results indicate that APP might be recruited more to the abundant clathrin assembly sites, suggesting that the number of APP endocytic events increases with aging.

Regarding F-actin, phalloidin F-actin labeling was inconsistent within preparations, compromising the quantification of its mean fluorescence. Instead, we analyzed F-actin presence at APP^+ endosomes. Although relatively tricky, we found F-actin puncta associated with the peripheral APP^+ endosomes, possibly closer to the plasma membrane (Fig. 6M). The quantification revealed increased F-actin puncta colocalization with APP^+ endosomes in aged neurites (Fig. 6N), suggesting an increase in F-actin for APP endocytosis in aged neurites.

There are two endocytic adaptors genetically linked to AD, CD2AP and CALM (Kanatsu and Tomita, 2017). CALM is a clathrin interactor known to regulate APP endocytosis (Xiao et al., 2012). CD2AP, an actin regulator that interacts with clathrin, regulates endocytosis in non-neuronal cells, and we showed that it controls APP endosomal sorting in young neurons (Furusawa et al., 2019; Kobayashi et al., 2004; Lehtonen et al., 2002; Lynch et al., 2003; Tang and Brieher, 2013; Ubelmann et al., 2017a; Welsch et al., 2005). We hypothesized that aging might alter CALM and CD2AP function. Indeed, we observed a CALM and CD2AP enrichment at APP^+ endosomes (Fig. 6O-Q; Fig. S5E,F). Quantification confirmed a CD2AP (87%) and CALM (82%) enrichment per APP^+ endosome in aged neurons (Fig. 6P,Q), supporting a gain in APP endocytic adaptors in aged neurons. CALM and CD2AP mean fluorescence increased in aged neurites (Fig. S5A-D), but their total levels did not change in the aged brain and aged neurons (Fig. S5G-J), not underlying their increased endosomal recruitment. Together, these data indicate an upregulation of the endocytic machinery with aging and of endocytic adaptors linked to AD that may favor APP endocytosis.

Aging-dependent synapse loss is in part due to Aβ endocytic production

Synapse dysfunction, more than neuronal death or dendritic shrinkage, has been observed in the aging brain. Synapse dysfunction is thought to account for the cognitive decline that the elderly develop and that precedes AD. It is unclear whether the Aβ in the aging brain is synaptotoxic. To establish causality between the increased intracellular Aβ42 in aged neurons, due to endocytosis upregulation and synapse decline, we needed to assess whether our aged neurons evidenced synaptic decline, as reported previously (Nwabuisi-Heath et al., 2012; Petralia et al., 2014). As a proxy for a synapse, we imaged and quantified the presynaptic marker vGlut1 (vesicular glutamate transporter 1), a glutamate transporter juxtaposition with the postsynaptic marker PSD-95 that anchors glutamate receptors at synapses. Consistent with previous studies, synapse density decreased significantly in aged neurons (Fig. 7A-D) (Nwabuisi-Heath et al., 2012; Papa et al., 1995). Given that synapse density declines in aged neurons that show increased Aβ42 production (Figs 1, 2), we hypothesized that inhibiting Aβ production could rescue age-dependent synaptic reduction.

Journal of Cell Science (2021) 134, jcs255752. doi:10.1242/jcs.255752

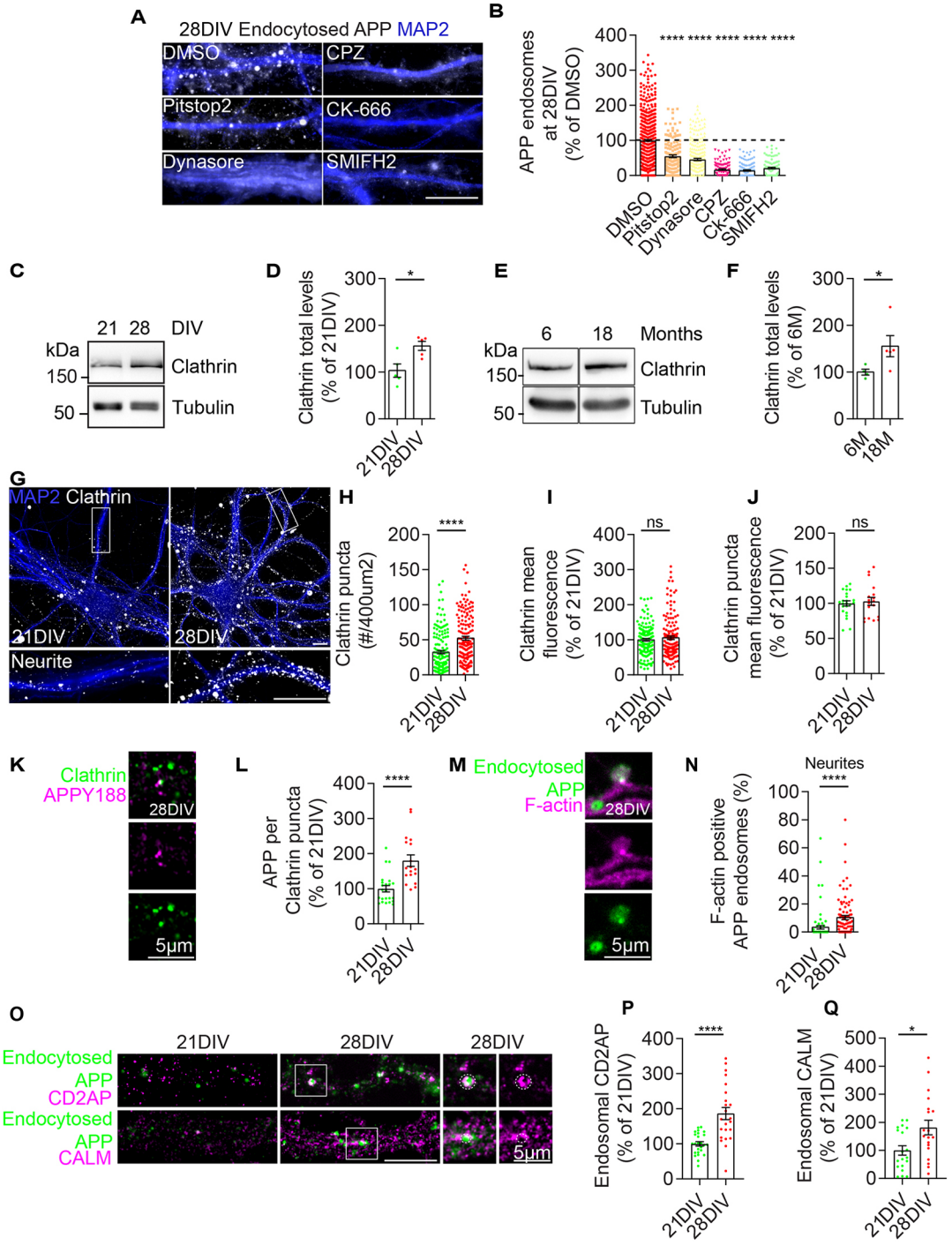

Fig. 6. APP endocytosis is sensitive to clathrin and actin inhibition. (A) Endocytosed APP (10 min) and MAP2 in neurites (28 DIV) treated with DMSO (0.1%), Pitstop2 (30 µM), CPZ (0.14 µM), dynasore (100 µM), Ck-666 (50 µM) or SMIFH2 (30 µM). (B) Quantification of APP$^+$ endosome number per area (400 µm^2) in treated neurites (28 DIV) (n=3-4, N_{DMSO}=661, $N_{Pistop2}$=145, N_{CPZ}=108, $N_{Dynasore}$=230, $N_{Ck\text{-}666}$=122, N_{SMIFH2}=98, ****P<0.0001 versus DMSO-treated neurites). (C) Western blot showing clathrin and tubulin expression in neurons (21 and 28 DIV). (D) Quantification of clathrin levels in neurons (21 and 28 DIV) (n=5). (E) Western blot showing clathrin and tubulin expression in brain (6 and 18 months). (F) Quantification of clathrin levels in brain (n=4-5). (G) Clathrin (gray) and MAP2 (blue) in neurons (21 and 28 DIV), displayed after background subtraction. The white rectangles indicate magnified neurites. (H) Quantification of clathrin puncta number per area (400 µm^2) in neurites (n=3, N=153-154). (I) Quantification of clathrin mean intensity in neurites (n=3, N=147-150). (J) Quantification of clathrin puncta mean intensity in neurites (n=3, $N_{neurons}$=21-26). (K) APP (magenta) in clathrin puncta (green) in neurites (28 DIV), displayed after background subtraction. (L) Quantification of APP mean intensity per clathrin puncta in neurites (n=3, $N_{neurons}$=21-26). (M) F-actin (magenta) colocalization with APP$^+$ endosomes (green; 10 min) in neurites (28 DIV), displayed after background subtraction. (N) Quantification of the number of F-actin and APP$^+$ endosomes in neurites (n=2, N=81-88). (O) CD2AP (magenta, top panels) or CALM (magenta, bottom panels) colocalization with APP$^+$ endosomes (green) (10 min) in neurites (21 and 28 DIV), displayed after background subtraction. White squares indicate magnified APP$^+$ endosomes (dotted circles). (P) Quantification of endosomal CD2AP, i.e. mean intensity of CD2AP per APP$^+$ endosome (n=3, $N_{neurons}$=23-25). (Q) Quantification of the endosomal CALM, i.e. mean intensity of CALM per APP$^+$ endosome (n=3, $N_{neurons}$=19). Data are mean±s.e.m. Statistical significance was determined by one-way ANOVA on ranks with post-hoc Dunn's testing (B) or by a Mann–Whitney test (D,F,H-J,L,N,P,Q). *P<0.05; ****P<0.0001; ns, not significant. Scale bars: 5 µm (K,M, inset in O); 10 µm (A,G,O).

Journal of Cell Science (2021) 134, jcs255752. doi:10.1242/jcs.255752

We treated aged neurons for 24 h with BACE inhibitor IV and γ-secretase inhibitor (DAPT), which reduced Aβ42, increased APP and altered APP CTFs (Fig. S6G-M). Notably, synapse number at 28 DIV increased significantly by 41% and 52% when treated with DAPT or BACE inhibitor IV, respectively (Fig. 7A-D). This increase indicates that inhibiting Aβ production stabilizes the synapses between 21 DIV and 28 DIV, reducing synapse loss by aged neurons.

To better understand why synapses were lost, we analyzed the density and size of each PSD-95 and vGlut1 puncta. PSD-95 and vGlut1 puncta density and size were reduced in aged neurons (Fig. S6A-D), indicating that aging affects the presynaptic and postsynaptic compartments. Treatment with BACE1 inhibitor IV improved vGlut1 and PSD-95 puncta density and size (Fig. S6A, C,D). In contrast, DAPT treatment increased vGlut1 but decreased PSD-95 puncta density without affecting their size (Fig. S6B-D). Of note, PSD-95 and vGlut1 cellular levels were unaltered in aged neurons (Fig. S6E,F). The differences observed between DAPT and BACE inhibitor IV can relate to both γ-secretase and BACE1 having substrates other than APP (Wolfe, 2019; Yan, 2017).

AMPA receptors are major players in synaptic plasticity that we and others showed reduced in fAD (Almeida et al., 2005; Baglietto-Vargas et al., 2018; Guntupalli et al., 2016) and aging (Ikonomovic et al., 2000; Pegasiou et al., 2020; Yang et al., 2015). We analyzed the AMPA receptor subunit (GluA2, also known as Gria2) mean intensity as a proxy for dendritic GluA2 and GluA2 mean intensity per F-actin puncta for synaptic GluA2 as F-actin concentration at postsynaptic compartments is very high. We found GluA2 total levels unaltered (Fig. S6E,F), but GluA2 mean fluorescence per neurite and F-actin puncta decreased with aging (Fig. 7E-G). These data indicate that a reduction in synaptic AMPA receptors accompanies the reduction in synapses. Aβ is involved in these alterations in synaptic content as DAPT treatment prevented the loss in GluA2 (Fig. 7E-G).

Our results suggest that Aβ42 production contributes to synapse loss in aged neurons *in vitro*. As the synaptic protection was not complete, it indicates that other aging mechanisms contribute to synapse decline.

Finally, we investigated whether the upregulation of endocytosis could increase intracellular Aβ and drive synaptic dysfunction in mature neurons (21 DIV). Therefore, we overexpressed Rab5a in mature neurons and observed a 31% increase in intracellular Aβ42 (Fig. 7H,I). Importantly, Rab5a overexpression was sufficient to reduce synapses density, particularly PSD-95 density and size (Fig. 7J-M). These data confirm that endocytosis upregulation recapitulates aging-dependent Aβ accumulations and synapse loss in mature neurons. Overall, we conclude that Aβ production due to endocytosis upregulation may account in part for the detrimental aging effect on synapses.

DISCUSSION

Here, we demonstrate that APP endocytosis upregulation with neuronal aging is a novel mechanism for the increase of synaptotoxic Aβ production with aging. Mechanistically, we discovered that APP endocytosis is dependent not only on clathrin and dynamin but on F-actin polymerization. The aging-dependent increase in clathrin assembly and F-actin polymerization could recruit APP endocytic adaptors to endocytic sites, upregulating APP endocytosis in aged neurons. We provide evidence that Aβ production dependent on aging but independent of fAD mutations is, in part, responsible for the synapse loss by aged neurons. Furthermore, we demonstrate that endocytosis upregulation alone is sufficient to increase Aβ42 and synapse loss. Together, our data indicate that neuronal endocytic trafficking alterations caused by aging could initiate pathological mechanisms and eventually trigger late-onset Alzheimer's disease (Fig. S7).

Intracellular Aβ42 and neuronal aging

Endogenous intracellular Aβ42 significantly increased in primary neurons aged in culture (Fig. 1), recapitulating the intracellular Aβ42 accumulation in the normal aging brain (Baker-Nigh et al., 2015; Blair et al., 2014; Kimura et al., 2005; Norvin et al., 2015). The intracellular increase in Aβ42 is likely followed by secretion in the conditioned medium of neurons aged *in vitro* (Bertrand et al., 2011; Guix et al., 2012; Kimura et al., 2005; Skovronsky et al., 1998) and by accumulation in extracellular amyloid plaques *in vivo* (Funato et al., 1998; Petersen et al., 2016; Vlassenko et al., 2011). APP processing likely contributes to the increase in intracellular Aβ42 with aging as we found APP CTFs augmented both in *in vitro* aged neurons and in *in vivo* aged brain (Fig. 2), which does not exclude the contribution of the aging-dependent reduction in Aβ degradation (Iwata et al., 2002) or extracellular Aβ endocytosis (Lai and McLaurin, 2010).

Why does APP processing increase with aging?

The aging impact on APP processing is likely independent of cellular APP alterations, which we found unaltered both *in vitro* and *in vivo* (Fig. 2), supporting similar previous observations (Flood et al., 1997; Gegelashvili et al., 1994). However, these results are not consensual as some report an increase (Guix et al., 2012; Sinha et al., 2016) and others a decrease in APP with aging (Kern et al., 2006). Increased APP processing does not seem to result from altered secretase levels (Fig. S3), as previously reported (Fukumoto et al., 2004; Guix et al., 2012). Instead, an increase in APP secretases activity could occur with aging (Fukumoto et al., 2004; Guix et al., 2012). This higher activity could be potentiated by an increase in APP access to BACE1, due to altered intracellular trafficking, secretory and endocytic, or an increase in anterograde and retrograde transport with aging (Buggia-Prévot et al., 2013; Das et al., 2016; Sannerud et al., 2016; Siman and Velji, 2003; Toh et al., 2017; Xu et al., 1997). Interestingly, Aβ42 and APP increased predominantly in aged neurites (Fig. 1), indicating altered APP trafficking, potentiating Aβ production in neurites. The increase in APP does not seem to be due to reduced APP degradation (Fig. 4) but could be due to a deficit in APP retrograde trafficking to the cell body caused by dynein malfunction with aging (Kimura et al., 2007, 2012, 2016).

We discovered a significant upregulation in APP endocytosis in aged neurons, which could explain the increase in APP processing as endocytosis is required for Aβ production (Cirrito et al., 2008; Das et al., 2016; Grbovic et al., 2003; Guimas Almeida et al., 2018; Rajendran et al., 2008; Zou et al., 2007). Importantly, we show that in aged neurons, APP localization to EEs increased *in vitro* and *in vivo* (Fig. 3). Our findings, together with several other reports, support that EEs are the leading sites for APP to encounter its secretases, where APP processing starts and likely persists during maturation into late endosomes, where Aβ accumulates (Almeida et al., 2006; Edgar et al., 2015; Morel et al., 2013; Rajendran et al., 2006; Sannerud et al., 2016; Takahashi et al., 2002, 2004; Vetrivel and Thinakaran, 2006; Willén et al., 2017; Yuyama and Yanagisawa, 2009). Therefore, we identify endocytosis as a new mechanism whereby APP processing might increase with aging.

Early endosome upregulation with neuronal aging

APP endocytosis allows it to enter EEs that harbor Rab5 and its effector EEA1. In aged neurons, an increase in enlarged EEs

Journal of Cell Science (2021) 134, jcs255752. doi:10.1242/jcs.255752

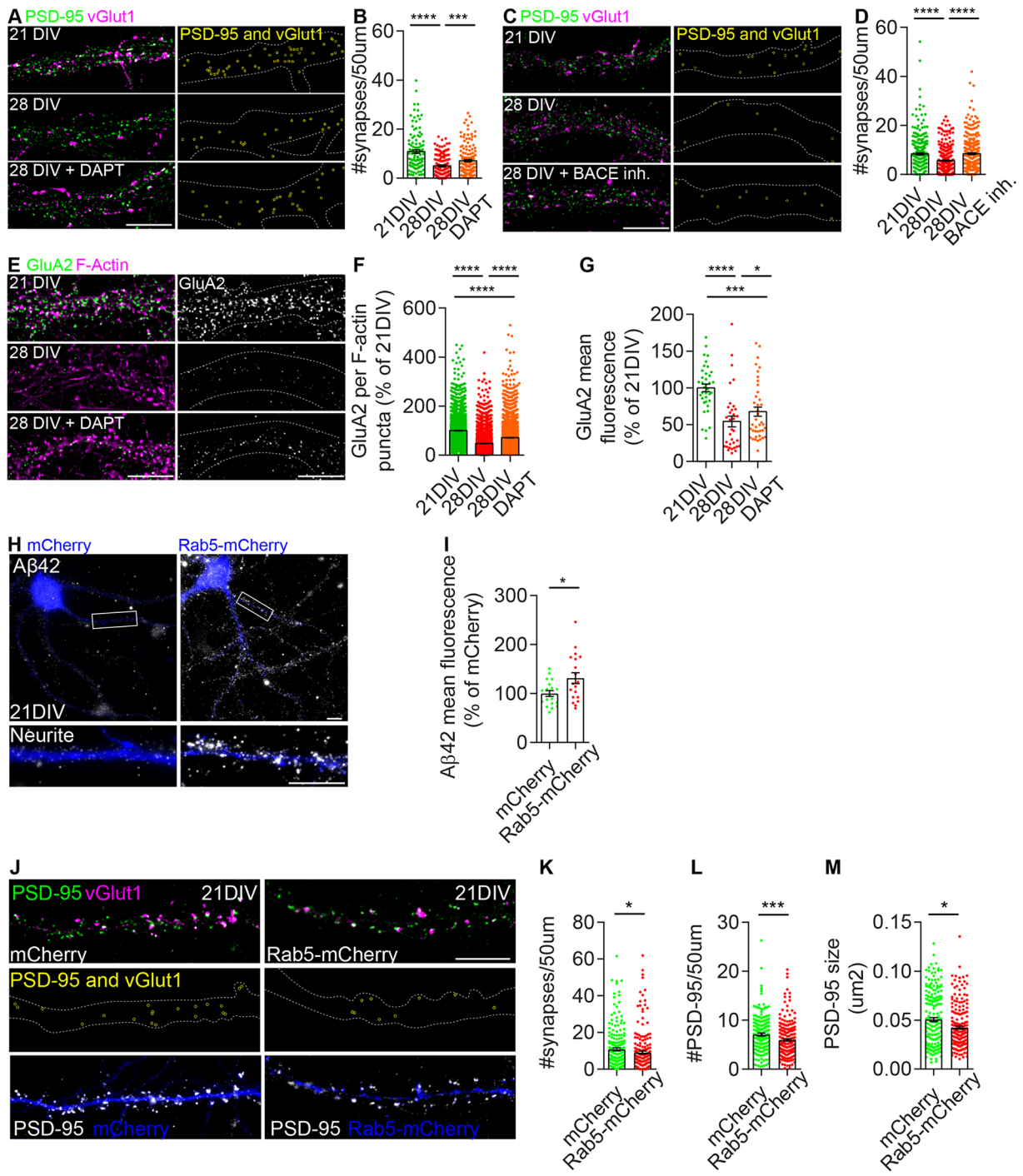

Fig. 7. Synapse loss in aged neurons is dependent on Aβ endocytic production. (A) PSD-95 (green) and vGlut1 (magenta) in 21 DIV, 28 DIV and 28 DIV neurites treated with DAPT, displayed after background subtraction. Yellow rings indicate synapses. (B) Quantification of the number of synapses per 50 µm of neurites (n=3; N_{21DIV}=118 neurites; N_{28DIV}=161 neurites; $N_{28DIV\ DAPT}$=155 neurites). (C) PSD-95 (green) and vGlut1 (magenta) in 21 DIV, 28 DIV, and 28 DIV neurites treated with BACE inhibitor IV, and displayed after background subtraction. Yellow rings indicate synapses. (D) Quantification of synapse number per 50 µm of 21 DIV, 28 DIV, and 28 DIV neurites treated with BACE inhibitor IV (n=4; N_{21DIV}=299 neurites; N_{28DIV}=341 neurites; $N_{28DIV\ BACE\ inh.}$=299 neurites). (E) GluA2 (green; gray) and F-actin (magenta) in 21 DIV, 28 DIV, and 28 DIV neurites treated with DAPT, displayed after background subtraction. (F) Quantification of GluA2 mean intensity per F-actin puncta in 21 DIV, 28 DIV, and 28 DIV neurites treated with DAPT (n=2, N_{21DIV}=2316 puncta; N_{28DIV}=2112 puncta; $N_{28DIV\ DAPT}$=2324 puncta). (G) Quantification of GluA2 mean intensity in 21 DIV, 28 DIV, and 28 DIV neurites treated with DAPT (n=2, N_{21DIV}=37 neurites; N_{28DIV}=34 neurites; $N_{28DIV\ DAPT}$=40 neurites). (H) Intracellular Aβ42 (gray) and rab5a-mCherry or mCherry (blue) in 21 DIV neurons. The white rectangles indicate magnified neurites. (I) Quantification of Aβ42 mean intensity in rab5a-mCherry- or mCherry-expressing neurites (21 DIV) (n=3, $N_{mCherry}$=19 neurites; $N_{rab5a\text{-}mCherry}$=19 neurites. (J) PSD-95 (green; gray) and vGlut1 (magenta) in rab5a-mCherry- or mCherry-expressing neurites (21 DIV). Yellow rings indicate synapses. (K) Quantification of synapse number per 50 µm of rab5a-mCherry- or mCherry-expressing neurites (21 DIV) (n=3; $N_{mCherry}$=196 neurites; $N_{rab5a\text{-}mCherry}$=191 neurites). (L) Quantification of PSD-95 puncta number per 50 µm of rab5a-mCherry- or mCherry-expressing neurites (21 DIV) (n=3; $N_{mCherry}$=190 neurites; $N_{rab5a\text{-}mCherry}$=200 neurites). (M) Quantification of PSD-95 puncta mean size (µm^2) in mCherry- or rab5a-mCherry expressing neurites (21 DIV) (n =3, $N_{mCherry}$=190 neurites; $N_{rab5a\text{-}mCherry}$=200 neurites). Data are mean±s.e.m. Statistical significance was determined by a Mann–Whitney test (B, D, F,G,K-M) or an unpaired t-test (I). *P<0.05, ***P<0.001, ****P<0.0001. Scale bars: 10 µm.

accompanied APP endocytosis upregulation *in vitro* and *in vivo* (Figs 2, 3). This EE upregulation in normal aged neurons is supported by one report (Blanpied et al., 2003). In contrast, another report showed no change in $Rab5^+$ EEs, but few post-mortem cognitively normal human brains were analyzed (Cataldo et al., 2000). However, enlarged EEs are easily detected early in sporadic AD and Down Syndrome (Cataldo et al., 2000). It would be interesting to analyze EEs in a larger group of aged individuals also using EEA1.

EE upregulation likely results from a general increase in endocytosis and endocytic vesicle fusion, as despite a major increase in APP endocytosis, LDL and FM1-43 bulk endosomes increased in aged neurons (Figs 4, 5). More specific seems to be the reduction in transferrin endocytosis and TfR in aged neurons and aged brain (Fig. 5), which are consistent with the reduced rate of transferrin exit from endocytic clathrin-coated pits in aged neurons (Blanpied et al., 2003), the receptor-reduced expression in aged hippocampus (Lu et al., 2017) and a homeostatic adaptation to aging-dependent changes in iron uptake (Malorni et al., 1998). However, we do not exclude the contribution of an endosomal maturation deficit, despite APP degradation not being altered (Fig. 4). From a different perspective, the augmented EEA1 recruitment to EEs could be due to increased Rab5 activation with aging (Ginsberg et al., 2011; Neefjes and van der Kant, 2014). Overall, our findings indicate that increased endocytic uptake leads to EE enlargement.

How does APP endocytosis increase with aging?

No previous study observed directly that neuronal aging increases APP endocytosis, but the increased endocytic protein levels in the aged human brain supports it (Alsaqati et al., 2017). APP endocytosis is known to be clathrin- and dynamin-dependent (Cirrito et al., 2008; Cossec et al., 2010; Koo and Squazzo, 1994; Marquez-Sterling et al., 1997; McMahon and Boucrot, 2011). Here, we used a pharmacological approach to dissect APP endocytosis mechanisms. We used two inhibitors of CME, CPZ (Wang et al., 1993), a clathrin assembly inhibitor in endocytic sites and previously shown to inhibit Aβ release (Cirrito et al., 2008), and Pitstop2 (Dutta et al., 2012), previously shown to decrease β- and γ-secretase endocytosis (Chia et al., 2013; Kanatsu et al., 2014; Kuboyama et al., 2015). Both CPZ and Pitstop2 reduced APP endocytosis in aged neurons, indicating that aging-dependent APP endocytosis is sensitive to clathrin inhibition (Fig. 6). The clathrin-coated endocytic vesicle scission occurs by dynamin polymerization upon GTP hydrolysis. We found that similar to expressing dynamin mutants (Carey et al., 2005) or other dynamin inhibitors (Cirrito et al., 2008), dynasore treatment, which inhibits dynamin function, inhibited APP endocytosis independently of aging (Fig. 6; Fig. S4). Actin polymerization has an auxiliary function in canonical CME (Boulant et al., 2011; Picco et al., 2018). We used two inhibitors of actin polymerization, CK-666 and SMIFH2, and found that both are extremely potent in inhibiting APP endocytosis, independently of aging. Interestingly, F-actin polymerization inhibition prevented APP endocytosis the most consistently (Fig. 6).

The mechanism used by aged neurons to endocytose APP involves clathrin, dynamin and F-actin, and does not seem qualitatively different from young neurons. The difference in aged neurons may be the quantity of clathrin assembly at endocytic sites as we found clathrin levels increased in aged neurons and the normal aged brain (Fig. 6), consistent with previous observations (Alsaqati et al., 2017; Blanpied et al., 2003; Kimura et al., 2012). Thus, the upregulation in APP endocytosis correlates with the increase in clathrin assembly and F-actin polymerization, which would translate in a general endocytosis upregulation but does not exclude a specific increase in APP endocytosis through the recruitment of APP endocytic adaptors, CD2AP and CALM, which we observed increase at APP^+ endosomes in aged neurons (Fig. 6; Fig. S5). Interestingly, PICALM encodes CALM and is a late-onset AD risk gene (Carmona et al., 2018; Harold et al., 2009), which has been reported to increase with normal aging *in vivo* (Alsaqati et al., 2017). CD2AP, a membrane-associated scaffolding protein and a late-onset AD risk gene (Carmona et al., 2018; Harold et al., 2009; Hollingworth et al., 2011; Kunkle et al., 2019; Naj et al., 2011), is implicated in endocytosis (Kobayashi et al., 2004; Lynch et al., 2003), actin cytoskeleton regulation (Lehtonen et al., 2002; Tang and Brieher, 2013; Welsch et al., 2005) and as a regulator of APP sorting for degradation (Furusawa et al., 2019; Ubelmann et al., 2017a). As CD2AP binds actin and controls its stability, it could be stabilizing F-actin to facilitate APP endocytosis. Together, our data support a quantitative increase in clathrin- and F-actin-sensitive APP endocytosis with neuronal aging.

Synapse dysfunction in aging and Alzheimer's disease

Although the Aβ accumulation is concomitant with synapse dysfunction in the aging brain, it is unclear whether causality exists. Here, we found that Aβ production inhibition increases synapse number and glutamate receptors in aged neurons, in agreement with our previous data from fAD neurons (Almeida et al., 2005; Takahashi et al., 2004). Moreover, we discovered that APP CTF accumulation after γ-secretase inhibition is not linked to synapse decline in aged neurons as suggested in fAD models (Bittner et al., 2009). However, other mechanisms could contribute to synapse loss during aging (Yankner et al., 2008). Importantly, we found that endocytosis upregulation in mature neurons increased Aβ and synapse loss, recapitulating the phenotype of aged neurons (Fig. 7).

Overall, our findings indicate that APP endocytosis upregulation is an autonomous cell mechanism by which neurons contribute to brain aging. The next step will be to use new methods for measuring endocytosis in neurons *in vivo* and other brain cells.

Our work highlights the involvement of APP endocytosis as a critical link between aging and AD. The increased APP processing and Aβ42 accumulation point to an impairment in endocytic trafficking towards EEs as neurons age. We found that the detrimental aging effect on synapses accounts, at least in part, to Aβ production. Hence, the mechanisms underlying aging-dependent synaptic decline need to be urgently identified to reverse synaptic dysfunction, prevent cognitive decline in the face of aging and delay AD.

MATERIALS AND METHODS

Animals

All animal procedures (without live experimentation) were performed according to EU recommendations and were approved by the Instituto Gulbenkian de Ciência Animal Care and Ethical Committee, the NMS–Universidade Nova de Lisboa ethical committee (07/2013/CEFCM) and the national DGAV (Direção-Geral da Alimentação e Veterinária; 0421/000/000/2013).

Cell culture

Primary neuronal cultures from *Mus musculus* were prepared as reported previously (Almeida et al., 2005) from cortices of embryonic day 16 (E16) wild-type females and male BALB/c mice (Instituto Gulbenkian de Ciência and CEDOC), C57Bl/6J (Jackson Labs, Maine, USA, JAX 000664) and

APP KO (Jackson Labs, Maine, USA, JAX 004133). Briefly, E16 brain tissue was dissociated by trypsinization and trituration in Dulbecco's medium Eagle medium (DMEM) with 10% fetal bovine serum (Heat-Inactivated FBS, Thermo Fisher Scientific). Dissociated neurons were plated in DMEM with 10% FBS on poly-D-lysine (Sigma-Aldrich)-coated six-well plates (1×10^5 cells/cm^2) and glass coverslips (2.6×10^4 cells/cm^2). After 3-16 h, the medium was substituted for Neurobasal medium supplemented with B27, GlutaMAX, and penicillin/streptomycin (all from Life Technologies) at 37°C in 5% CO_2. Cells were maintained up to 28 DIV without changing or adding new medium. We only used cultures that presented minimal glia.

For cDNA expression, primary neurons (12 DIV) were transiently transfected with 1 µg of cDNA with Lipofectamine 2000 (Life Technologies). Cells were analyzed at 21 DIV. When indicated, γ-secretase was inhibited by 24 h of treatment with 250 nM DAPT (Calbiochem), BACE1 was inhibited by 24 h treatment with 10 µM compound IV (Calbiochem), and DMSO (0.1%; solvent; PanReac AppliChem) was used as a control.

cDNA

We used DNA plasmids encoding mCherry and Rab5a-mCherry (obtained from M. Arpin, Institut Curie, Paris, France).

Antibodies

The following primary antibodies were used: anti-Ankyrin-G pAb (P-20, Santa Cruz Biotechnology, sc-31778, 1:100); anti-APP mAb (22C11, Millipore, MAB348, 1:100); anti-APP [Y188, GeneTex, GTX61201, 1:200 (immunofluorescence, IF); 1:1000 (western blot, WB)]; anti-Aβ42 mAb (12F4, Millipore, 05-831-l, 1:50); anti-Aβ40 pAb (Merck Millipore, AB5074P, 1:100); anti-BACE1 pAb (Thermo Scientific, PA1-757, 1:850); anti-EEA1 pAb [N-19, Abcam, sc-6415, 1:50 (IF); 1:1000 (WB) or mAb C45B10, Cell Signaling Technology, #3288, 1:1000 (WB)]; anti-MAP2 mAb [Sigma-Aldrich, M4403, 1:500 (IF); 1:1000 (WB)]; anti-nicastrin pAb (Thermo Scientific, PA1- 758, 1:500); anti-tubulin mAb (Tu-20, Millipore, MAB1637, 1:10,000); anti-LAMP1 mAb (CD107a, BD Pharmingen, 553792; 1:200); anti-Rab5a pAb (Sicgen, AB1024-200, 1:200); anti-GAPDH mAb (Ambion, AM4300, 1:1000); anti-PSD-95 mAb [Merck Millipore, 04-1066, 1:200 (IF); 1:1000 (WB)]; anti-vGlut1 mAb [Merck Millipore, MAB5502, 1:200 (IF); 1:1000 (WB)]; anti-GluA2 mAb [Merck Millipore, MABN71, 1:200 (IF); 1:1000 (WB)]; anti-CALM pAb [Sigma-Aldrich, HPA019053, 1:250 (IF); 1:1000 (WB)]; anti-CD2AP pAb [Santa Cruz Biotechnology, sc-9137, 1:100 (IF) or Sigma-Aldrich, HPA003326, 1:500 (WB)]; anti-clathrin heavy chain mAb [BD Biosciences, 610499, 1:50 (IF); 1:1000 (WB)]; anti-ArpC2 pAb (GeneTex, GTX101984, 1:1000); anti-TfR mAb [Thermo Scientific, 13-6800, 1:250 (IF); 1:500 (WB)]; anti-actin mAb (Sigma-Aldrich, A2228, 1:10,000); anti-GFAP mAb [Merck Millipore, MAB3402, 1:1000 (WB)]; anti-Rab11a mAb {Abcam, [EPR7587(B)]; ab128913, 1:10,000 [WB]}; and anti-doublecortin pAb [Santa Cruz Biotechnology, (C-18), sc-8066, 1:1000 (WB)]. For immunohistochemistry, the following antibodies were used: anti-APP (Y188, GeneTex, GTX61201, 1:500); anti-EEA1 (N-19, Abcam, sc-6415, 1:300); and anti-Rab5a (Sicgen, AB1024-200, 1:300). The secondary antibodies used were conjugated to Alexa Fluor 488, 555 and 647 (Molecular Probes), or to horseradish peroxidase (HRP, Bio-Rad).

Immunofluorescence labeling

Immunofluorescence was performed as described previously (Almeida et al., 2005; Ubelmann et al., 2017a). Briefly, cultured primary neurons were fixed at 14, 19, 21 and 28 DIV with 4% paraformaldehyde/4% sucrose in PBS for 20 min, permeabilized with 0.1% saponin in PBS for 1 h and blocked in 2% FBS/1% bovine serum albumin (BSA)/0.1% saponin in PBS for 1 h at room temperature before antibody incubation using a standard procedure. For PSD-95, vGlut1 and Rab5a immunolabeling, permeabilization was performed with 0.3% Triton X-100 in PBS for 5 min at room temperature. Coverslips were mounted using Fluoromount-G (Southern Biotechnology, Birmingham, AL, USA) or Slowfade gold antifade reagent (Thermo Fisher Scientific, Sweden).

Image acquisition

Epifluorescence microscopy was carried out on an upright microscope Z2 (Zeiss) equipped with a 60× NA-1.4 oil immersion objective and an AxioCam MRm charged-coupled device (CCD) camera (Zeiss) on an upright microscope DMRA2 (Leica) equipped with a 100× NA-1.4 oil immersion objective and a CoolSnap HQ camera (Photometrics), or on an inverted IX70 microscope (Olympus) equipped with a 100× NA-1.25 oil immersion objective and a Hamamatsu ORCA-flash4.0 LT plus camera (Hamamatsu). Confocal microscopy was performed with a LSM 710 confocal microscope (Zeiss), a Revolution xD (Andor) spinning-disk system coupled to an Eclipse Ti-E microscope (Nikon) or a LSM 980 confocal microscope (AiryScan 2, Zeiss). Samples were imaged in two dimensions, with the focus plane chosen based on signal sharpness and best signal to noise ratio, in parallel, and using identical acquisition parameters for direct comparison.

Immunoblotting

Cell lysates were prepared using modified RIPA buffer [50 mM Tris-HCl (pH 7.4), 1% NP-40, 0.25% sodium deoxycholate, 150 mM NaCl, 1 mM EGTA, and 0.1% SDS, with protease inhibitor cocktail (PIC)]. Proteins separated by 7.5, 10, 15%, 4-12% Tris-glycine SDS-PAGE (Invitrogen) or 12% NuPAGE Bis-Tris SDS-PAGE (Invitrogen, NP0341BOX) were transferred to nitrocellulose membranes (GE Healthcare) and processed for immunoblotting using an ECL Prime kit (GE Healthcare). Images of immunoblots were captured using a ChemiDoc Gel Imaging System (Bio-Rad) within the linear range and quantified by densitometry using the 'Analyse gels' function in ImageJ.

β-CTF/C99 blots

To detect levels of β-CTF/C99 and C89/C83/C191 in primary mouse cortical neurons (Fig. 2; Fig. S6), 10 µg of cell extracts were prepared in reducing sample buffer containing 10% β-mercaptoethanol and boiled at 95°C for 5 min. Samples were resolved on a 12% NuPAGE Bis-Tris SDS-PAGE at 125 V for ∼2 h. Transfer of proteins onto a 0.2-µm nitrocellulose membrane (GE Healthcare) was conducted at 10 V for 1 h. The membrane was incubated overnight at 4°C with Y188 antibodies diluted in PBS Tween 20 (1:1000) and washed four times with PBS Tween 20 for 5 min per wash. The membrane was then incubated with 1:5000 diluted secondary antibodies conjugated with HRP for 1 h and washed as above. Bound antibodies were detected and imaged as described in the 'Immunoblotting' section.

Senescence-associated β-gal assay

We used the Senescence β-Galactosidase Staining kit (9860; Cell Signaling Technology) to detect β-galactosidase activity (Fig. 1). In brief, cells were fixed in the fixative solution for 10-15 min at room temperature. The fixed cells were then incubated with β-galactosidase staining solution containing X-gal at 37°C overnight (18 h). As the blue color developed, bright-field cell images were taken using an upright microscope Z2 (Zeiss) connected to an AxioCam MRm CCD camera (Zeiss).

Enzyme-linked immunosorbent assays

Secreted murine endogenous Aβ1-40 and Aβ1-42 from primary neurons at steady state were measured from the medium collected with PIC after 21 or 28 DIV using an ELISA kit specifically for murine Aβ40 and Aβ42 (Invitrogen, KMB3481 and KMB3441). Each sample was measured in duplicate using a SpectraMax i3x microplate reader (Molecular Devices). For each sample, values were normalized for protein concentration measured using the BCA Protein Assay Kit (Thermo Scientific, 23225).

Trafficking assays

For bulk endocytosis (Fig. 5), a 10-min pulse with FM1-43 was performed. FM1-43 is a fluorescent styryl dye that binds to the plasma membrane from which it can be endocytosed. Once at endosomes, it is protected from removal from the plasma membrane by washing (Fomina et al., 2003). Specifically, neurons were incubated with FM1-43Fx (Thermo Fisher Scientific, F-35355) in a complete medium at a final concentration of 10 µM for 10 min (pulse) at 37°C. Cells were then fixed, washed and mounted.

For bulk endocytosis inhibition (Fig. S4), neurons were previously incubated at 37°C with 30 µM Pitstop2 (Sigma-Aldrich, SML1169) for 15 min, 100 µM dynasore (Sigma-Aldrich, 7693) for 10 min, 0.14 µM chlorpromazine hydrochloride (Sigma-Aldrich, c8138) for 10 min, 50 µM CK-666 (Merck, SML0006) for 5 min, and 30 µM SMIFH2 (Merck, S4826) for 5 min. For bulk endocytosis of biotinylated APP (Fig. 4), biotinylation of surface APP was performed as described previously (Almeida et al., 2006). Briefly, neurons at 21 DIV and 28 DIV were incubated on ice with 0.5 mg/ml Sulfo-NHS-LC-Biotin (Pierce) in PBS for 30 min. Free biotin was quenched with ice-cold 0.5% BSA in PBS. Biotinylated proteins were chased for 10 min and 30 min at 37°C to allow the detection of endocytosis. For the detection of surface biotin-APP, cells were rinsed, and lysates were prepared in RIPA buffer. For the detection of endocytosed biotin-APP, surface biotin was stripped by treating cells with GSH (50 mM) in stripping buffer [(75 mM NaCl, 10 mM EGTA, 1% BSA (pH 7.8-8.0)] for 15 min on ice before lysate preparation. Biotinylated proteins were immunoprecipitated with NeutrAvidin agarose beads (Pierce) overnight at 4°C and, after washing, separated by SDS-PAGE. Quantitative immunoblotting of biotinylated proteins and total proteins was performed using the anti-APP (Y188) antibody.

For APP endocytosis (Fig. 4), a 10-min pulse with a monoclonal mouse antibody against the extracellular N-terminus of surface APP (22C11) was performed as described previously (Ubelmann et al., 2017b). After a 10-min pulse at 37°C in complete medium with 10 mM HEPES, cells were fixed and immunolabeled with a secondary anti-mouse IgG antibody and mounted, or co-labeled for Rab5a (Fig. S3), Rab11a (Fig. S3), CD2AP, CALM or Phalloidin to probe F-actin (Fig. 6), then washed and mounted.

For surface APP (Fig. 4), cells were fixed, non-permeabilized and immunolabeled with 22C11 primary antibody and a secondary anti-mouse IgG antibody. After washing, immunofluorescence labeling of APPY188 was performed as described previously in the 'Immunofluorescence labeling' section.

For APP recycling (Fig. S3), cells pulsed for 10 min with 22C11 at 37°C were acid stripped (0.5 M NaCl, 0.2 M acetic acid; 5 s) and quickly rinsed in PBS before chasing for 20 min at 37°C. Cells were rinsed with PBS before 5 min fixation with 4% paraformaldehyde/4% sucrose in PBS, and recycled APP was immunolabeled without permeabilization. Upon immunolabeling, cells were rinsed with PBS before 15 min fixation with 4% paraformaldehyde/4% sucrose in PBS, followed by washing and mounting.

For APP endocytosis inhibition (Fig. 6), neurons were previously incubated at 37°C with 30 µM Pitstop2 (Sigma-Aldrich, SML1169) for 15 min, 100 µM dynasore (Sigma-Aldrich, 7693) for 10 min; 0.14 µM chlorpromazine hydrochloride (Sigma-Aldrich, c8138) for 10 min, 50 µM CK-666 (Merck, SML0006) for 5 min, and 30 µM SMIFH2 (Merck, S4826) for 5 min.

For transferrin endocytosis (Fig. 5), a 10-min pulse with transferrin was performed as described previously (Almeida et al., 2006). Briefly, neurons were incubated with 10 µg/ml transferrin labeled with Alexa Fluor 647 (A647-Tf; Life Technologies, T23366) in a complete medium with 10 mM HEPES for 10 min (pulse) at 37°C. Next, cells were fixed, permeabilized and labeled with Phalloidin to probe F-actin, then washed and mounted.

For acetylated LDL (A488-AcLDL) endocytosis (Fig. 5), neurons were incubated with Low-Density Lipoprotein From Human Plasma, acetylated, Alexa Fluor 488 conjugate (AcLDL) (10 µg/ml, Invitrogen L23380) in complete medium for 30 min (pulse) at 37°C. Cells were then fixed, washed and mounted.

Quantitative analyses

Image analyses were carried out using ImageJ (imagej.nih.gov/ij), Fiji (Fiji.sc) or ICY (icy.bioimageanalysis.org; de Chaumont et al., 2012). For the quantification of the number of autofluorescent granules positive for LAMP1 (Fig. 1) and autofluorescent granules (Fig. S1) per area of the dendrite (density), dendritic segments were outlined with ICY. LAMP1 and autofluorescent granules were segmented and counted automatically using the ICY 'spot detector' plug-in. The number of colocalizations (lysosomal lipofuscin) was obtained using the ICY 'colocalization studio-SODA' plug-in (Lagache et al., 2018).

For the subcellular quantification of intracellular Aβ42 levels (Fig. 1; Fig. S6), Aβ40 levels (Fig. S2) and APP levels (Fig. 1; Fig. S3, Fig. S6), the mean fluorescence of Aβ42/Aβ40/APP in neurites was measured using ImageJ. A region of the background was outlined using 'polygon selection'. For selecting a region of neurites, a square (500×500) was centered on each primary dendrite. The mean fluorescence of Aβ42/Aβ40/APP in each region was quantified with the 'measure' function. The mean fluorescence per region was calculated as a percentage of the indicated control upon background fluorescence subtraction.

For the quantification of APP levels in axons versus dendrites (Fig. S1), two subcellular regions of interest (ROI), axons ($AnkG^+$) and dendrites ($AnkG^-$), were outlined using ImageJ 'polygon selection'. The mean fluorescence of APP in each ROI was quantified as above. For the quantification of APP polarization, APP mean fluorescence in the axon ROI was divided by the APP mean fluorescence in the dendrite ROI (APP axon/dendrite ratio). APP mean fluorescence in axons versus dendrites was calculated as above.

For the quantification of APP colocalization with EEA1 or LAMP1 density per area (Fig. 3), APP^+ endosomes (22C11) colocalization with Rab5a or Rab11a percentage (Fig. S3), APP^+ endosomes (22C11) colocalization with F-actin percentage (Fig. 6), and PSD-95 colocalization with vGlut1 (synapse) density per length of neurite (Fig. 7), the number of colocalizing objects were obtained using ICY 'colocalizer' protocol or with 'Colocalization Studio – SODA' (Lagache et al., 2018). The area or length (Feret's diameter) of the neurite ROI was obtained using ICY ROI export.

For the quantification of puncta density per area, intensity and size of APP^+ endosomes (22C11), EEA1, Rab5a, APP, clathrin, PSD-95, vGlut1, FM1-43, transferrin (A647-Tf) and A488-AcLDL (Figs 3, 4, 5, 6, 7; Fig. S4, Fig. S6), the ICY 'spot detector' was used. For Rab5a quantification of puncta density per area, intensity and size, images were deconvolved with Huygens Essential version 20.10 (Scientific Volume Imaging, The Netherlands, http://svi.nl), using the CMLE algorithm, with SNR:10 and 25 iterations.

For the quantification of APP surface levels, several neurite regions were outlined using the 'polygon selection' tool based on neuronal morphology. The average fluorescence of APP in each region and of a background region was quantified using the 'measure' function. Upon background fluorescence subtraction, the average fluorescence per region was calculated as the percentage of 21 DIV neurons.

For the quantification of the mean fluorescence of clathrin (Fig. 6), CALM (Fig. S5), CD2AP (Fig. S5), TfR (Fig. 5) and GluA2 (Fig. 7) levels in neurites, subcellular ROI were outlined using ICY 'region of interest- 2D ROI – Area'. The mean fluorescence in each ROI was quantified using ICY ROI export.

For the quantification of early endosomal APP *in vivo* (Fig. 3), endosomal rab5a enrichment (Fig. S3), APP per clathrin puncta (Fig. 6), endosomal CD2AP and CALM enrichment (Fig. 6), or GluA2 per F-actin puncta (Fig. 7), puncta were segmented, and ROIs created using the ICY 'spot detector' plugin and the mean fluorescence per spot in each ROI was obtained using ICY ROI export.

For the quantification of intracellular Aβ42 upon cDNA expression, all neurites were outlined using the ICY 'thresholder plug-in based on mCherry/Rab5a-mCherry signal and on neuronal morphology. The average fluorescence of Aβ42 in all neurites, excluding cell body, and of a background region, was obtained using ICY ROI export. Upon background fluorescence subtraction, the average fluorescence on neurites was calculated as the percentage of the control (mCherry).

Brain homogenates preparation

Frozen forebrains (including cortex and hippocampus) from 6-month-old (adult) and 18-month-old (aged) C57BL/6J mice were solubilized using a modified RIPA buffer. After 15 min on ice with RIPA buffer, brains were homogenized by sonication and centrifuged at 4°C for 30 min. Equivalent amounts of protein (40 µg), as determined by the BCA protein assay kit (Thermo Fisher Scientific), were mixed with sample buffer, heated at 95°C for 5 min, vortexed and run on a 4-12% Tris-glycine SDS-PAGE (Invitrogen). Electrophoretic transfer and immunoblotting were performed as described above.

Brain immunohistochemistry

Histology was performed on fixed gelatin-embedded forebrains of the left brain hemispheres of 12-month-old (adult) and 18-month-old (aged) mice. Transverse 40 µm sections were sliced on a microtome (Cryostat Leica CM3050 S). Sections were washed in 0.1 M phosphate buffer, permeabilized with 0.3% Triton X-100 in 0.1 M phosphate buffer for 10 min at room temperature, and blocked in 0.3% Triton X-100/5% BSA in 0.1 M phosphate buffer for 1 h at room temperature before primary antibody incubation in blocking solution overnight at 4°C. The secondary antibodies used were conjugated to Alexa Fluor 488 and 555 (Molecular Probes). Coverslips were then mounted using Fluoromount-G (Southern Biotechnology, Birmingham, AL, USA).

Statistics

GraphPad Prism 8 was used for graphic representation of individual replicates with mean±s.e.m. and for statistical analysis of at least three independent experiments, as indicated in figure legends. The sample size was determined based on pilot studies. Data were tested with the D'Agostino-Pearson omnibus normality test. For parametric and paired data, the paired *t*-test was applied; for non-parametric and paired data, the Wilcoxon *t*-test was applied; for non-parametric and unpaired data, the Mann–Whitney or Kolmogorov–Smirnov test was applied; for non-parametric and multiple comparisons statistical analysis of data, one-way ANOVA on ranks with post-hoc Dunn's testing was applied. The exact *P* values are listed in Table S1.

Acknowledgements

We thank M. Arpin and S. Miserey-Lenkei (Institut Curie), I. Araújo (Universidade do Algarve), and CEDOC colleagues for reagents; M. Guimarães and D. Rodrigues for technical assistance; L. Almeida for Excel macro; lab members for helpful discussions; H. Miranda, A. Gontijo (CEDOC) and E. Gomes (Instituto de Medicina Molecular, iMM) for critically reading the manuscript; and A. Farinho (CEDOC-Histology), S. Marques (CEDOC-Vivarium) and T. Pereira (CEDOC-Microscopy) for support.

Competing interests

The authors declare no competing or financial interests.

Author contributions

Conceptualization: T.B., C.G.A.; Methodology: T.B., C.G.A.; Formal analysis: T.B., C.G.A.; Investigation: T.B., I.M., R.G., A.P.T., C.G.A.; Writing - original draft: T.B., C.G.A.; Writing - review & editing: T.B., C.G.A.; Visualization: C.G.A.; Supervision: G.K.G., C.G.A.; Funding acquisition: G.K.G., C.G.A.

Funding

This work was supported by Marie Curie Actions-EC (PCIG–GA–2012–334366–trafficinAD); iNOVA4Health (UID/Multi/04462/2019-FCT/MCTES/PT2020); Maratona da Saúde-2016; the Alzheimer's Association (AARG-19-618007); the Portuguese Platform of BioImaging funded by the Fundação para a Ciência e a Tecnologia/Lisboa2020/PT2020 (PPBI-POCI-01-0145-FEDER-022122); Horizon 2020 Framework Programme (H2020 GA811087-Lysocil); and C.G.A. salary funded by Fundação para a Ciência e a Tecnologia (CEECIND/00410/2017). A.P.T. and T.B. were supported by fellowships from Fundação para a Ciência e a Tecnologia (SFRH/BD/52473/2014 and SFRH/BD/131513/2017). I.M. and G.K.G. received support from the Vetenskapsrådet.

Peer review history

The peer review history is available online at https://journals.biologists.com/jcs/article-lookup/doi/10.1242/jcs.255752

References

Acevedo, K. M., Hung, Y. H., Dalziel, A. H., Li, Q.-X., Laughton, K., Wikhe, K., Rembach, A., Roberts, B., Masters, C. L., Bush, A. I. et al. (2011). Copper promotes the trafficking of the amyloid precursor protein. *J. Biol. Chem.* **286**, 8252-8262. doi:10.1074/jbc.M110.128512

Aksenova, M. V., Aksenov, M. Y., Markesbery, W. R. and Butterfield, D. A. (1999). Aging in a dish: age-dependent changes of neuronal survival, protein oxidation, and creatine kinase BB expression in long-term hippocampal cell culture. *J. Neurosci. Res.* **58**, 308-317. doi:10.1002/(SICI)1097-4547(19991015)58:2<308::AID-JNR11>3.0.CO;2-#

Almeida, C. G., Tampellini, D., Takahashi, R. H., Greengard, P., Lin, M. T., Snyder, E. M. and Gouras, G. K. (2005). Beta-amyloid accumulation in APP mutant neurons reduces PSD-95 and GluR1 in synapses. *Neurobiol. Dis.* **20**, 187-198. doi:10.1016/j.nbd.2005.02.008

Almeida, C. G., Takahashi, R. H. and Gouras, G. K. (2006). Beta-amyloid accumulation impairs multivesicular body sorting by inhibiting the ubiquitin-proteasome system. *J. Neurosci.* **26**, 4277-4288. doi:10.1523/JNEUROSCI.5078-05.2006

Alsaqati, M., Thomas, R. S. and Kidd, E. J. (2017). Proteins involved in endocytosis are upregulated by ageing in the normal human brain: implications for the development of Alzheimer's disease. *J. Gerontol. A Biol. Sci. Med. Sci.* **73**, 289-298. doi:10.1093/gerona/glx135

Andersen, O. M., Schmidt, V., Spoelgen, R., Gliemann, J., Behlke, J., Galatis, D., McKinstry, W. J., Parker, M. W., Masters, C. L., Hyman, B. T. et al. (2006). Molecular dissection of the interaction between amyloid precursor protein and its neuronal trafficking receptor SorLA/LR11. *Biochemistry* **45**, 2618-2628. doi:10.1021/bi052120v

Baglietto-Vargas, D., Prieto, G. A., Limon, A., Forner, S., Rodriguez-Ortiz, C. J., Ikemura, K., Ager, R. R., Medeiros, R., Trujillo-Estrada, L., Martini, A. C. et al. (2018). Impaired AMPA signaling and cytoskeletal alterations induce early synaptic dysfunction in a mouse model of Alzheimer's disease. *Aging Cell* **17**, e12791. doi:10.1111/acel.12791

Baker-Nigh, A., Vahedi, S., Davis, E. G., Weintraub, S., Bigio, E. H., Klein, W. L. and Geula, C. (2015). Neuronal amyloid-β accumulation within cholinergic basal forebrain in ageing and Alzheimer's disease. *Brain* **138**, 1722-1737. doi:10.1093/brain/awv024

Bertrand, S. J., Aksenova, M. V., Aksenov, M. Y., Mactutus, C. F. and Booze, R. M. (2011). Endogenous amyloidogenesis in long-term rat hippocampal cell cultures. *BMC Neurosci.* **12**, 38. doi:10.1186/1471-2202-12-38

Bigagli, E., Luceri, C., Scartabelli, T., Dolara, P., Casamenti, F., Pellegrini-Giampietro, D. E. and Giovannelli, L. (2016). Long-term neuroglial cocultures as a brain aging model: hallmarks of senescence, MicroRNA expression profiles, and comparison with In Vivo models. *J. Gerontol. A Biol. Sci. Med. Sci.* **71**, 50-60. doi:10.1093/gerona/glu231

Bittner, T., Fuhrmann, M., Burgold, S., Jung, C. K. E., Volbracht, C., Steiner, H., Mitteregger, G., Kretzschmar, H. A., Haass, C. and Herms, J. (2009). Gamma-secretase inhibition reduces spine density *in vivo* via an amyloid precursor protein-dependent pathway. *J. Neurosci.* **29**, 10405-10409. doi:10.1523/JNEUROSCI.2288-09.2009

Blair, J. A., Siedlak, S. L., Wolfram, J. A., Nunomura, A., Castellani, R. J., Ferreira, S. T., Klein, W. L., Wang, Y., Casadesus, G., Smith, M. A. et al. (2014). Accumulation of intraneuronal amyloid-β is common in normal brain. *Curr. Alzheimer Res.* **11**, 317-324. doi:10.2174/1567205011666140302200902

Blanpied, T. A., Scott, D. B. and Ehlers, M. D. (2003). Age-related regulation of dendritic endocytosis associated with altered clathrin dynamics. *Neurobiol. Aging* **24**, 1095-1104. doi:10.1016/j.neurobiolaging.2003.04.004

Boulant, S., Kural, C., Zeeh, J.-C., Ubelmann, F. and Kirchhausen, T. (2011). Actin dynamics counteract membrane tension during clathrin-mediated endocytosis. *Nat. Cell Biol.* **13**, 1124-1131. doi:10.1038/ncb2307

Boyer, C., Schikorski, T. and Stevens, C. F. (1998). Comparison of hippocampal dendritic spines in culture and in brain. *J. Neurosci.* **18**, 5294-5300. doi:10.1523/JNEUROSCI.18-14-05294.1998

Brunk, U. T. and Terman, A. (2002). Lipofuscin: mechanisms of age-related accumulation and influence on cell function. *Free Radic. Biol. Med.* **33**, 611-619. doi:10.1016/S0891-5849(02)00959-0

Buggia-Prévot, V., Fernandez, C. G., Udayar, V., Vetrivel, K. S., Elie, A., Roseman, J., Sasse, V. A., Lefkow, M., Meckler, X., Bhattacharyya, S. et al. (2013). A function for EHD family proteins in unidirectional retrograde dendritic transport of BACE1 and Alzheimer's disease Aβ production. *Cell Rep.* **5**, 1552-1563. doi:10.1016/j.celrep.2013.12.006

Carey, R. M., Balcz, B. A., Lopez-Coviella, I. and Slack, B. E. (2005). Inhibition of dynamin-dependent endocytosis increases shedding of the amyloid precursor protein ectodomain and reduces generation of amyloid beta protein. *BMC Cell Biol.* **6**, 30. doi:10.1186/1471-2121-6-30

Carmona, S., Hardy, J. and Guerreiro, R. (2018). The genetic landscape of Alzheimer disease. *Handb Clin Neurol* **148**, 395-408. doi:10.1016/B978-0-444-64076-5.00026-0

Castellano, J. M., Kim, J., Stewart, F. R., Jiang, H., DeMattos, R. B., Patterson, B. W., Fagan, A. M., Morris, J. C., Mawuenyega, K. G., Cruchaga, C. et al. (2011). Human apoE isoforms differentially regulate brain amyloid-β peptide clearance. *Sci. Transl. Med.* **3**, 89ra57. doi:10.1126/scitranslmed.3002156

Cataldo, A. M., Peterhoff, C. M., Troncoso, J. C., Gomez-Isla, T., Hyman, B. T. and Nixon, R. A. (2000). Endocytic pathway abnormalities precede amyloid β deposition in sporadic Alzheimer's disease and Down syndrome: differential effects of APOE genotype and presenilin mutations. *Am. J. Pathol.* **157**, 277-286. doi:10.1016/S0002-9440(10)64538-5

Chaufty, J., Sullivan, S. E. and Ho, A. (2012). Intracellular amyloid precursor protein sorting and amyloid-β secretion are regulated by Src-mediated phosphorylation of Mint2. *J. Neurosci.* **32**, 9613-9625. doi:10.1523/JNEUROSCI.0602-12.2012

Chia, P. Z. C., Toh, W. H., Sharples, R., Gasnereau, I., Hill, A. F. and Gleeson, P. A. (2013). Intracellular itinerary of internalised β-secretase, BACE1, and its

potential impact on β-amyloid peptide biogenesis. *Traffic* **14**, 997-1013. doi:10.1111/tra.12088

Cirrito, J. R., Kang, J.-E., Lee, J., Stewart, F. R., Verges, D. K., Silverio, L. M., Bu, G., Mennerick, S. and Holtzman, D. M. (2008). Endocytosis is required for synaptic activity-dependent release of amyloid-beta in vivo. *Neuron* **58**, 42-51. doi:10.1016/j.neuron.2008.02.003

Cole, S. L. and Vassar, R. (2007). The basic biology of BACE1: A key therapeutic target for alzheimer's disease. *Curr. Genomics* **8**, 509-530. doi:10.2174/138920207783769512

Cossec, J.-C., Simon, A., Marquer, C., Moldrich, R. X., Leterrier, C., Rossier, J., Duyckaerts, C., Lenkei, Z. and Potier, M.-C. (2010). Clathrin-dependent APP endocytosis and Abeta secretion are highly sensitive to the level of plasma membrane cholesterol. *Biochim. Biophys. Acta* **1801**, 846-852. doi:10.1016/j.bbalip.2010.05.010

Daniel, J. A., Chau, N., Abdel-Hamid, M. K., Hu, L., von Kleist, L., Whiting, A., Krishnan, S., Maamary, P., Joseph, S. R., Simpson, F. et al. (2015). Phenothiazine-derived antipsychotic drugs inhibit dynamin and clathrin-mediated endocytosis. *Traffic* **16**, 635-654. doi:10.1111/tra.12272

Das, U., Wang, L., Ganguly, A., Saikia, J. M., Wagner, S. L., Koo, E. H. and Roy, S. (2016). Visualizing APP and BACE-1 approximation in neurons yields insight into the amyloidogenic pathway. *Nat. Neurosci.* **19**, 55-64. doi:10.1038/nn.4188

Davis, C. G., van Driel, I. R., Russell, D. W., Brown, M. S. and Goldstein, J. L. (1987). The low density lipoprotein receptor. Identification of amino acids in cytoplasmic domain required for rapid endocytosis. *J. Biol. Chem.* **262**, 4075-4082. doi:10.1016/S0021-9258(18)61313-4

de Chaumont, F., Dallongeville, S., Chenouard, N., Hervé, N., Pop, S., Provoost, T., Meas-Yedid, V., Pankajakshan, P., Lecomte, T., Le Montagner, Y. et al. (2012). Icy: an open bioimage informatics platform for extended reproducible research. *Nat. Methods* **9**, 690-696. doi:10.1038/nmeth.2075

Dickstein, D. L., Weaver, C. M., Luebke, J. I. and Hof, P. R. (2013). Dendritic spine changes associated with normal aging. *Neuroscience* **251**, 21-32. doi:10.1016/j.neuroscience.2012.09.077

Dong, C. M., Wang, X. L., Wang, G. M., Zhang, W. J., Zhu, L., Gao, S., Yang, D. J., Qin, Y., Liang, Q. J., Chen, Y. L. et al. (2014). A stress-induced cellular aging model with postnatal neural stem cells. *Cell Death Dis.* **5**, e1116. doi:10.1038/cddis.2014.82

Dutta, D., Williamson, C. D., Cole, N. B. and Donaldson, J. G. (2012). Pitstop 2 is a potent inhibitor of clathrin-independent endocytosis. *PLoS ONE* **7**, e45799. doi:10.1371/journal.pone.0045799

Edgar, J. R., Willén, K., Gouras, G. K. and Futter, C. E. (2015). ESCRTs regulate amyloid precursor protein sorting in multivesicular bodies and intracellular amyloid-β accumulation. *J. Cell Sci.* **128**, 2520-2528. doi:10.1242/jcs.170233

Ehrlich, M., Boll, W., Van Oijen, A., Hariharan, R., Chandran, K., Nibert, M. L. and Kirchhausen, T. (2004). Endocytosis by random initiation and stabilization of clathrin-coated pits. *Cell* **118**, 591-605. doi:10.1016/j.cell.2004.08.017

Eimer, W. A. and Vassar, R. (2013). Neuron loss in the 5XFAD mouse model of Alzheimer's disease correlates with intraneuronal Aβ42 accumulation and Caspase-3 activation. *Mol. Neurodegener.* **8**, 2. doi:10.1186/1750-1326-8-2

Ferguson, S. M. (2018). Axonal transport and maturation of lysosomes. *Curr. Opin. Neurobiol.* **51**, 45-51. doi:10.1016/j.conb.2018.02.020

Flood, F. M., Cowburn, R. F. and Johnston, J. A. (1997). Presenilin-1, amyloid precursor protein and amyloid precursor-like protein 2 mRNA levels in human superior frontal cortex during aging. *Neurosci. Lett.* **235**, 17-20. doi:10.1016/S0304-3940(97)00697-6

Fomina, A. F., Deerinck, T. J., Ellisman, M. H. and Cahalan, M. D. (2003). Regulation of membrane trafficking and subcellular organization of endocytic compartments revealed with FM1-43 in resting and activated human T cells. *Exp. Cell Res.* **291**, 150-166. doi:10.1016/S0014-4827(03)00372-0

Francis, F., Koulakoff, A., Boucher, D., Chafey, P., Schaar, B., Vinet, M. C., Friocourt, G., McDonnell, N., Reiner, O., Kahn, A. et al. (1999). Doublecortin is a developmentally regulated, microtubule-associated protein expressed in migrating and differentiating neurons. *Neuron* **23**, 247-256. doi:10.1016/S0896-6273(00)80777-1

Fukumoto, H., Rosene, D. L., Moss, M. B., Raju, S., Hyman, B. T. and Irizarry, M. C. (2004). Beta-secretase activity increases with aging in human, monkey, and mouse brain. *Am. J. Pathol.* **164**, 719-725. doi:10.1016/S0002-9440(10)63159-8

Funato, H., Yoshimura, M., Kusui, K., Tamaoka, A., Ishikawa, K., Ohkoshi, N., Namekata, K., Okeda, R. and Ihara, Y. (1998). Quantitation of amyloid beta-protein (A beta) in the cortex during aging and in Alzheimer's disease. *Am. J. Pathol.* **152**, 1633-1640.

Furusawa, K., Takasugi, T., Chiu, Y.-W., Hori, Y., Tomita, T., Fukuda, M. and Hisanaga, S.-I. (2019). CD2-associated protein (CD2AP) overexpression accelerates amyloid precursor protein (APP) transfer from early endosomes to the lysosomal degradation pathway. *J. Biol. Chem.* **294**, 10886-10899. doi:10.1074/jbc.RA118.005385

Gauthier, S., Reisberg, B., Zaudig, M., Petersen, R. C., Ritchie, K., Broich, K., Belleville, S., Brodaty, H., Bennett, D., Chertkow, H. et al. (2006). Mild cognitive impairment. *Lancet* **367**, 1262-1270. doi:10.1016/S0140-6736(06)68542-5

Gegelashvili, G., Schousboe, A. and Linnemann, D. (1994). Expression of amyloid precursor protein (APP) in rat brain and cultured neural cells. *Int. J. Dev. Neurosci.* **12**, 703-708. doi:10.1016/0736-5748(94)90050-7

Ginsberg, S. D., Mufson, E. J., Alldred, M. J., Counts, S. E., Wuu, J., Nixon, R. A. and Che, S. (2011). Upregulation of select rab GTPases in cholinergic basal forebrain neurons in mild cognitive impairment and Alzheimer's disease. *J. Chem. Neuroanat.* **42**, 102-110. doi:10.1016/j.jchemneu.2011.05.012

Gordon, B. A., Blazey, T. M., Su, Y., Hari-Raj, A., Dincer, A., Flores, S., Christensen, J., McDade, E., Wang, G., Xiong, C. et al. (2018). Spatial patterns of neuroimaging biomarker change in individuals from families with autosomal dominant Alzheimer's disease: a longitudinal study. *Lancet Neurol.* **17**, 241-250. doi:10.1016/S1474-4422(18)30028-0

Goslin, K. and Banker, G. (1989). Experimental observations on the development of polarity by hippocampal neurons in culture. *J. Cell Biol.* **108**, 1507-1516. doi:10.1083/jcb.108.4.1507

Gouras, G. K., Almeida, C. G. and Takahashi, R. H. (2005). Intraneuronal Abeta accumulation and origin of plaques in Alzheimer's disease. *Neurobiol. Aging* **26**, 1235-1244. doi:10.1016/j.neurobiolaging.2005.05.022

Gray, D. A. and Woulfe, J. (2005). Lipofuscin and aging: a matter of toxic waste. *Sci. Aging Knowledge Environ.* **2005**, re1.

Grbovic, O. M., Mathews, P. M., Jiang, Y., Schmidt, S. D., Dinakar, R., Summers-Terio, N. B., Ceresa, B. P., Nixon, R. A. and Cataldo, A. M. (2003). Rab5-stimulated up-regulation of the endocytic pathway increases intracellular beta-cleaved amyloid precursor protein carboxyl-terminal fragment levels and Abeta production. *J. Biol. Chem.* **278**, 31261-31268. doi:10.1074/jbc.M304122200

Guimas Almeida, C., Sadat Mirfakhar, F., Perdigão, C. and Burrinha, T. (2018). Impact of late-onset Alzheimer's genetic risk factors on beta-amyloid endocytic production. *Cell Mol. Life Sci.* **75**, 2577-2589. doi:10.1007/s00018-018-2825-9

Guix, F. X., Wahle, T., Vennekens, K., Snellinx, A., Chávez-Gutiérrez, L., Ill-Raga, G., Ramos-Fernandez, E., Guardia-Laguarta, C., Lleó, A., Arimon, M. et al. (2012). Modification of γ-secretase by nitrosative stress links neuronal ageing to sporadic Alzheimer's disease. *EMBO Mol. Med.* **4**, 660-673. doi:10.1002/emmm.201200243

Guntupalli, S., Widagdo, J. and Anggono, V. (2016). Amyloid-β-induced dysregulation of AMPA receptor trafficking. *Neural Plast.* **2016**, 3204519. doi:10.1155/2016/3204519

Haass, C., Schlossmacher, M. G., Hung, A. Y., Vigo-Pelfrey, C., Mellon, A., Ostaszewski, B. L., Lieberburg, I., Koo, E. H., Schenk, D. and Teplow, D. B. (1992). Amyloid beta-peptide is produced by cultured cells during normal metabolism. *Nature* **359**, 322-325. doi:10.1038/359322a0

Harold, D., Abraham, R., Hollingworth, P., Sims, R., Gerrish, A., Hamshere, M. L., Pahwa, J. S., Moskvina, V., Dowzell, K., Williams, A. et al. (2009). Genome-wide association study identifies variants at CLU and PICALM associated with Alzheimer's disease. *Nat. Genet.* **41**, 1088-1093. doi:10.1038/ng.440

Herskowitz, J. H., Offe, K., Deshpande, A., Kahn, R. A., Levey, A. I. and Lah, J. J. (2012). GGA1-mediated endocytic traffic of LR11/SorLA alters APP intracellular distribution and amyloid-β production. *Mol. Biol. Cell* **23**, 2645-2657. doi:10.1091/mbc.e12-01-0014

Hetrick, B., Han, M. S., Helgeson, L. A. and Nolen, B. J. (2013). Small molecules CK-666 and CK-869 inhibit actin-related protein 2/3 complex by blocking an activating conformational change. *Chem. Biol.* **20**, 701-712. doi:10.1016/j.chembiol.2013.03.019

Hinze, C. and Boucrot, E. (2018). Local actin polymerization during endocytic carrier formation. *Biochem. Soc. Trans.* **46**, 565-576. doi:10.1042/BST20170355

Hollingworth, P., Harold, D., Sims, R., Gerrish, A., Lambert, J.-C., Carrasquillo, M. M., Abraham, R., Hamshere, M. L., Pahwa, J. S., Moskvina, V. et al. (2011). Common variants at ABCA7, MS4A6A/MS4A4E, EPHA1, CD33 and CD2AP are associated with Alzheimer's disease. *Nat. Genet.* **43**, 429-435. doi:10.1038/ng.803

Hung, A. Y., Koo, E. H., Haass, C. and Selkoe, D. J. (1992). Increased expression of beta-amyloid precursor protein during neuronal differentiation is not accompanied by secretory cleavage. *Proc. Natl. Acad. Sci. USA* **89**, 9439-9443. doi:10.1073/pnas.89.20.9439

Ikonomovic, M. D., Nocera, R., Mizukami, K. and Armstrong, D. M. (2000). Age-related loss of the AMPA receptor subunits GluR2/3 in the human nucleus basalis of Meynert. *Exp. Neurol.* **166**, 363-375. doi:10.1006/exnr.2000.7544

Isogai, T., van der Kammen, R. and Innocenti, M. (2015). SMIFH2 has effects on Formins and p53 that perturb the cell cytoskeleton. *Sci. Rep.* **5**, 9802. doi:10.1038/srep09802

Ivanov, A. I. (2008). Pharmacological inhibition of endocytic pathways: is it specific enough to be useful? *Methods Mol. Biol.* **440**, 15-33. doi:10.1007/978-1-59745-178-9_2

Iwata, N., Takaki, Y., Fukami, S., Tsubuki, S. and Saido, T. C. (2002). Region-specific reduction of A beta-degrading endopeptidase, neprilysin, in mouse hippocampus upon aging. *J. Neurosci. Res.* **70**, 493-500. doi:10.1002/jnr.10390

Jung, S. S., Nalbantoglu, J. and Cashman, N. R. (1996). Alzheimer's beta-amyloid precursor protein is expressed on the surface of immediately *ex vivo* brain cells: a flow cytometric study. *J. Neurosci. Res.* **46**, 336-348. doi:10.1002/(SICI)1097-4547(19961101)46:3<336::AID-JNR7>3.0.CO;2-L

Jurk, D., Wang, C., Miwa, S., Maddick, M., Korolchuk, V., Tsolou, A., Gonos, E. S., Thrasivoulou, C., Saffrey, M. J., Cameron, K. et al. (2012). Postmitotic neurons develop a p21-dependent senescence-like phenotype driven by a DNA damage response. *Aging Cell* **11**, 996-1004. doi:10.1111/j.1474-9726.2012.00870.x

Kaksonen, M. and Roux, A. (2018). Mechanisms of clathrin-mediated endocytosis. *Nat. Rev. Mol. Cell Biol.* **19**, 313-326. doi:10.1038/nrm.2017.132

Kanatsu, K. and Tomita, T. (2017). Molecular mechanisms of the genetic risk factors in pathogenesis of Alzheimer disease. *Front. Biosci. (Landmark Ed)* **22**, 180-192. doi:10.2741/4480

Kanatsu, K., Morohashi, Y., Suzuki, M., Kuroda, H., Watanabe, T., Tomita, T. and Iwatsubo, T. (2014). Decreased CALM expression reduces Aβ42 to total Aβ ratio through clathrin-mediated endocytosis of γ-secretase. *Nat. Commun.* **5**, 3386. doi:10.1038/ncomms4386

Kern, A., Roempp, B., Prager, K., Walter, J. and Behl, C. (2006). Down-regulation of endogenous amyloid precursor protein processing due to cellular aging. *J. Biol. Chem.* **281**, 2405-2413. doi:10.1074/jbc.M505625200

Kikuchi, M., Hirosawa, T., Yokokura, M., Yagi, S., Mori, N., Yoshikawa, E., Yoshihara, Y., Sugihara, G., Takebayashi, K., Iwata, Y. et al. (2011). Effects of brain amyloid deposition and reduced glucose metabolism on the default mode of brain function in normal aging. *J. Neurosci.* **31**, 11193-11199. doi:10.1523/JNEUROSCI.2535-11.2011

Kimura, N., Yanagisawa, K., Terao, K., Ono, F., Sakakibara, I., Ishii, Y., Kyuwa, S. and Yoshikawa, Y. (2005). Age-related changes of intracellular Abeta in cynomolgus monkey brains. *Neuropathol. Appl. Neurobiol.* **31**, 170-180. doi:10.1111/j.1365-2990.2004.00624.x

Kimura, N., Imamura, O., Ono, F. and Terao, K. (2007). Aging attenuates dynactin-dynein interaction: down-regulation of dynein causes accumulation of endogenous tau and amyloid precursor protein in human neuroblastoma cells. *J. Neurosci. Res.* **85**, 2909-2916. doi:10.1002/jnr.21408

Kimura, N., Okabayashi, S. and Ono, F. (2012). Dynein dysfunction disrupts intracellular vesicle trafficking bidirectionally and perturbs synaptic vesicle docking via endocytic disturbances a potential mechanism underlying age-dependent impairment of cognitive function. *Am. J. Pathol.* **180**, 550-561. doi:10.1016/j.ajpath.2011.10.037

Kimura, N., Samura, E., Suzuki, K., Okabayashi, S., Shimozawa, N. and Yasutomi, Y. (2016). Dynein dysfunction reproduces age-dependent retromer deficiency: concomitant disruption of retrograde trafficking is required for alteration in β-amyloid precursor protein metabolism. *Am. J. Pathol.* **186**, 1952-1966. doi:10.1016/j.ajpath.2016.03.006

Kobayashi, S., Sawano, A., Nojima, Y., Shibuya, M. and Maru, Y. (2004). The c-Cbl/CD2AP complex regulates VEGF-induced endocytosis and degradation of Flt-1 (VEGFR-1). *FASEB J.* **18**, 929-931. doi:10.1096/fj.03-0767fje

Koo, E. H. and Squazzo, S. L. (1994). Evidence that production and release of amyloid beta-protein involves the endocytic pathway. *J. Biol. Chem.* **269**, 17386-17389. doi:10.1016/S0021-9258(17)32449-3

Kuboyama, T., Lee, Y.-A., Nishiko, H. and Tohda, C. (2015). Inhibition of clathrin-mediated endocytosis prevents amyloid β-induced axonal damage. *Neurobiol. Aging* **36**, 1808-1819. doi:10.1016/j.neurobiolaging.2015.02.005

Kunkle, B. W., Grenier-Boley, B., Sims, R., Bis, J. C., Damotte, V., Naj, A. C., Boland, A., Vronskaya, M., van der Lee, S. J., Amlie-Wolf, A. et al. (2019). Genetic meta-analysis of diagnosed Alzheimer's disease identifies new risk loci and implicates Aβ, tau, immunity and lipid processing. *Nat. Genet.* **51**, 414-430. doi:10.1038/s41588-019-0358-2

LaFerla, F. M., Green, K. N. and Oddo, S. (2007). Intracellular amyloid-beta in Alzheimer's disease. *Nat. Rev. Neurosci.* **8**, 499-509. doi:10.1038/nrn2168

Lagache, T., Grassart, A., Dallongeville, S., Faklaris, O., Sauvonnet, N., Dufour, A., Danglot, L. and Olivo-Marin, J.-C. (2018). Mapping molecular assemblies with fluorescence microscopy and object-based spatial statistics. *Nat. Commun.* **9**, 698. doi:10.1038/s41467-018-03053-x

Lai, A. Y. and McLaurin, J. (2010). Mechanisms of amyloid-Beta Peptide uptake by neurons: the role of lipid rafts and lipid raft-associated proteins. *Int. J. Alzheimers. Dis.* **2011**, 548380. doi:10.4061/2011/548380

Lehtonen, S., Zhao, F. and Lehtonen, E. (2002). CD2-associated protein directly interacts with the actin cytoskeleton. *Am. J. Physiol. Renal Physiol.* **283**, F734-F743. doi:10.1152/ajprenal.00312.2001

Lesné, S. E., Sherman, M. A., Grant, M., Kuskowski, M., Schneider, J. A., Bennett, D. A. and Ashe, K. H. (2013). Brain amyloid-β oligomers in ageing and Alzheimer's disease. *Brain* **136**, 1383-1398. doi:10.1093/brain/awt062

Lu, L.-N., Qian, Z.-M., Wu, K.-C., Yung, W.-H. and Ke, Y. (2017). Expression of iron transporters and pathological hallmarks of parkinson's and alzheimer's diseases in the brain of young, adult, and aged rats. *Mol. Neurobiol.* **54**, 5213-5224. doi:10.1007/s12035-016-0067-0

Lynch, D. K., Winata, S. C., Lyons, R. J., Hughes, W. E., Lehrbach, G. M., Wasinger, V., Corthals, G., Cordwell, S. and Daly, R. J. (2003). A Cortactin-CD2-associated protein (CD2AP) complex provides a novel link between epidermal growth factor receptor endocytosis and the actin cytoskeleton. *J. Biol. Chem.* **278**, 21805-21813. doi:10.1074/jbc.M211407200

Macia, E., Ehrlich, M., Massol, R., Boucrot, E., Brunner, C. and Kirchhausen, T. (2006). Dynasore, a cell-permeable inhibitor of dynamin. *Dev. Cell* **10**, 839-850. doi:10.1016/j.devcel.2006.04.002

Malorni, W., Testa, U., Rainaldi, G., Tritarelli, E. and Peschle, C. (1998). Oxidative stress leads to a rapid alteration of transferrin receptor intravesicular trafficking. *Exp. Cell Res.* **241**, 102-116. doi:10.1006/excr.1998.4020

Marks, S. M., Lockhart, S. N., Baker, S. L. and Jagust, W. J. (2017). Tau and β-amyloid are associated with medial temporal lobe structure, function, and memory encoding in normal aging. *J. Neurosci.* **37**, 3192-3201. doi:10.1523/JNEUROSCI.3769-16.2017

Marquez-Sterling, N. R., Lo, A. C. Y., Sisodia, S. S. and Koo, E. H. (1997). Trafficking of cell-surface β-amyloid precursor protein: evidence that a sorting intermediate participates in synaptic vesicle recycling. *J. Neurosci.* **17**, 140-151. doi:10.1523/JNEUROSCI.17-01-00140.1997

Martin, M. G., Trovò, L., Perga, S., Sadowska, A., Rasola, A., Chiara, F. and Dotti, C. G. (2011). Cyp46-mediated cholesterol loss promotes survival in stressed hippocampal neurons. *Neurobiol. Aging* **32**, 933-943. doi:10.1016/j.neurobiolaging.2009.04.022

Mattson, M. P. and Magnus, T. (2006). Ageing and neuronal vulnerability. *Nat. Rev. Neurosci.* **7**, 278-294. doi:10.1038/nrn1886

Maxfield, F. R. and McGraw, T. E. (2004). Endocytic recycling. *Nat. Rev. Mol. Cell Biol.* **5**, 121-132. doi:10.1038/nrm1315

Mayor, S. and Pagano, R. E. (2007). Pathways of clathrin-independent endocytosis. *Nat. Rev. Mol. Cell Biol.* **8**, 603-612. doi:10.1038/nrm2216

McDade, E., Wang, G., Gordon, B. A., Hassenstab, J., Benzinger, T. L. S., Buckles, V., Fagan, A. M., Holtzman, D. M., Cairns, N. J., Goate, A. M. et al. (2018). Longitudinal cognitive and biomarker changes in dominantly inherited Alzheimer disease. *Neurology* **91**, e1295-e1306. doi:10.1212/WNL.0000000000006277

McMahon, H. T. and Boucrot, E. (2011). Molecular mechanism and physiological functions of clathrin-mediated endocytosis. *Nat. Rev. Mol. Cell Biol.* **12**, 517-533. doi:10.1038/nrm3151

Morel, E., Chamoun, Z., Lasiecka, Z. M., Chan, R. B., Williamson, R. L., Vetanovetz, C., Dall'Armi, C., Simoes, S., Point Du Jour, K. S., McCabe, B. D. et al. (2013). Phosphatidylinositol-3-phosphate regulates sorting and processing of amyloid precursor protein through the endosomal system. *Nat. Commun.* **4**, 2250. doi:10.1038/ncomms3250

Morrison, J. H. and Baxter, M. G. (2012). The ageing cortical synapse: hallmarks and implications for cognitive decline. *Nat. Rev. Neurosci.* **13**, 240-250. doi:10.1038/nrn3200

Naj, A. C., Jun, G., Beecham, G. W., Wang, L.-S., Vardarajan, B. N., Buros, J., Gallins, P. J., Buxbaum, J. D., Jarvik, G. P., Crane, P. K. et al. (2011). Common variants at MS4A4/MS4A6E, CD2AP, CD33 and EPHA1 are associated with late-onset Alzheimer's disease. *Nat. Genet.* **43**, 436-441. doi:10.1038/ng.801

Neefjes, J. and van der Kant, R. (2014). Stuck in traffic: an emerging theme in diseases of the nervous system. *Trends Neurosci.* **37**, 66-76. doi:10.1016/j.tins.2013.11.006

Nicolas, M. and Hassan, B. A. (2014). Amyloid precursor protein and neural development. *Development* **141**, 2543-2548. doi:10.1242/dev.108712

Norvin, D., Kim, G., Baker-Nigh, A. and Geula, C. (2015). Accumulation and age-related elevation of amyloid-β within basal forebrain cholinergic neurons in the rhesus monkey. *Neuroscience* **298**, 102-111. doi:10.1016/j.neuroscience.2015.04.011

Nwabuisi-Heath, E., LaDu, M. J. and Yu, C. (2012). Simultaneous analysis of dendritic spine density, morphology and excitatory glutamate receptors during neuron maturation in vitro by quantitative immunocytochemistry. *J. Neurosci. Methods* **207**, 137-147. doi:10.1016/j.jneumeth.2012.04.003

Palop, J. J. and Mucke, L. (2010). Amyloid-beta-induced neuronal dysfunction in Alzheimer's disease: from synapses toward neural networks. *Nat. Neurosci.* **13**, 812-818. doi:10.1038/nn.2583

Papa, M., Bundman, M. C., Greenberger, V. and Segal, M. (1995). Morphological analysis of dendritic spine development in primary cultures of hippocampal neurons. *J. Neurosci.* **15**, 1-11. doi:10.1523/JNEUROSCI.15-01-00001.1995

Pegasiou, C. M., Zolnourian, A., Gomez-Nicola, D., Deinhardt, K., Nicoll, J., Ahmed, A., Vajramani, G., Grundy, P., Verhoog, M., Mansvelder, H. et al. (2020). Age-Dependent Changes in Synaptic NMDA Receptor Composition in Adult Human Cortical Neurons. *Cereb. Cortex* **30**, 4246-4256. doi:10.1093/cercor/bhaa052

Pensalfini, A., Albay, R., Rasool, S., Wu, J. W., Hatami, A., Arai, H., Margol, L., Milton, S., Poon, W. W., Corrada, M. M. et al. (2014). Intracellular amyloid and the neuronal origin of Alzheimer neuritic plaques. *Neurobiol. Dis.* **71**, 53-61. doi:10.1016/j.nbd.2014.07.011

Petersen, R. C., Wiste, H. J., Weigand, S. D., Rocca, W. A., Roberts, R. O., Mielke, M. M., Lowe, V. J., Knopman, D. S., Pankratz, V. S., Machulda, M. M. et al. (2016). Association of elevated amyloid levels with cognition and biomarkers in cognitively normal people from the community. *JAMA Neurol.* **73**, 85-92. doi:10.1001/jamaneurol.2015.3098

Petralia, R. S., Mattson, M. P. and Yao, P. J. (2014). Communication breakdown: the impact of ageing on synapse structure. *Ageing Res. Rev.* **14**, 31-42. doi:10.1016/j.arr.2014.01.003

Picco, A., Kukulski, W., Manenschijn, H. E., Specht, T., Briggs, J. A. G. and Kaksonen, M. (2018). The contributions of the actin machinery to endocytic membrane bending and vesicle formation. *Mol. Biol. Cell* **29**, 1346-1358. doi:10.1091/mbc.E17-11-0688

Placanica, L., Zhu, L. and Li, Y.-M. (2009). Gender- and age-dependent gamma-secretase activity in mouse brain and its implication in sporadic Alzheimer disease. *PLoS ONE* **4**, e5088. doi:10.1371/journal.pone.0005088

Rajendran, L. and Annaert, W. (2012). Membrane trafficking pathways in Alzheimer's disease. *Traffic* **13**, 759-770. doi:10.1111/j.1600-0854.2012.01332.x

Rajendran, L., Honsho, M., Zahn, T. R., Keller, P., Geiger, K. D., Verkade, P. and Simons, K. (2006). Alzheimer's disease beta-amyloid peptides are released in association with exosomes. *Proc. Natl. Acad. Sci. USA* **103**, 11172-11177. doi:10.1073/pnas.0603838103

Rajendran, L., Schneider, A., Schlechtingen, G., Weidlich, S., Ries, J., Braxmeier, T., Schwille, P., Schulz, J. B., Schroeder, C., Simons, M. et al. (2008). Efficient inhibition of the Alzheimer's disease beta-secretase by membrane targeting. *Science* **320**, 520-523. doi:10.1126/science.1156609

Roux, A., Uyhazi, K., Frost, A. and De Camilli, P. (2006). GTP-dependent twisting of dynamin implicates constriction and tension in membrane fission. *Nature* **441**, 528-531. doi:10.1038/nature04718

Samson, R. D. and Barnes, C. A. (2013). Impact of aging brain circuits on cognition. *Eur. J. Neurosci.* **37**, 1903-1915. doi:10.1111/ejn.12183

Sannerud, R., Esselens, C., Ejsmont, P., Mattera, R., Rochin, L., Tharkeshwar, A. K., De Baets, G., De Wever, V., Habets, R., Baert, V. et al. (2016). Restricted Location of PSEN2/γ-Secretase Determines Substrate Specificity and Generates an Intracellular Aβ Pool. *Cell* **166**, 193-208. doi:10.1016/j.cell.2016.05.020

Selkoe, D. J. and Hardy, J. (2016). The amyloid hypothesis of Alzheimer's disease at 25 years. *EMBO Mol. Med.* **8**, 595-608. doi:10.15252/emmm.201606210

Shibata, M., Yamada, S., Kumar, S. R., Calero, M., Bading, J., Frangione, B., Holtzman, D. M., Miller, C. A., Strickland, D. K., Ghiso, J. et al. (2000). Clearance of Alzheimer's amyloid-ss(1-40) peptide from brain by LDL receptor-related protein-1 at the blood-brain barrier. *J. Clin. Invest.* **106**, 1489-1499. doi:10.1172/JCI10498

Shpetner, H. S. and Vallee, R. B. (1992). Dynamin is a GTPase stimulated to high levels of activity by microtubules. *Nature* **355**, 733-735. doi:10.1038/355733a0

Siman, R. and Velji, J. (2003). Localization of presenilin-nicastrin complexes and gamma-secretase activity to the trans-Golgi network. *J. Neurochem.* **84**, 1143-1153. doi:10.1046/j.1471-4159.2003.01616.x

Sinha, M., Bir, A., Banerjee, A., Bhowmick, P. and Chakrabarti, S. (2016). Multiple mechanisms of age-dependent accumulation of amyloid beta protein in rat brain: Prevention by dietary supplementation with N-acetylcysteine, α-lipoic acid and α-tocopherol. *Neurochem. Int.* **95**, 92-99. doi:10.1016/j.neuint.2015.10.003

Skovronsky, D. M., Doms, R. W. and Lee, V. M. (1998). Detection of a novel intraneuronal pool of insoluble amyloid beta protein that accumulates with time in culture. *J. Cell Biol.* **141**, 1031-1039. doi:10.1083/jcb.141.4.1031

Snyder, E. M., Nong, Y., Almeida, C. G., Paul, S., Moran, T., Choi, E. Y., Nairn, A. C., Salter, M. W., Lombroso, P. J., Gouras, G. K. et al. (2005). Regulation of NMDA receptor trafficking by amyloid-beta. *Nat. Neurosci.* **8**, 1051-1058. doi:10.1038/nn1503

Soykan, T., Kaempf, N., Sakaba, T., Vollweiter, D., Goerdeler, F., Puchkov, D., Kononenko, N. L. and Haucke, V. (2017). Synaptic vesicle endocytosis occurs on multiple timescales and is mediated by formin-dependent actin assembly. *Neuron* **93**, 854-866.e4. doi:10.1016/j.neuron.2017.02.011

Storey, E., Beyreuther, K. and Masters, C. L. (1996). Alzheimer's disease amyloid precursor protein on the surface of cortical neurons in primary culture co-localizes with adhesion patch components. *Brain Res.* **735**, 217-231. doi:10.1016/0006-8993(96)00608-7

Sullivan, S. E., Dillon, G. M., Sullivan, J. M. and Ho, A. (2014). Mint proteins are required for synaptic activity-dependent amyloid precursor protein (APP) trafficking and amyloid β generation. *J. Biol. Chem.* **289**, 15374-15383. doi:10.1074/jbc.M113.541003

Sun, J., Carlson-Stevermer, J., Das, U., Shen, M., Delenclos, M., Snead, A. M., Koo, S. Y., Wang, L., Qiao, D., Loi, J. et al. (2019). CRISPR/Cas9 editing of APP C-terminus attenuates β-cleavage and promotes α-cleavage. *Nat. Commun.* **10**, 53. doi:10.1038/s41467-018-07971-8

Takahashi, R. H., Milner, T. A., Li, F., Nam, E. E., Edgar, M. A., Yamaguchi, H., Beal, M. F., Xu, H., Greengard, P. and Gouras, G. K. (2002). Intraneuronal Alzheimer abeta42 accumulates in multivesicular bodies and is associated with synaptic pathology. *Am. J. Pathol.* **161**, 1869-1879. doi:10.1016/S0002-9440(10)64463-X

Takahashi, R. H., Almeida, C. G., Kearney, P. F., Yu, F., Lin, M. T., Milner, T. A. and Gouras, G. K. (2004). Oligomerization of Alzheimer's beta-amyloid within processes and synapses of cultured neurons and brain. *J. Neurosci.* **24**, 3592-3599. doi:10.1523/JNEUROSCI.5167-03.2004

Tang, V. W. and Brieher, W. M. (2013). FSGS3/CD2AP is a barbed-end capping protein that stabilizes actin and strengthens adherens junctions. *J. Cell Biol.* **203**, 815-833. doi:10.1083/jcb.201304143

Toh, W. H., Tan, J. Z. A., Zulkefli, K. L., Houghton, F. J. and Gleeson, P. A. (2017). Amyloid precursor protein traffics from the Golgi directly to early endosomes in an Arl5b- and AP4-dependent pathway. *Traffic* **18**, 159-175. doi:10.1111/tra.12465

Trovò, L., Ahmed, T., Callaerts-Vegh, Z., Buzzi, A., Bagni, C., Chuah, M., Vandendriessche, T., D'Hooge, R., Balschun, D. and Dotti, C. G. (2013). Low hippocampal PI(4,5)P□ contributes to reduced cognition in old mice as a result of loss of MARCKS. *Nat. Neurosci.* **16**, 449-455. doi:10.1038/nn.3342

Tuma, P. L. and Collins, C. A. (1994). Activation of dynamin GTPase is a result of positive cooperativity. *J. Biol. Chem.* **269**, 30842-30847. doi:10.1016/S0021-9258(18)47358-9

Ubelmann, F., Burrinha, T., Salavessa, L., Gomes, R., Ferreira, C., Moreno, N. and Guimas Almeida, C. (2017a). Bin1 and CD2AP polarise the endocytic generation of beta-amyloid. *EMBO Rep.* **18**, 102-122. doi:10.15252/embr.201642738

Ubelmann, F., Burrinha, T. and Guimas Almeida, C. (2017b). A novel protocol to quantitatively measure the endocytic trafficking of amyloid precursor protein (APP) in polarized primary neurons with sub-cellular resolution. *Bio Protoc* **7**, e2629. doi:10.21769/BioProtoc.2629

Ullrich, O., Horiuchi, H., Bucci, C. and Zerial, M. (1994). Membrane association of Rab5 mediated by GDP-dissociation inhibitor and accompanied by GDP/GTP exchange. *Nature* **368**, 157-160. doi:10.1038/368157a0

Vassar, R., Kovacs, D. M., Yan, R. and Wong, P. C. (2009). The beta-secretase enzyme BACE in health and Alzheimer's disease: regulation, cell biology, function, and therapeutic potential. *J. Neurosci.* **29**, 12787-12794. doi:10.1523/JNEUROSCI.3657-09.2009

Veitch, D. P., Weiner, M. W., Aisen, P. S., Beckett, L. A., Cairns, N. J., Green, R. C., Harvey, D., Jack, C. R., Jagust, W., Morris, J. C. et al. (2018). Understanding disease progression and improving Alzheimer's disease clinical trials: recent highlights from the Alzheimer's disease neuroimaging initiative. *Alzheimers Dement* **15**, 106-152. doi:10.1016/j.jalz.2018.08.005

Vetrivel, K. S. and Thinakaran, G. (2006). Amyloidogenic processing of beta-amyloid precursor protein in intracellular compartments. *Neurology* **66**, S69-S73. doi:10.1212/01.wnl.0000192107.17175.39

Vlassenko, A. G., Mintun, M. A., Xiong, C., Sheline, Y. I., Goate, A. M., Benzinger, T. L. S. and Morris, J. C. (2011). Amyloid-beta plaque growth in cognitively normal adults: longitudinal [11C]Pittsburgh compound B data. *Ann. Neurol.* **70**, 857-861. doi:10.1002/ana.22608

Wang, L. H., Rothberg, K. G. and Anderson, R. G. (1993). Mis-assembly of clathrin lattices on endosomes reveals a regulatory switch for coated pit formation. *J. Cell Biol.* **123**, 1107-1117. doi:10.1083/jcb.123.5.1107

Welikovitch, L. A., Do Carmo, S., Maglóczky, Z., Szocsics, P., Lőke, J., Freund, T. and Cuello, A. C. (2018). Evidence of intraneuronal Aβ accumulation preceding tau pathology in the entorhinal cortex. *Acta Neuropathol.* **136**, 901-917. doi:10.1007/s00401-018-1922-z

Welsch, T., Endlich, N., Gökce, G., Doroshenko, E., Simpson, J. C., Kriz, W., Shaw, A. S. and Endlich, K. (2005). Association of CD2AP with dynamic actin on vesicles in podocytes. *Am. J. Physiol. Renal Physiol.* **289**, F1134-F1143. doi:10.1152/ajprenal.00178.2005

Willem, M., Tahirovic, S., Busche, M. A., Ovsepian, S. V., Chafai, M., Kootar, S., Hornburg, D., Evans, L. D. B., Moore, S., Daria, A. et al. (2015). η-Secretase processing of APP inhibits neuronal activity in the hippocampus. *Nature* **526**, 443-447. doi:10.1038/nature14864

Willén, K., Edgar, J. R., Hasegawa, T., Tanaka, N., Futter, C. E. and Gouras, G. K. (2017). Aβ accumulation causes MVB enlargement and is modelled by dominant negative VPS4A. *Mol. Neurodegener.* **12**, 61. doi:10.1186/s13024-017-0203-y

Willox, A. K., Sahraoui, Y. M. E. and Royle, S. J. (2014). Non-specificity of Pitstop 2 in clathrin-mediated endocytosis. *Biol. Open* **3**, 326-331. doi:10.1242/bio.20147955

Wolfe, M. S. (2019). Structure and Function of the γ-Secretase Complex. *Biochemistry* **58**, 2953-2966. doi:10.1021/acs.biochem.9b00401

Xiao, Q., Gil, S.-C., Yan, P., Wang, Y., Han, S., Gonzales, E., Perez, R., Cirrito, J. R. and Lee, J.-M. (2012). Role of phosphatidylinositol clathrin assembly lymphoid-myeloid leukemia (PICALM) in intracellular amyloid precursor protein (APP) processing and amyloid plaque pathogenesis. *J. Biol. Chem.* **287**, 21279-21289. doi:10.1074/jbc.M111.338376

Xu, H., Sweeney, D., Wang, R., Thinakaran, G., Lo, A. C., Sisodia, S. S., Greengard, P. and Gandy, S. (1997). Generation of Alzheimer beta-amyloid protein in the trans-Golgi network in the apparent absence of vesicle formation. *Proc. Natl. Acad. Sci. USA* **94**, 3748-3752. doi:10.1073/pnas.94.8.3748

Yamazaki, T., Selkoe, D. J. and Koo, E. H. (1995). Trafficking of cell surface beta-amyloid precursor protein: retrograde and transcytotic transport in cultured neurons. *J. Cell Biol.* **129**, 431-442. doi:10.1083/jcb.129.2.431

Yan, R. (2017). Physiological functions of the β-site amyloid precursor protein cleaving enzyme 1 and 2. *Front. Mol. Neurosci.* **10**, 97. doi:10.3389/fnmol.2017.00097

Yang, Y.-J., Chen, H.-B., Wei, B., Wang, W., Zhou, P.-L., Zhan, J.-Q., Hu, M.-R., Yan, K., Hu, B. and Yu, B. (2015). Cognitive decline is associated with reduced

surface GluR1 expression in the hippocampus of aged rats. *Neurosci. Lett.* **591**, 176-181. doi:10.1016/j.neulet.2015.02.030

Yankner, B. A., Lu, T. and Loerch, P. (2008). The aging brain. *Annu. Rev. Pathol.* **3**, 41-66. doi:10.1146/annurev.pathmechdis.2.010506.092044

Youmans, K. L., Tai, L. M., Kanekiyo, T., Stine, W. B., Michon, S.-C., Nwabuisi-Heath, E., Manelli, A. M., Fu, Y., Riordan, S., Eimer, W. A. et al. (2012). Intraneuronal Aβ detection in 5xFAD mice by a new Aβ-specific antibody. *Mol. Neurodegener.* **7**, 8. doi:10.1186/1750-1326-7-8

Yuyama, K. and Yanagisawa, K. (2009). Late endocytic dysfunction as a putative cause of amyloid fibril formation in Alzheimer's disease. *J. Neurochem.* **109**, 1250-1260. doi:10.1111/j.1471-4159.2009.06046.x

Zou, L., Wang, Z., Shen, L., Bao, G. B., Wang, T., Kang, J. H. and Pei, G. (2007). Receptor tyrosine kinases positively regulate BACE activity and Amyloid-beta production through enhancing BACE internalization. *Cell Res.* **17**, 389-401. doi:10.1038/cr.2007.5

Figure S1

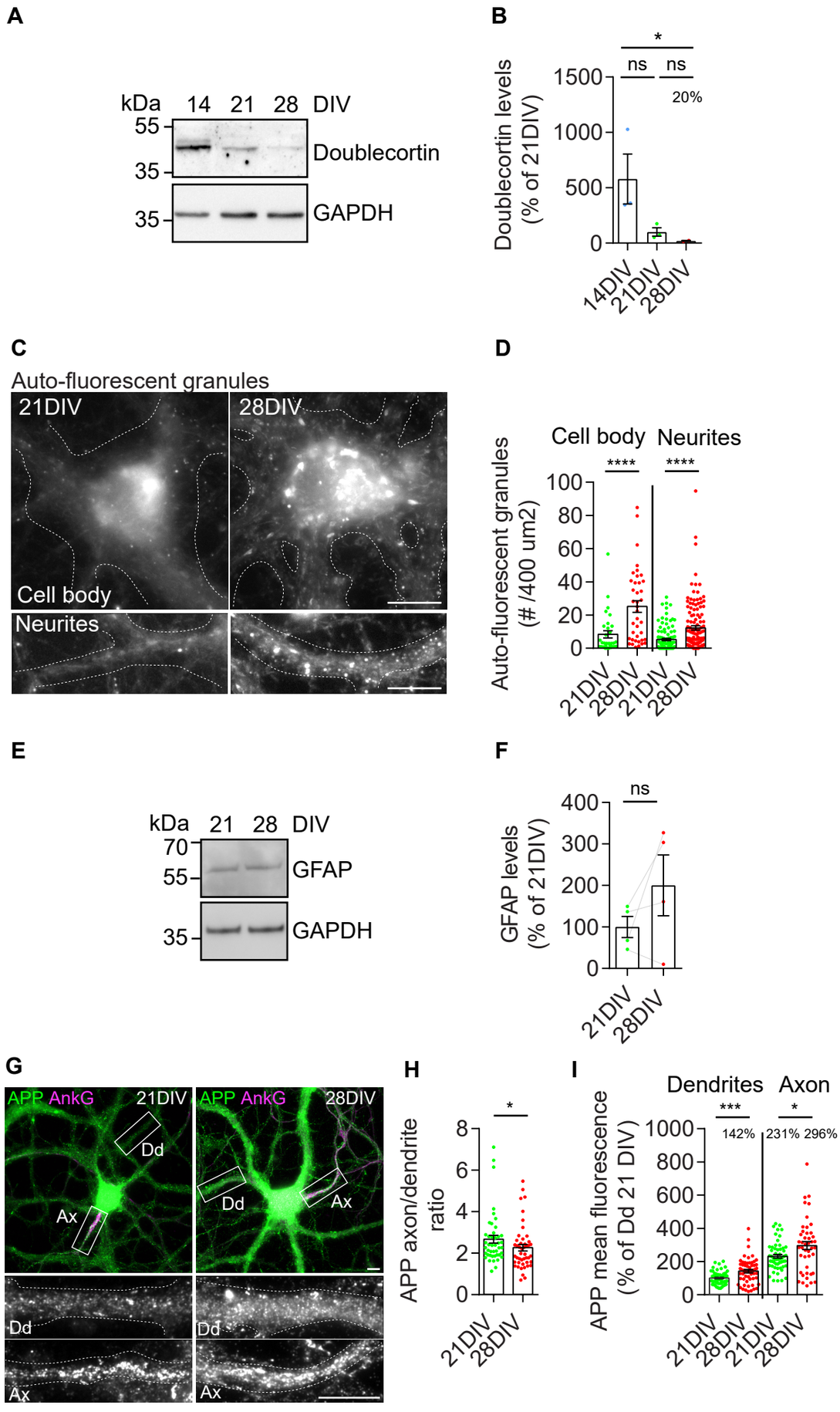

Figure S1. Aged neurons evidence canonical signs of aging and altered APP polarization.

A. Endogenous doublecortin in neurons at 14 DIV, 21 DIV and 28 DIV analyzed by western blot with anti-doublecortin antibody and GAPDH as loading control. **B.** Quantification of doublecortin levels normalized to percentage of 21 DIV neurons (n = 2-3; ^{ns}P = 0.4008 21 DIV vs. 14 DIV; ^{ns}P = 0.7907 28 DIV vs. 21DIV; *P =0.0417 28 DIV vs. 14DIV, one-way ANOVA on ranks with *post hoc* Dunn's testing, mean ± SEM). **C.** Auto-fluorescent aging granules, or lipofuscin, in the cell body and neurites of 21DIV and 28DIV neurons analyzed by epifluorescence microscopy. Scale bars, 10 µm. **D.** Quantification of the number of auto-fluorescent granules per area (400 µm2) in cell body and neurites (n=3-4, $N_{cellbody}$ = 31-39, $N_{neurites}$= 60-129, ****$P_{cellbody}$ < 0.0001 28 DIV vs. 21 DIV, ****$P_{neurites}$ < 0.0001 28 DIV vs. 21 DIV, Mann-Whitney test, mean ± SEM). **E.** Endogenous glial fibrillary acidic protein (GFAP) analyzed by western blot with anti-GFAP antibody and GAPDH as loading control of neurons at 21 DIV and 28 DIV. **F.** Quantification of GFAP levels normalized to percentage of 21 DIV neurons (n = 4; ^{ns}P = 0.2271 28 DIV vs. 21 DIV, paired t-test, mean ± SEM). **G.** APP (green) localization in axons and dendrites by immunofluorescence at 21 DIV and 28 DIV, with anti-APP antibody (Y188) and anti-ankyrin-G (AnkG; magenta) to identify axons, analyzed by epifluorescence microscopy. The white rectangles indicate APP (grey) localization in the magnified dendrites (Dd) and axons (Ax). Scale bar, 10 µm. **H.** Quantification of the APP axon/dendrite ratio indicating APP polarization (n=3, N_{21DIV} = 44, N_{28DIV} = 46; *P = 0.0322 28DIV vs 21DIV, Mann-Whitney test; mean ± SEM). **I.** Quantification of the APP mean intensity in dendrites and axons of 21DIV and 28 DIV neurons. Results were normalized to percentage of 21 DIV dendrites (n = 4-5, $N_{dendrites}$=57-76; N_{axon}= 44-55; ***$P_{dendrites}$ = 0.0002 28 DIV vs. 21 DIV dendrites, *P_{axon} = 0.0258 28 DIV vs. 21 DIV axons, Mann-Whitney test, mean ± SEM).

Figure S2

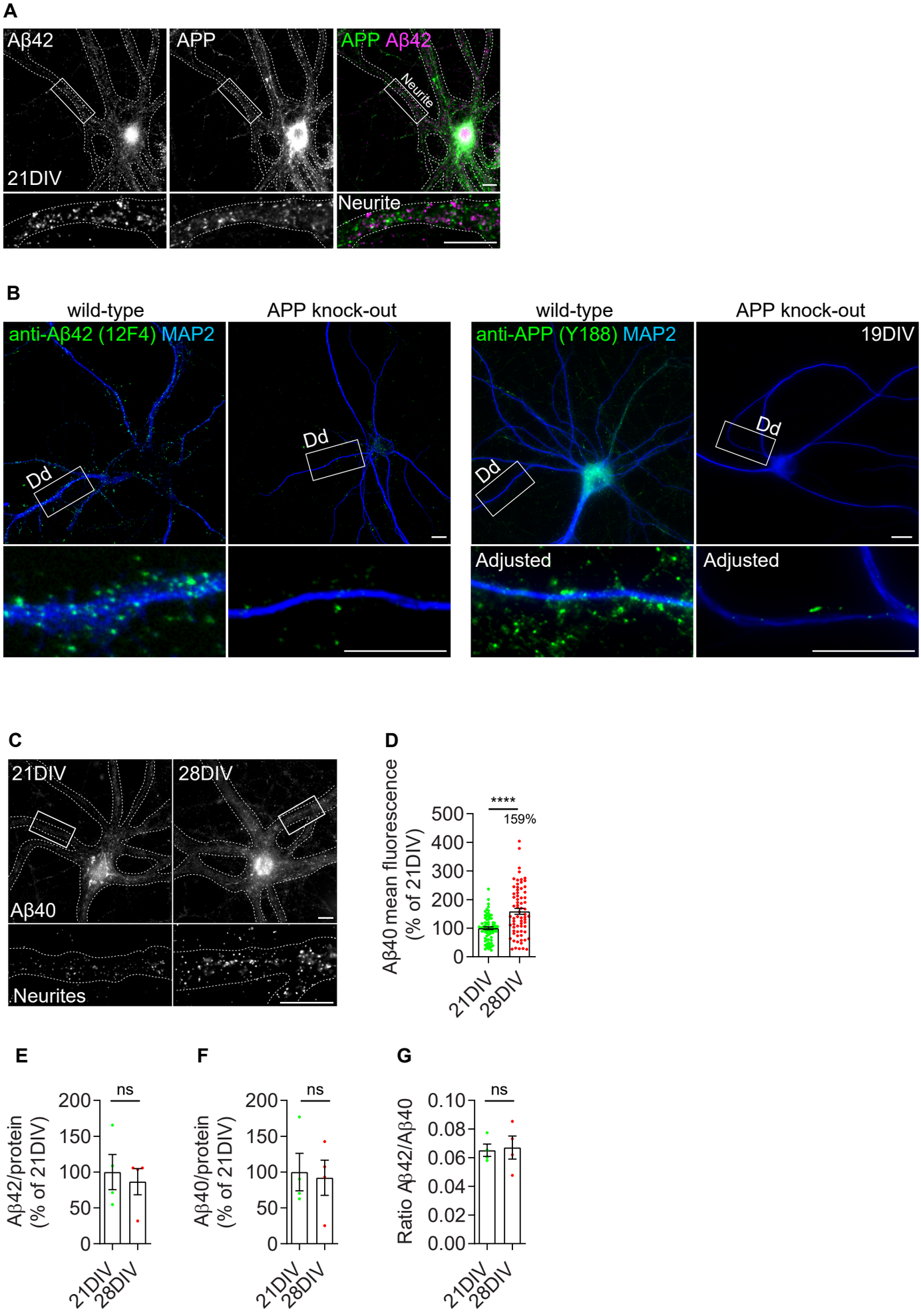

Figure S2. Aβ and APP antibody specificity in APP knock-out neurons, Aβ40 intracellular levels and secreted Aβ levels.

A. Aβ42 and APP co-staining with anti-Aβ42 antibody (12F4) and anti-APP antibody (Y188) in 21 DIV neurons as a control for specific intracellular Aβ42 detection. Aβ42 (grey, first panel), APP (grey, second panel), and merged (APP green; Aβ42 magenta). The white rectangles indicate the magnified regions shown below. Scale bar, 10 µm. **B.** Aβ42 and APP staining with anti-Aβ42 antibody (12F4) and anti-APP antibody (Y188) in 19 DIV wild-type and APP knock-out neurons as a control for specific intracellular Aβ42 (green, left panel) and APP (green, right panel) detection. MAP2 was used to label neuronal dendrites (blue). The white rectangles indicate the magnified regions shown below. Scale bar, 10 µm. **C.** Intracellular endogenous Aβ40 (grey) in neurons at 21 DIV and 28 DIV, immunolabelled with anti-Aβ40 antibody, analyzed by epifluorescence microscopy. The white rectangles indicate the magnified neurites. Scale bars, 10 µm. **D.** Quantification of Aβ40 mean intensity in neurites of 21DIV and 28DIV neurons, in percentage of 21 DIV (n = 3, $N_{neurites}$= 70-78, ****$P_{neurites}$ < 0.0001 28 DIV vs. 21 DIV neurons, unpaired t-test, mean ± SEM). **E.** Extracellular endogenous Aβ42 levels in conditioned media of neurons at 21 DIV and 28 DIV, measured by ELISA and normalized by total protein levels in the media (n = 4, ^{ns}P = 0.5459 28 DIV vs. 21 DIV media, paired t-test, mean ± SEM). **F.** Extracellular endogenous Aβ40 levels in the conditioned media of neurons at 21 DIV and 28 DIV, measured by ELISA and normalized by total protein levels in the media (n = 4, ^{ns}P = 0.6573 28 DIV vs. 21 DIV media, paired t-test, mean ± SEM). **G.** Aβ42/Aβ40 ratio in the conditioned media of neurons at 21 DIV and 28 DIV, measured by ELISA and normalized by total protein levels in the media (n = 4, ^{ns}P = 0.8656 28 DIV vs. 21 DIV media, paired t-test, mean ± SEM).

Figure S3

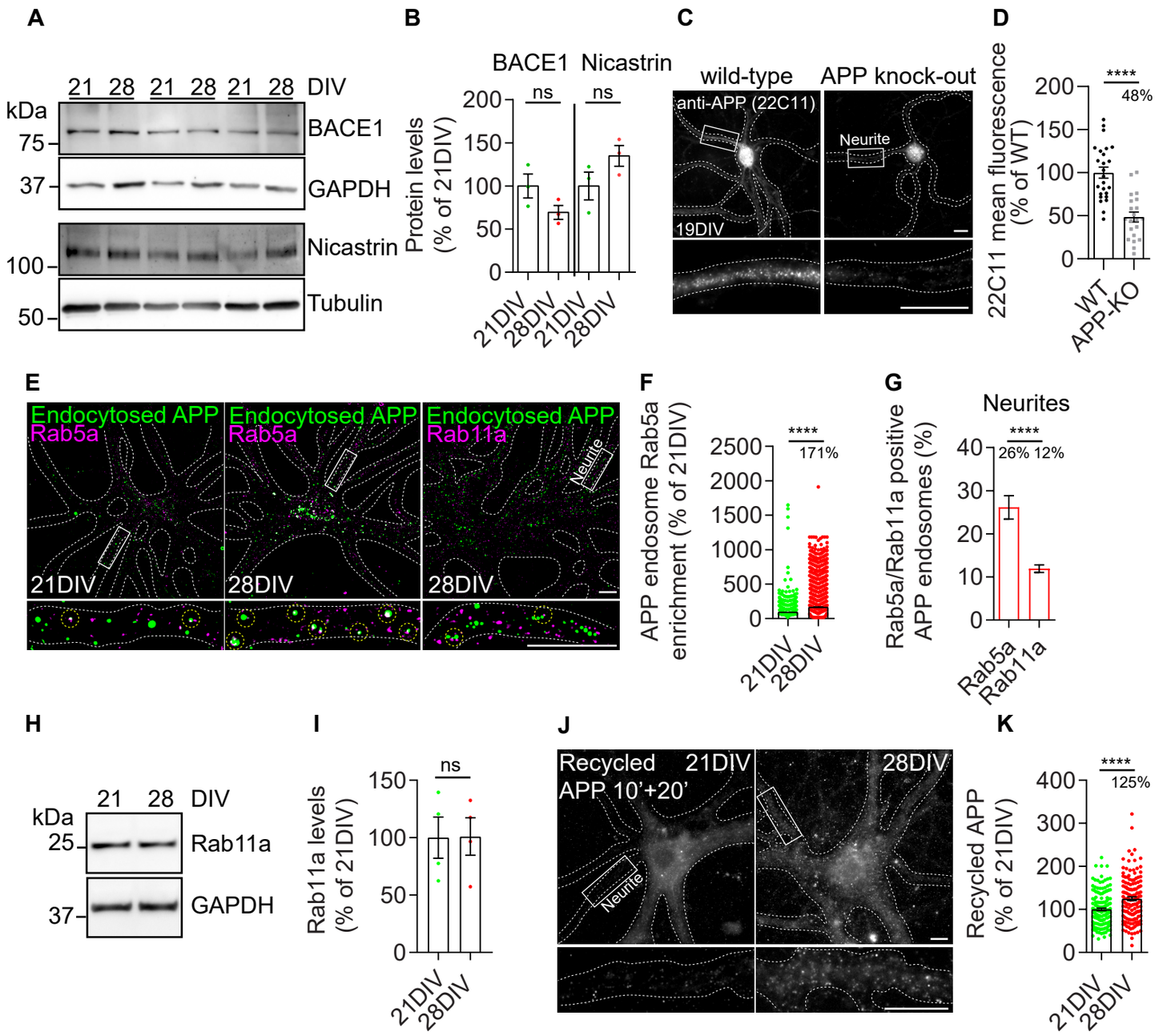

Figure S3. BACE1 and nicastrin levels, APP colocalization with Rab5a/Rab11a and APP recycling.

A. Endogenous BACE1 analyzed by western blot with anti-BACE1 antibody and GAPDH as loading control of neurons at 21 DIV and 28 DIV (top panels). Endogenous subunit of the gamma-secretase complex, nicastrin, analyzed by western blot with anti-nicastrin antibody and tubulin as loading control of neurons at 21 DIV and 28 DIV (bottom panels). **B.** Quantification of BACE1 and nicastrin levels normalized to percentage of 21 DIV neurons (n = 3; $^{ns}P_{\text{BACE1 and nicastrin}}$ = 0.2000 28 DIV vs. 21 DIV, Mann-Whitney test, mean ± SEM). **C.** APP staining with anti-APP antibody (22C11) in 19 DIV wild-type and APP knock-out neurons as a control for specific intracellular APP detection. The white rectangles indicate the magnified regions shown below. Scale bar, 10 µm. **D.** Quantification of 22C11 mean fluorescence intensity in 19DIV neurites of wild-type and APP knock-out (APP-KO) neurons, relative to wild-type (n = 3, N_{neurites}= 21-25, ****P_{neurites} < 0.0001 APP-KO vs. wild-type, unpaired t-test, mean ± SEM). **E.** APP^+ endosomes (10'; green) and Rab5a (magenta) in neurons assessed by immunofluorescence at 21DIV and 28 DIV, with anti-Rab5a antibody. APP^+ endosomes (10'; green) and Rab11a (magenta) in neurons assessed by immunofluorescence at 28DIV, with anti-Rab11a antibody. Both were analyzed by epifluorescence microscopy and displayed upon background subtraction. The white rectangle indicates the magnified neurite shown below. Rab5a and rab11a localization to APP^+ endosomes (dashed yellow rings) on the magnified neurite were generated automatically by the ICY "Colocalizer" protocol. Scale bar, 10 µm. **F.** Quantification of the endosomal Rab5a, i.e. mean intensity of Rab5a per APP^+ endosome, in percentage of 21 DIV, in neurites of 21 DIV and 28 DIV neurons (n=3, $N_{\text{APP+ endosomes}}$ = 11447-15437, ****P< 0.0001 28 DIV vs. 21 DIV neurons, Mann-Whitney test, mean ± SEM). **G.** Quantification of the number (mean) of Rab5a/Rab11a puncta localized to APP^+ endosomes in percentage of APP^+ endosomes per 28DIV neurite (n=3, $N_{\text{Rab5a neurites}}$= 48; $N_{\text{Rab11a neurites}}$= 99, ****$P$< 0.0001 Rab11a vs. Rab5a 28DIV neurons, Mann-Whitney test, mean ± SEM). **H.** Endogenous Rab11a analyzed by western blot with anti-Rab11a antibody and GAPDH as loading control of neurons at 21 DIV and 28 DIV. **I.** Quantification of Rab11a levels normalized to percentage of 21 DIV neurons (n = 4; ^{ns}P = 0.9476 28 DIV vs. 21 DIV, paired t-test, mean ± SEM). **J.** Recycled APP (10' pulse $^+$ 20'chase) in neurites of 21 DIV and 28 DIV neurons, analyzed by epifluorescence microscopy. The white rectangle indicates the magnified neurite shown below. Scale bar, 10 µm. **K.** Quantification of the mean intensity of recycled APP in neurites of 21 DIV and 28 DIV neurons. Results were normalized to percentage of 21 DIV (n = 3, N_{neurites}=143-169; ****P_{neurites} < 0.0001 28 DIV vs. 21 DIV, Mann-Whitney test, mean ± SEM).

Figure S4

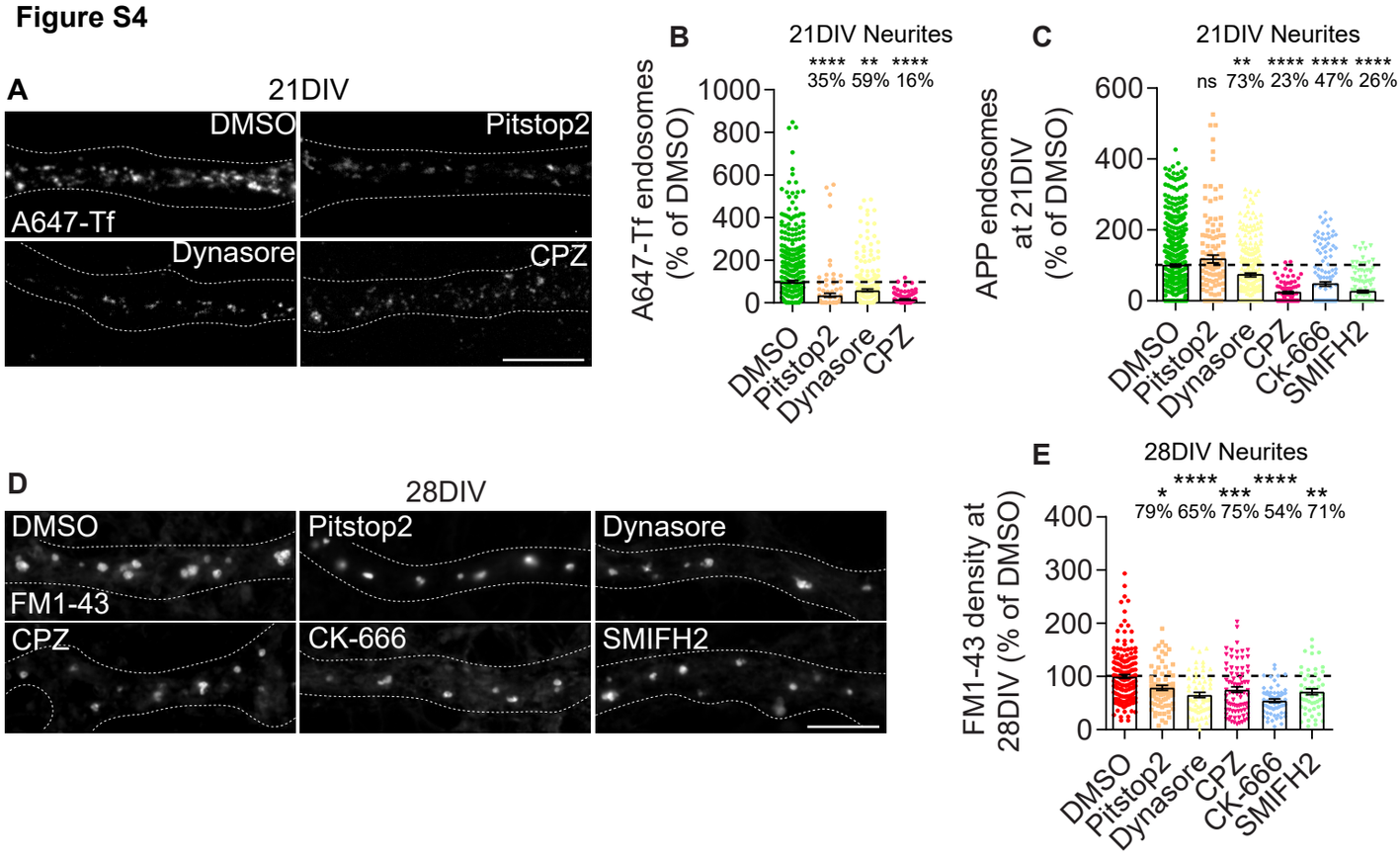

Figure S4. Transferrin, APP, and bulk endocytosis are clathrin- and dynamin-sensitive. APP endocytosis in mature neurons and bulk endocytosis in aged neurons are also dependent on actin.

A. Transferrin endocytosis in neurons pulsed with Alexa647-Tf for 10' at 21 DIV after treatment with DMSO (0.1 %), Pitstop2 (30 µM), Dynasore (100 µM) or CPZ (0.14 µM). Neurons were analyzed by epifluorescence microscopy. Scale bars, 10 µm. **B.** Quantification of the number of transferrin endosomes per area (400 µm2) in 21 DIV neurites upon drug treatments, in percentage of DMSO (n=6, N_{DMSO}= 542, $N_{Pistop2}$= 121, $N_{Dynasore}$= 258, N_{CPZ}= 103, , ****P < 0.0001 Pitstop2-, CPZ-treated vs. DMSO, **P = 0.0055 Dynasore-treated vs. DMSO, one-way ANOVA on ranks with *post hoc* Dunn's testing, mean ± SEM). **C.** Quantification of the number of APP^+ endosomes (10') per area (400 µm2) in 21 DIV neurites upon treatment with Pitstop2 (30µM), Dynasore (100µM), CPZ (0.14 µM), Ck-666 (50 µM), SMIFH2 (30 µM) and DMSO (0.1%), in percentage of control (DMSO) (n=9, N_{DMSO}= 634, $N_{Pistop2}$= 118, $N_{Dynasore}$= 254, N_{CPZ}= 81, N_{Ck-666}= 149, N_{SMIFH2}= 136 , ^{ns}P > 0.9999 Pitstop2 vs. DMSO, ****P < 0.0001 CPZ, Ck-666-, SMIFH2 vs. DMSO, **$P_{Dynasore}$ = 0.0015 Dynasore vs. DMSO, one-way ANOVA on ranks with *post hoc* Dunn's testing, mean ± SEM). **D.** Bulk endocytosis in neurons pulsed with FM1-43 for 10' at 28 DIV neurites after treatment with Pitstop2 (30µM), Dynasore (100µM), CPZ (0.14 µM), Ck-666 (50 µM), SMIFH2 (30 µM) and DMSO (0.1%). Neurons were analyzed by epifluorescence microscopy. Scale bars, 10 µm. **E.** Quantification of the number of FM1-43 puncta per area (400 µm2) in 28DIV neurites upon treatment with Pitstop2 (30µM), Dynasore (100µM), CPZ (0.14 µM), Ck-666 (50 µM), SMIFH2 (30 µM) and DMSO (0.1%), in percentage of control (DMSO) (n=2, N_{DMSO}= 177, $N_{Pistop2}$= 73, $N_{Dynasore}$= 62, N_{CPZ}= 80, N_{Ck-666}= 62, N_{SMIFH2}= 51, *P = 0.0329 Pitstop2 vs. DMSO, **P= 0.0019 SMIFH2 vs. DMSO, ***P= 0.0005 CPZ vs. DMSO, ****P < 0.0001 Dynasore and CK-666 vs. DMSOs, one-way ANOVA on ranks with *post hoc* Dunn's testing, mean ± SEM)

Figure S5

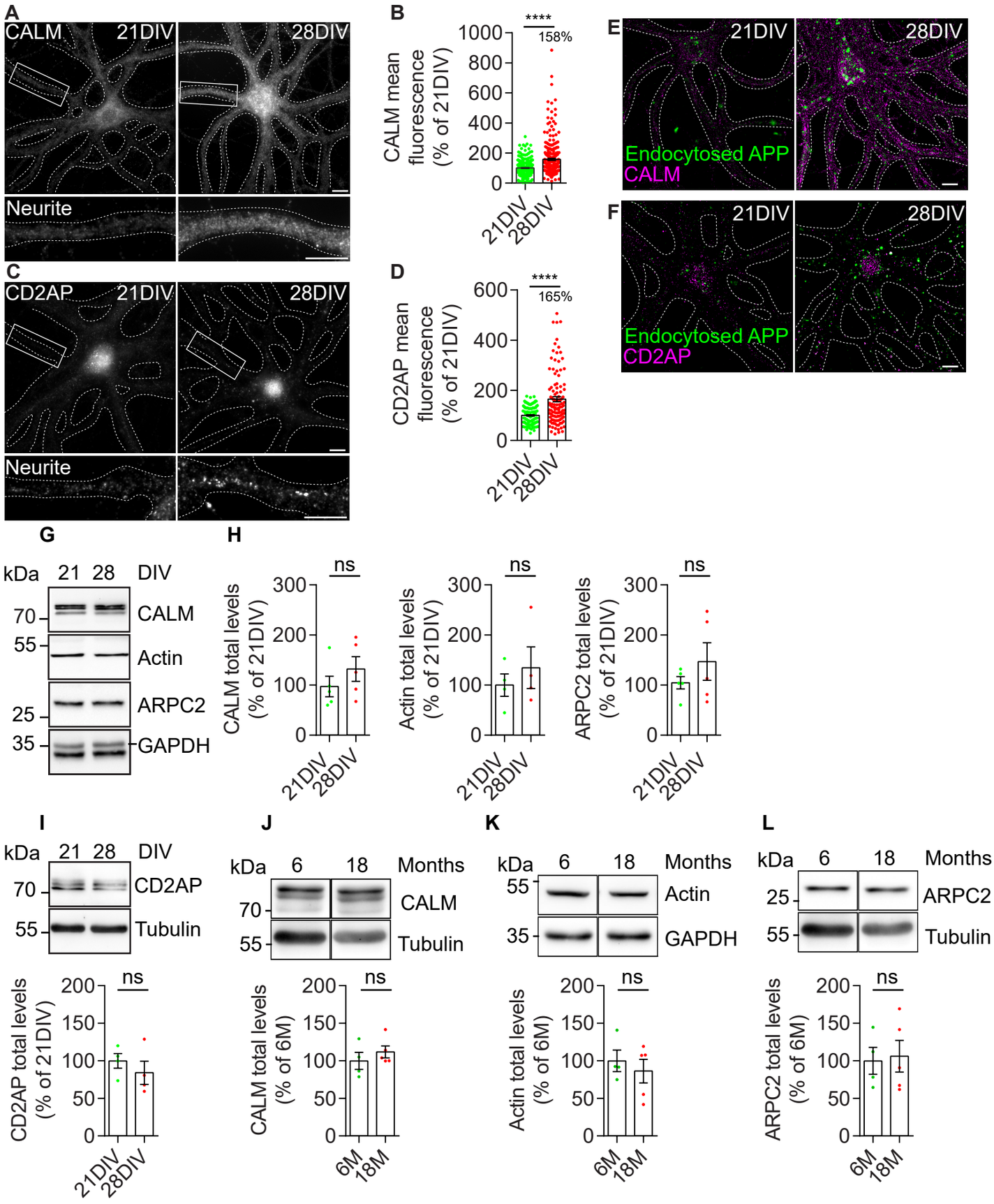

Figure S5. CALM and CD2AP increase with neuronal aging.

A. CALM distribution detected by immunofluorescence of neurons at 21 DIV and 28 DIV, analyzed by epifluorescence microscopy. The white rectangles indicate the magnified 21 DIV and 28 DIV neurites shown below. Scale bars, 10 µm. **B.** Quantification of CALM mean intensity, normalized to percentage of 21 DIV, in 21 DIV and 28 DIV neurites (n=5, $N_{neurites}$= 279-302, ****P < 0.0001 28 DIV vs. 21 DIV, unpaired t-test, mean ± SEM). **C.** CD2AP distribution detected by immunofluorescence of neurons at 21 DIV and 28 DIV, analyzed by epifluorescence microscopy. The white rectangles indicate the magnified 21 DIV and 28 DIV neurites shown below. Scale bars, 10 µm. **D.** Quantification of CD2AP mean intensity, normalized to percentage of 21 DIV, in 21 DIV and 28 DIV neurites (n=3, $N_{neurites}$= 111-122, ****P < 0.0001 28 DIV vs. 21 DIV, unpaired t-test, mean ± SEM). **E.** Enrichment of CALM on APP^+ endosomes (22C11) in the cell body and neurites of 21 DIV and 28 DIV neurons was detected by immunofluorescence, with anti-endocytosed APP antibody (22C11; green) and anti-PICALM antibody (CALM; magenta), analyzed by epifluorescence microscopy and the images are displayed after background subtraction . Scale bar, 10 µm. **F.** Enrichment of CD2AP on APP^+ endosomes (22C11) in the cell body and neurites of 21 DIV and 28 DIV neurons was detected by immunofluorescence, with anti-endocytosed APP antibody (22C11; green) and anti-CD2AP antibody (magenta), analyzed by epifluorescence microscopy and the images are displayed after background subtraction. Scale bar, 10 µm. **G.** Endogenous CALM, Actin, and ARPC2 were analyzed by western blot with anti-PICALM, anti-Actin and anti-ArpC2 antibody, and GAPDH as loading control of neurons at 21 DIV and 28 DIV.

H. Quantification of CALM, Actin and ARPC2 levels normalized to percentage of 21 DIV neurons (n = 4-5; $^{ns}P_{CALM}$ = 0.2222; $^{ns}P_{Actin}$ = 0.6571; $^{ns}P_{ArpC2}$ = 0.6667, 28 DIV vs. 21 DIV, Mann-Whitney test, mean ± SEM). **I.** Endogenous CD2AP analyzed by western blot with the anti-CD2AP antibody and tubulin as loading control of neurons at 21 DIV and 28 DIV. Quantification of CD2AP levels normalized to percentage of 21 DIV neurons (n = 4; ^{ns}P = 0.4857, 28 DIV vs. 21 DIV, Mann-Whitney test, mean ± SEM). **J.** Endogenous CALM analyzed by western blot with anti-PICALM antibody, and tubulin as loading control of adult brains (6 M) and aged brains (18 M). Quantification of CALM levels normalized to the percentage of 6 M brain (n = 4-5; ^{ns}P = 0.5238, 18 M vs. 6 M, Mann-Whitney test, mean ± SEM). **K.** Endogenous Actin analyzed by western blot with anti-actin antibody, and GAPDH as loading control of adult brains (6 M) and aged brains (18 M). Quantification of actin levels normalized to the percentage of 6 M brain (n = 4-5; ^{ns}P = 0.8730, 18 M vs. 6 M, Mann-Whitney test, mean ± SEM). **L.** Endogenous ARPC2 analyzed by western blot with anti-ARPC2 antibody, and tubulin as loading control of adult brains (6 M) and aged brains (18 M). Quantification of ARPC2 levels normalized to the percentage of 6 M brain (n = 4-5; ^{ns}P > 0.9999, 18 M vs. 6 M, Mann-Whitney test, mean ± SEM).

Figure S6

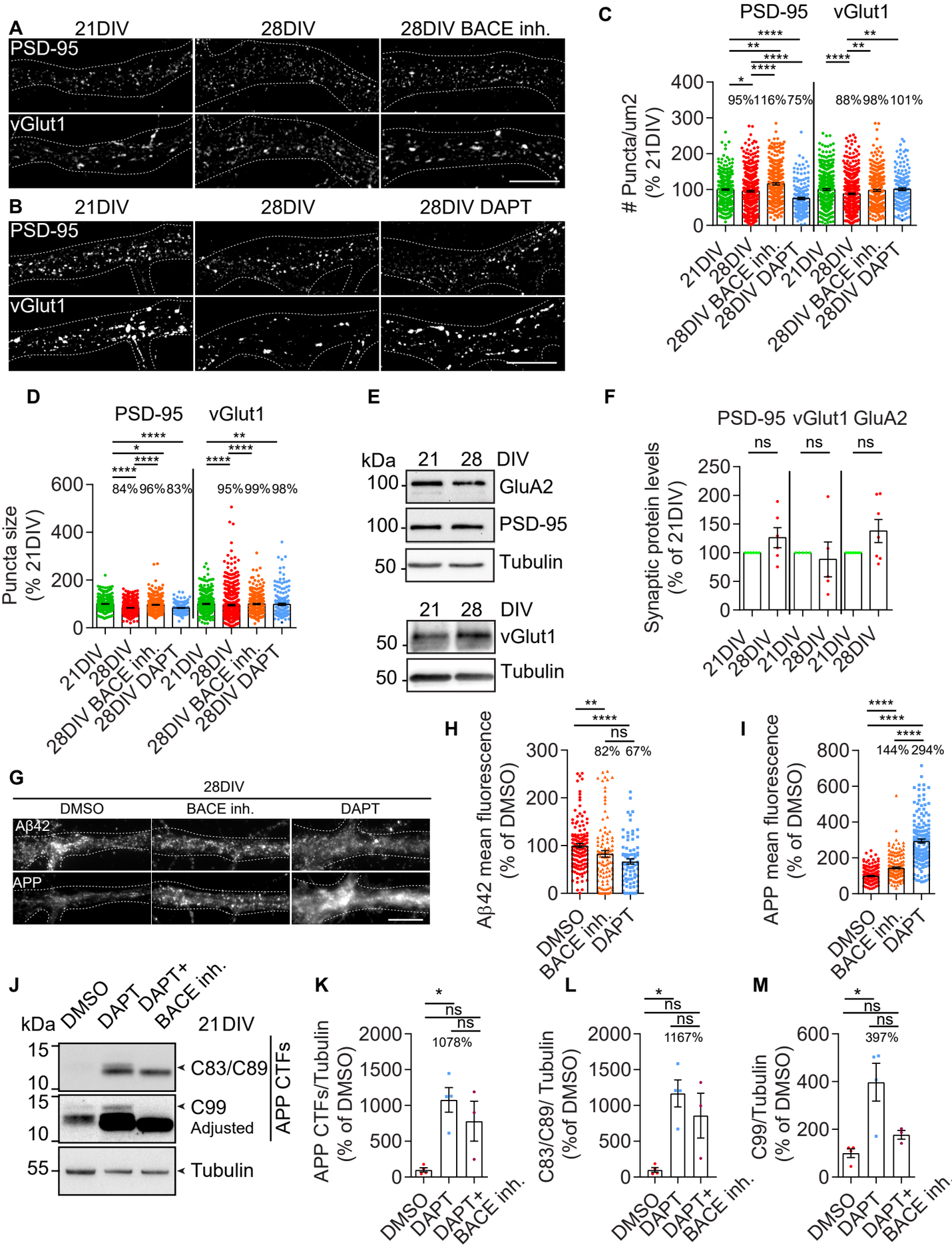

Figure S6. Aged synaptic proteins' puncta density and size are dependent on Aβ production. DAPT and BACE inhibitor are effective reducing Aβ levels and increasing APP processing.

A. PSD-95 and vGlut puncta in neurites of 21 DIV neurons, 28 DIV neurons, and 28 DIV neurons treated with BACE inhibitor IV, analyzed by epifluorescence microscopy, and displayed after background subtraction. Scale bar, 10 µm. **B.** PSD-95 and vGlut puncta in neurites of 21 DIV neurons, 28 DIV neurons, and 28 DIV neurons treated with DAPT, analyzed by epifluorescence microscopy, and displayed after background subtraction. Scale bar, 10 µm. **C.** Quantification of the number of PSD-95 and vGlut1 per 50 µm2 of neurites in 21 DIV neurites, 28 DIV neurites and DAPT or BACE inhibitor-treated 28DIV neurites. Results were normalized to percentage of 21 DIV (n=7; $N_{21DIV\ PSD\text{-}95}$=419 neurites; $N_{28DIV\ PSD\text{-}95}$=517 neurites; $N_{28DIV\ BACE\ inh.\ PSD\text{-}95}$=306 neurites; $N_{28DIV\ DAPT\ PSD\text{-}95}$=170 neurites; $N_{21DIV\ vGlut}$=418 neurites; $N_{28DIV\ vGlut}$=512 neurites; $N_{28DIV\ BACE\ inh.\ vGlut}$=304 neurites; $N_{28DIV\ DAPT\ vGlut}$=170 neurites; **P*=0.0279 PSD-95 puncta density in 28 DIV vs. 21 DIV neurites, *****P* < 0.0001 PSD-95 puncta density in BACE inh.-treated vs. not treated 28 DIV neurites; ***P*=0.0015 PSD-95 puncta density in 28 DIV BACE inh.-treated vs. not treated 21 DIV neurites; *****P* < 0.0001 PSD-95 puncta density in DAPT-treated vs. not treated 28 DIV neurites; *****P* < 0.0001 PSD-95 puncta density in 28 DIV DAPT-treated vs. not treated 21 DIV neurites; *****P* < 0.0001 vGlut1 puncta density in 28 DIV vs. 21 DIV neurites, ***P*=0.0033 vGlut1 puncta density in BACE inh.-treated vs. not treated 28 DIV neurites; ^{ns}P=0.3202 vGlut1 puncta density in 28 DIV BACE inhibitor-treated vs. not treated 21 DIV neurites; ^{ns}P = 0.9934 vGlut1 puncta density in 28 DIV DAPT-treated vs. not treated 21 DIV neurites, ***P* = 0.0024 vGlut1 puncta density in DAPT-treated vs. not treated 28 DIV neurites Mann Whitney test, mean ± SEM). **D.** Quantification of the size of PSD-95 and vGlut1 puncta in 21DIV neurites, 28 DIV neurites and DAPT or BACE inh.-treated 28DIV neurites. Results were normalized to percentage of 21 DIV (n=7; $N_{21DIV\ PSD\text{-}95}$=419 neurites; $N_{28DIV\ PSD\text{-}95}$=517 neurites; $N_{28DIV\ BACE\ inh.\ PSD\text{-}95}$=306 neurites; $N_{28DIV\ DAPT\ PSD\text{-}95}$=170 neurites; $N_{21DIV\ vGlut}$=418 neurites; $N_{28DIV\ vGlut}$=512 neurites; $N_{28DIV\ BACE\ inh.\ vGlut}$=304 neurites; $N_{28DIV\ DAPT\ vGlut}$=170 neurites; *****P* < 0.0001 PSD-95 size in 28 DIV vs. 21 DIV neurites, ^{ns}P = 0.0739 PSD-95 size in DAPT-treated vs. not treated 28 DIV neurites; **P*=0.0102 PSD-95 size in 28 DIV BACE inh.-treated vs. not treated 21 DIV neurites; *****P* < 0.0001 PSD-95 size in BACE inh.-treated vs. not treated 28 DIV neurites; *****P* < 0.0001 PSD-95 size in 28 DIV DAPT-treated vs. not treated 21 DIV neurites; *****P* < 0.0001 vGlut1 size in 28 DIV vs. 21 DIV neurites, *****P* < 0.0001 vGlut1 size in BACE inh.-treated vs. not treated 28 DIV neurites; ^{ns}P = 0.3114 vGlut1 size in 28 DIV BACE inh.-treated vs. not treated 21 DIV neurites; ^{ns}P = 0.3544 vGlut1 size in DAPT-treated vs. not treated 28 DIV neurites, ***P* = 0.0014 vGlut1 size in 28DIV DAPT-treated vs. not treated 21 DIV neurites, Mann Whitney test, mean ± SEM). **E.** GluA2, PSD-95, and vGlut1 total levels in neurons at 21 DIV and 28 DIV, analyzed by western blot with anti-PSD-95, anti-GluA2 and anti-vGlut1 antibody. Tubulin was immunoblotted as the loading control. **F.**

Quantification of PSD-95, vGlut1 and GluA2 levels normalized to tubulin and to the percentage of 21 DIV ($n_{PSD\text{-}95}$ = 6; n_{vGlut1} = 5; n_{GluA2} = 7; $^{ns}P_{PSD\text{-}95}$ = 0.2188, $^{ns}P_{vGlut1}$ = 0.8125, $^{ns}P_{GluA2}$ = 0.2188, Wilcoxon test, mean ± SEM). **G.** Endogenous Aβ42 and APP mean intensity in neurites of 28 DIV neurons treated with DMSO (0.1%), DAPT or BACE inhibitor IV, immunolabelled with anti-Aβ42 (12F4) and anti-APP (Y188) antibody, analyzed by epifluorescence microscopy. Scale bar, 10 µm. **H.** Quantification of Aβ42 mean fluorescence intensity in 28DIV neurites, in percentage of control (DMSO) (n = 3-4, N_{DMSO}= 134, N_{DAPT}= 78, $N_{BACE\ inh.}$= 99, ****P < 0.0001 DAPT-treated vs. DMSO, **P = 0.0025 BACE inh.-treated vs. DMSO, ^{ns}P =0.4943 DAPT-treated vs. BACE inh.-treated, one-way ANOVA on ranks with *post hoc* Dunn's testing, mean ± SEM). **I.** Quantification of APP mean intensity in 28DIV neurites, in percentage of control (DMSO) (n = 4-5, N_{DMSO}= 217, N_{DAPT}= 151, $N_{BACE\ inh.}$= 171, ****P < 0.0001 DAPT-treated vs. DMSO, ****P < 0.0001 BACE inh.-treated vs. DMSO, ****P < 0.0001 DAPT-treated vs. BACE inh.-treated, one-way ANOVA on ranks with *post hoc* Dunn's testing, mean ± SEM). **J.** Endogenous APP-CTFs (C191, C83/89, C99) total levels in neurons at 21 DIV treated with DMSO, DAPT, and DAPT plus BACE inhibitor IV, analyzed by western blot. Tubulin was immunoblotted as the loading control. **K.** Quantification of APP-CTFs total levels in 21DIV neurons, normalized to tubulin (n = 3-4; *$P_{APP\ CTFs}$ = 0.0315 DAPT-treated vs. DMSO, $^{ns}P_{APP\ CTFs}$ = 0.1692 DAPT plus BACE inh.-treated vs. DMSO, $^{ns}P_{APP\ CTFs}$ > 0.9999 DAPT plus BACE inh.-treated vs. DAPT-treated, one-way ANOVA on ranks with *post hoc* Dunn's testing, mean ± SEM). **L.** Quantification of C83/C89 total levels in 21DIV neurons, normalized to tubulin (n = 3-4; *$P_{C83/C89}$ = 0.0315 DAPT-treated vs. DMSO, $^{ns}P_{C83/C89}$ = 0.1692 DAPT plus BACE inh.-treated vs. DMSO, $^{ns}P_{C83/C89}$ > 0.9999 DAPT plus BACE inh.-treated vs. DAPT-treated, one-way ANOVA on ranks with *post hoc* Dunn's testing, mean ± SEM). **M.** Quantification of C99 total levels in 21DIV neurons, normalized to tubulin (n = 3-4; *P_{C99} = 0.0167 DAPT-treated vs. DMSO, $^{ns}P_{C99}$ = 0.3000 DAPT plus BACE inh.-treated vs. DMSO, $^{ns}P_{C99}$ > 0.9999 DAPT plus BACE inh.-treated vs. DAPT-treated, one-way ANOVA on ranks with *post hoc* Dunn's testing, mean ± SEM).

Figure S7

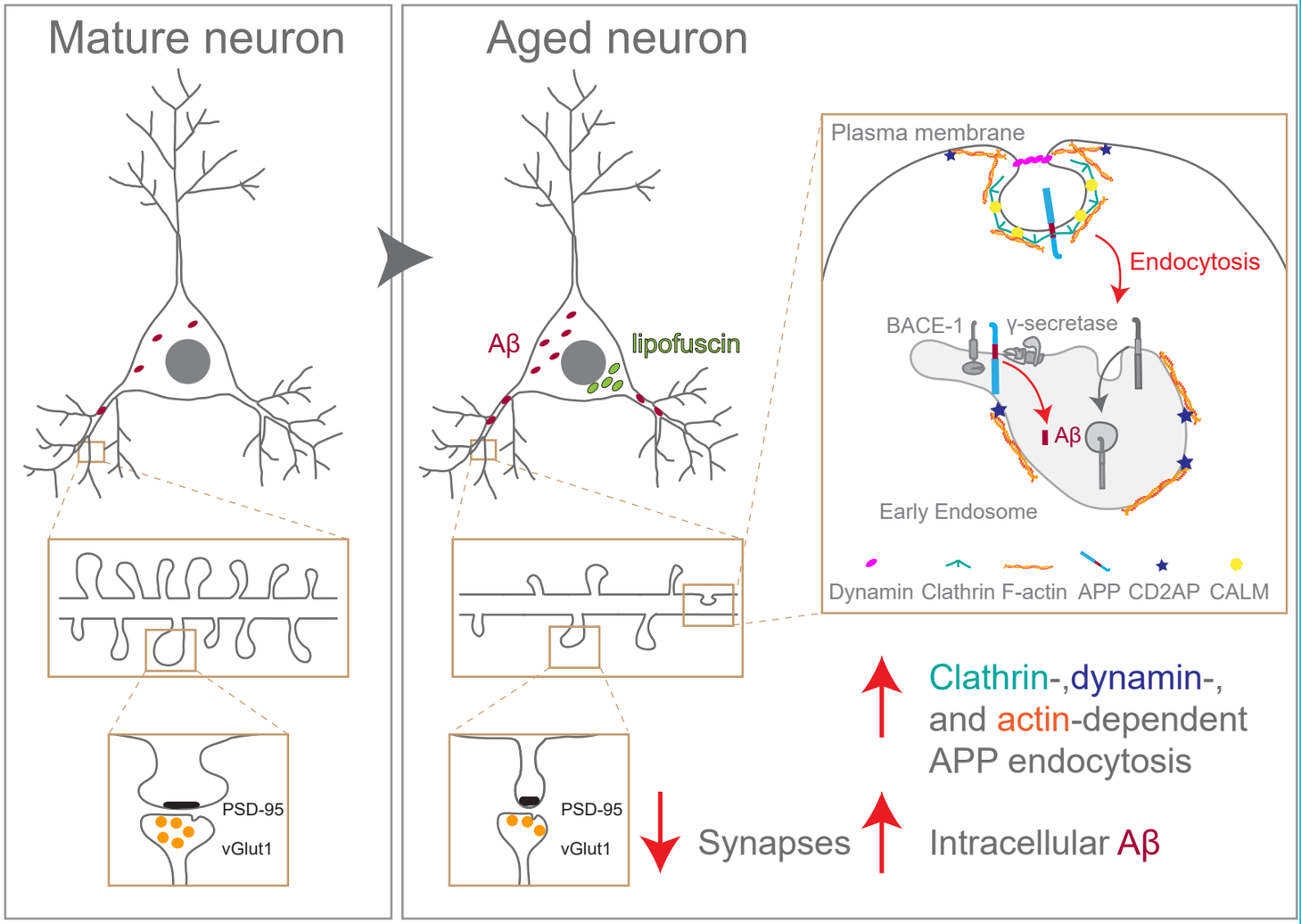

Figure S7. Schematics of APP endocytosis up-regulation and synapse loss with aging

Neuronal aging up-regulates APP endocytosis by increasing clathrin assembly and F-actin polymerization, recruiting more APP endocytic adaptors (CD2AP and CALM) to endocytic sites in aged neurons. The increase in APP endocytosis, will enhance the encounter with its secretases, and potentiate Aβ production during neuronal aging eventually triggering synapse decline and favoring the development of late-onset Alzheimer's disease.

Table S1

(1) P values in Figure 1B

	21DIV	28DIV
14DIV	0.0432	0.0095

(2) P values in Figure 1E

	28DIV
21DIV	< 0.0001

(3) P values in Figure 1G

	28DIV
21DIV cell body	< 0.0001
21DIV neurites	0.9027

(4) P values in Figure 1I

	14DIV	21DIV	28DIV
cell body			
14DIV	-	0.2790	0.0158
21DIV	0.2790	-	0.3231
Neurites			
14DIV	-	> 0.9999	< 0.0001
21DIV	> 0.9999	-	< 0.0001

(5) P values in Figure 1K

	28DIV
21DIV cell body	0.6739
21DIV neurites	< 0.0001

(6) P values in Figure 2B

	21DIV	28DIV
14DIV	> 0.9999	0.0071
21DIV	-	0.0039

(7) P values in Figure 2C

	21DIV	28DIV
14DIV	> 0.9999	0.0811
21DIV	-	0.0094

(8) P values in Figure 2D

	21DIV	28DIV
14DIV	> 0.9999	0.0038
21DIV	-	0.0033

(9) P values in Figure 2E

	21DIV	28DIV
14DIV	0.0067	0.0050
21DIV	-	> 0.9999

Journal of Cell Science • Supplementary information

(10)P values in Figure 2F

	21DIV	28DIV
14DIV	> 0.9999	0.0323
21DIV	-	0.0006

(11)P values in Figure 2G

	21DIV	28DIV
14DIV	> 0.9999	0.4146
21DIV	-	0.7539

(12)P values in Figure 2I

	18M
6M	0.0110

(13)P values in Figure 2J

	18M
6M	0.7562

(14)P values in Figure 2K

	18M
6M	0.1071

(15)P values in Figure 2L

	18M
6M	0.2269

(16)P values in Figure 2M

	18M
6M	0.0397

(17)P values in Figure 2N

	18M
6M	0.0024

(18)P values in Figure 3B

	28DIV
21DIV	0.3374

(19)P values in Figure 3C

	28DIV
21DIV	< 0.0001

(20)P values in Figure 3D

	28DIV
21DIV	< 0.0001

(21)P values in Figure 3F

	28DIV
21DIV	0.0857

(22)P values in Figure 3G

	28DIV
21DIV	< 0.0001

(23)P values in Figure 3H

	28DIV
21DIV	0.0138

(24)P values in Figure 3J

	28DIV
21DIV	0.0275

(25)P values in Figure 3L

	28DIV
21DIV	0.2275

(26)P values in Figure 3N

	18M
12M	0.0016

(27)P values in Figure 3O

	18M
12M	0.0002

(28)P values in Figure 3P

	18M
12M	0.0038

(29)P values in Figure 3R

	18M
12M	0.5225

(30)P values in Figure 3S

	18M
12M	0.0215

(31)P values in Figure 3T

	18M
12M	0.0008

(32)P values in Figure 4C

	28DIV
21DIV 10’	0.0476
21DIV 30’	0.0079

(33)P values in Figure 4D

	28DIV
21DIV	0.0210

(34)P values in Figure 4E

	28DIV
21DIV	0.4316

(35)P values in Figure 4H

	28DIV
21DIV	< 0.0001

(36)P values in Figure 4I

	28DIV
21DIV	< 0.0001

(37)P values in Figure 4J

	28DIV
21DIV	0.2159

(38)P values in Figure 4M

	28DIV
21DIV 10’	> 0.9999
21DIV 60’	> 0.9999
21DIV 120’	0.6000

(39)P values in Figure 4O

	28DIV
21DIV	0.0004

(40)P values in Figure 5B

	28DIV
21DIV	0.5795

(41)P values in Figure 5C

	28DIV
21DIV	0.0034

(42)P values in Figure 5D

	28DIV
21DIV	0.0353

(43)P values in Figure 5F

	28DIV
21DIV	< 0.0001

(44)P values in Figure 5H

	28DIV
21DIV	< 0.0001

(45)P values in Figure 5J

	18M
6M	0.1111

(46)P values in Figure 5L

	28DIV
21DIV	< 0.0001

(47)P values in Figure 5M

	28DIV
21DIV	< 0.0001

(48)P values in Figure 5N

	28DIV
21DIV	0.0003

(49)P values in Figure 6B

	28DIV DMSO
28DIV Pitstop2	< 0.0001
28DIV Dynasore	< 0.0001
28DIV CPZ	< 0.0001
28DIV CK-666	< 0.0001
28DIV SMIFH2	< 0.0001

(50)P values in Figure 6D

	28DIV
21DIV	0.0317

(51)P values in Figure 6F

	18M
6M	0.0317

(52)P values in Figure 6H

	28DIV
21DIV	< 0.0001

(53)P values in Figure 6I

	28DIV
21DIV	0.5745

(54)P values in Figure 6J

	28DIV
21DIV	> 0.9999

Journal of Cell Science • Supplementary information

(55)P values in Figure 6L

	28DIV
21DIV	< 0.0001

(56)P values in Figure 6N

	28DIV
21DIV	< 0.0001

(57)P values in Figure 6P

	28DIV
21DIV	< 0.0001

(58)P values in Figure 6Q

	28DIV
21DIV	0.0344

(59)P values in Figure 7B

	28DIV
21DIV	< 0.0001
28DIV DAPT	0.0006

(60)P values in Figure 7D

	28DIV
21DIV	< 0.0001
28DIV BACE inhibitor IV	< 0.0001

(61)P values in Figure 7F

	28DIV	28DIV DAPT
21DIV	< 0.0001	< 0.0001
28DIV DAPT	< 0.0001	-

(62)P values in Figure 7G

	28DIV	28DIV DAPT
21DIV	< 0.0001	0.0002
28DIV DAPT	0.0483	-

(63)P values in Figure 7I

	21DIV Rab5-mCherry
21DIV mCherry	0.0171

(64)P values in Figure 7K

	21DIV Rab5-mCherry
21DIV mCherry	0.0428

(65)P values in Figure 7L

	21DIV Rab5-mCherry
21DIV mCherry	0.0002

(66)P values in Figure 7M

	21DIV Rab5-mCherry
21DIV mCherry	0.0385